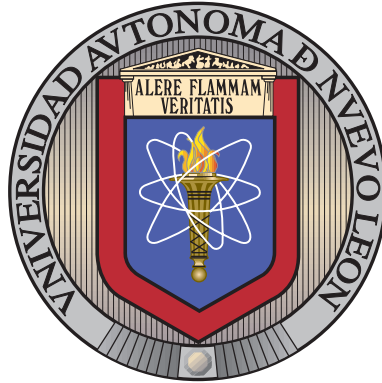


UNIVERSIDAD AUTÓNOMA DE NUEVO LEÓN

FACULTAD DE INGENIERÍA MECÁNICA Y ELÉCTRICA



DEVELOPMENT OF A VOID FRACTION SENSING  
METHOD FOR TWO-PHASE FLOW  
CHARACTERIZATION AND ITS APPLICATION IN  
REFRIGERATION SYSTEMS

POR

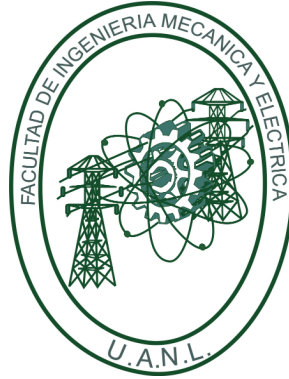
OZIEL SILVA ALVARADO

COMO REQUISITO PARCIAL PARA OBTENER EL GRADO DE  
MAESTRÍA EN CIENCIAS DE LA INGENIERÍA  
CON ORIENTACIÓN EN ENERGÍAS TÉRMICA Y RENOVABLE

4 DE OCTUBRE DE 2023

UNIVERSIDAD AUTÓNOMA DE NUEVO LEÓN

FACULTAD DE INGENIERÍA MECÁNICA Y ELÉCTRICA



DEVELOPMENT OF A VOID FRACTION SENSING  
METHOD FOR TWO-PHASE FLOW  
CHARACTERIZATION AND ITS APPLICATION IN  
REFRIGERATION SYSTEMS

POR

OZIEL SILVA ALVARADO

COMO REQUISITO PARCIAL PARA OBTENER EL GRADO DE  
MAESTRÍA EN CIENCIAS DE LA INGENIERÍA  
CON ORIENTACIÓN EN ENERGÍAS TÉRMICA Y RENOVABLE

4 DE OCTUBRE DE 2023

**UNIVERSIDAD AUTÓNOMA DE NUEVO LEÓN**  
**Facultad de Ingeniería Mecánica y Eléctrica**  
**Posgrado**

Los miembros del Comité de Evaluación de Tesis recomendamos que la Tesis “Development of a void fraction sensing method for two-phase flow characterization and its application in refrigeration systems”, realizada por el estudiante Oziel Silva Alvarado, con número de matrícula 1736707, sea aceptada para su defensa como requisito parcial para obtener el grado de Maestría en Ciencias de la Ingeniería con Orientación en Energías Térmica y Renovable.

**El Comité de Evaluación de Tesis**

Dr. Santos Méndez Díaz  
Director

Dr. Arturo Morales Fuentes  
Co-Director

Dr. Daniel de la Rosa Urbalejo  
Revisor

Dr. Efrain Alcorta García  
Revisor

Dr. Miguel Ángel Platas Garza  
Revisor

Vo.Bo.

  
Dr. Simón Martínez Martínez  
Subdirector de Estudios de Posgrado

Institución 190001

Programa 507507

Acta Núm. 4237

Ciudad Universitaria, a 19 de septiembre de 2023.

*“We have come to define significance as ‘I’m special. Everything else isn’t’. . . . The top four ingredients in life, in your body; top four atoms in order: hydrogen, oxygen, carbon, nitrogen. Those four atoms. Do you know -which are- the top four chemically active atoms in the universe? Hydrogen, oxygen, carbon, nitrogen. Upon learning that you’re not special because you do not contain special ingredients is the same fact that includes that the idea -of- while we live in this universe, the universe lives within us. We are special, because we are the same.”*

*- Neil deGrasse Tyson -*

# *Dedicatoria*

*Agradezco y dedico este trabajo a mis padres, José Juventino Silva Jurado y Elizabeth Alvarado Martínez, quienes me han apoyado en todo ámbito y me inspiraron a seguir adelante con mis estudios e iniciarme en el mundo de la investigación. A mi hermano, Osvaldo, quien desde niños me enseñó de sus experiencias y conocimientos y siempre me apoyó en hacer más de lo que puedo y su esposa, Ingrid Navarro, a quien siempre he visto como una hermana solidaria y afectiva.*

*A mi tío Heriberto Pérez Silva, quien me apoyó en la elaboración de partes pequeñas pero de suma importancia de las instalaciones de este trabajo y siempre he apreciado sus conocimientos y amabilidad. Mis amigos Bernardo, Hugo, Daniel, Héctor, David, Gilberto, José y Juliana que desde hace 9 años que me han seguido, escuchado y apoyado tanto en lo académico como en la vida. A la maestra Gloria Alejandra Rodríguez Aguayo, que en paz descanse, por ser la primera docente que creyó en mis casi imposibles metas. También quisiera agradecer el apoyo y confianza otorgada por el maestro Juan Rafael Cervantes Vega, quien también me ayudó en mi formación académica y laboral. Adicionalmente, quiero agradecer a mi familia, amistades y mascota, Lolita, que siempre me han apoyado en todo.*

*Para finalizar, quisiera agradecer a mis asesores, los doctores Santos Méndez Díaz y Arturo Morales Fuentes por el gran apoyo, orientación, motivación y enseñanza que me brindaron, además de su confianza plena puesta en mí.*

# TABLE OF CONTENTS

---

<b>Acknowledgements</b>	<b>x</b>
<b>1. Introduction</b>	<b>1</b>
1.1. Low GWP refrigerants and the global warming: the zeotropic mixtures problem . . . . .	1
1.2. Void fraction . . . . .	4
1.3. Void fraction and flow models . . . . .	5
1.3.1. Homogeneous and K $\alpha$ H models . . . . .	6
1.3.2. Slip Model . . . . .	6
1.3.3. Drift flux model . . . . .	7
1.4. Flow regime . . . . .	7
1.5. Hypothesis . . . . .	8
1.6. Objectives and outline . . . . .	8
1.6.1. Specific objectives . . . . .	9
1.7. Thesis chapters description . . . . .	10
1.8. Nomenclature . . . . .	11

---

1.9. References . . . . .	12
<b>2. Instrumentation and equipment background</b>	<b>13</b>
2.1. Void fraction measurement methods . . . . .	13
2.2. Image analysis method . . . . .	14
2.2.1. High-speed camera . . . . .	15
2.3. Capacitance sensor . . . . .	15
2.3.1. Capacitance electrode-based sensor . . . . .	16
2.4. Electrical probe sensors . . . . .	17
2.4.1. Impedance needle-probe sensor . . . . .	18
2.5. Issues on measurement . . . . .	19
2.6. Nomenclature . . . . .	20
2.7. References . . . . .	21
<b>3. Experimental facilities construction</b>	<b>23</b>
3.1. Visualization test facility . . . . .	23
3.2. Calibration test facility . . . . .	25
3.3. Image capture section construction . . . . .	28
3.4. Capacitance sensor construction . . . . .	29
3.4.1. The construction process . . . . .	29
3.5. Impedance needle-probe sensor construction . . . . .	35
3.5.1. The construction process . . . . .	37

---

3.6. Acquisition of the signals . . . . .	42
3.6.1. Bridge circuit . . . . .	43
3.6.2. RLC circuits . . . . .	44
3.6.3. Comparator circuits . . . . .	45
3.6.4. The designed circuits . . . . .	46
3.7. Nomenclature . . . . .	50
3.8. References . . . . .	51
<b>4. Experimental campaign</b>	<b>54</b>
4.1. Calibration procedure . . . . .	54
4.2. Captured images analysis . . . . .	57
4.2.1. Image analysis void fraction . . . . .	58
4.2.2. Image analysis superficial gas velocity . . . . .	61
4.3. Flow regime identification . . . . .	63
4.3.1. The Probability Density Function (PDF) . . . . .	63
4.4. Flow regime theoretical determination . . . . .	65
4.4.1. 3-D Flow Regime Map . . . . .	65
4.4.2. Air-Water Flow Regime Map Comparison . . . . .	69
4.5. Theoretical void fraction analysis . . . . .	69
4.6. Nomenclature . . . . .	78
4.7. References . . . . .	80



---

<b>5. Results</b>	<b>82</b>
5.1. Impedance needle probe sensor . . . . .	82
5.2. Capacitance electrode-based sensor . . . . .	89
5.3. Image analysis . . . . .	92
5.4. Experimental to theoretical comparison . . . . .	94
5.4.1. Void fraction comparison . . . . .	94
5.4.2. Flow regime comparison . . . . .	103
5.5. Nomenclature . . . . .	105
5.6. References . . . . .	107
<b>6. Conclusions</b>	<b>108</b>
6.1. Further works . . . . .	110

# ACKNOWLEDGEMENTS

---

I am grateful for the support provided by the CONACYT with the no. 1101661 research scholarship and the scientific and technology research support programme PAICYT-UANL 2022 for supporting this work.

I am also grateful for the donation provided by ROGERS CORPORATION for this work, providing the necessary material to build the capacitance sensor.

# INTRODUCTION

---

## 1.1 LOW GWP REFRIGERANTS AND THE GLOBAL WARMING: THE ZEOTROPIC MIXTURES PROBLEM

Refrigerant gases usage represents one of the main pollution sources. The parameters Ozone Depletion Potential (ODP) and Global Warming Potential (GWP) are employed to determine the risk that a particular refrigerant represents to the environment. Pure refrigerant mixtures, whose mix proportions make them have a lower impact on the environment, are an environmental impact mitigation strategy involving the use of refrigerants. One recently used and low GWP refrigerant in refrigeration systems is the R-448A, which has exceptional physicochemical properties, similar to those from R-404A. The R-404A, which has a high GWP, is also beginning to get replaced by the R-448A. However, this refrigerant is a zeotropic mixture.

An azeotropic mixture has a similar behavior to that of a pure substance on its phase change at constant pressure and temperature, while a zeotropic mixture behaves differently. That is, as the case of the azeotropic and pure substances has the fluid change its state of matter evenly, the zeotropic substances do not change evenly, since, for instance, some portion of the substance will boil at a constant pressure and temperature and the other portion will not, since all the energy that

is put into the substance will be divided momentarily between the phase-change of one portion and the reaching of the boiling point of the other portion, so it will make the proportions uneven at some points. Thereby, making the mass proportion between two or more substances in a zeotropic mixture differ on its gaseous phase in comparison to its liquid phase as it is represented in Fig. 1.

The boiling process in a gas compression refrigeration system defines the cooling capacity of the system. The isenthalpic expansion process characterizes the condition of the refrigerant at the evaporator inlet, whilst the superheat conditions at the evaporator outlet determine the outlet enthalpy. Thus, the enthalpy difference and the mass flux establish the cooling capacity. Knowledge of the gas quality of the refrigerant at the evaporator inlet may determine the cooling capacity better, as well as it could give necessary information to optimize the system's operation.

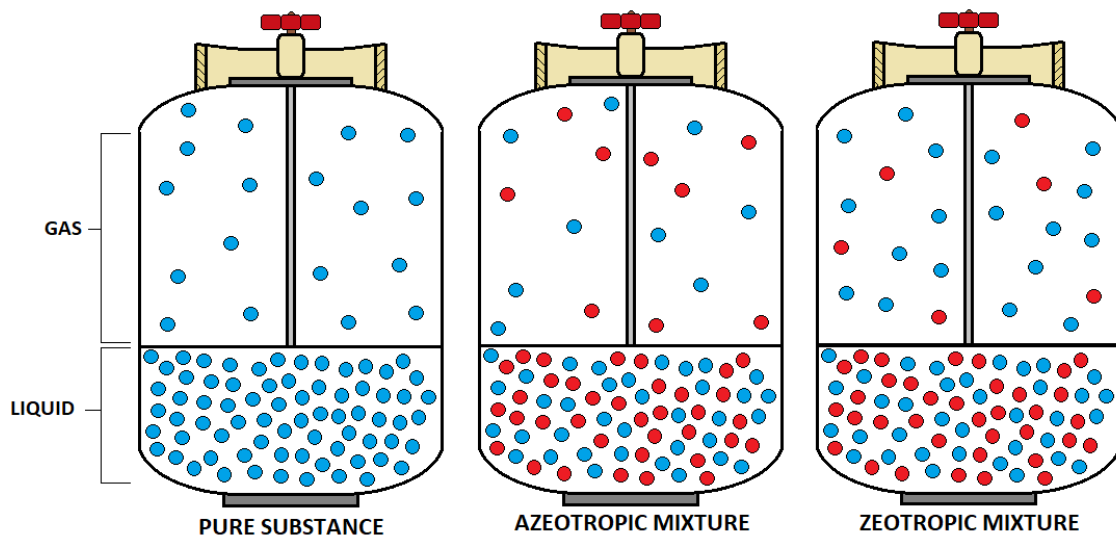


Figure 1 – Visual representation of a pure substance, an azeotropic substance and a zeotropic substance during their phase change. Suppose that both azeotropic and zeotropic mixtures are a 50%-50% two-substance mixtures. The blue and red particles depict separately the substances that would constitute a two-substance mixture, where the count of boiled (top) particles from the liquid particles (bottom) in the azeotropic mixture and the zeotropic mixture is 9 blue and 9 red, and 18 blue and 6 red respectively.

There are several methods to characterize multiphase flows [1] and most of them are based on void fraction measurement. Nonetheless, most of the methods require calibration of the equipment by Quick Closing Valves (QCV) methods or by image analysis methods due to their trustworthy precision.

Due to expansion processes in refrigeration systems being frequently supposed to be isenthalpic for simplicity, it is common to get imprecise results in relation to the gas quality. The need of obtaining the void fraction has its origin on its direct relation with the gas quality acquisition. Therefore, it becomes a vital characteristic for the calculus of important characteristics like the pressures drop and the heat transfer coefficient, which have a huge and direct influence in refrigeration applications.

Void fraction characterizations in refrigeration systems are often done with refrigerant R-410A as the working fluid. Studies that involve zeotropic refrigerants usually employ R-410A. For instance, [Wotjan et al. \[2\]](#) measured the void fraction for refrigerants R-22 and R-410A employing image analysis in a glass tube under a stratified-slug flow regime illuminated by a laser. It had a  $\pm 0.01$  precision in void fraction range from 0.05 to 0.95, but it was mentioned that this technique has difficulties when evaluating small diameter tubes. [Portillo et al. \[3\]](#) described and made a calibration procedure in situ for a capacitive void fraction sensor on a 3 mm tube; R-410A was employed in gas quality conditions in the range of 0 to 1, though the results were only satisfactory for low gas qualities.

To the authors' knowledge, there is a lack of reported studies concerning void fraction measurement on low GWP zeotropic refrigerants. It is also of interest that measurement of the void fraction via image analysis is often done in glass-sight tubes, whose adaptation to the experimental facility is, due to methodology issues, of huge dimensions and have a hard-time when making it so.

## 1.2 VOID FRACTION

The void fraction is a dimensionless parameter defined by the ratio of the covered gas space over the total flow space through a cross-section, Eq. (1.1). Likewise, void fraction measurements can be defined at a point (local), over a line, a surface or a volume [4]. Such definitions can be seen in detail on Fig. 2.

$$\alpha = \frac{\text{Occupied space}_{gas}}{\text{Occupied space}_{total}} \quad (1.1)$$

Void fraction ( $\alpha$ ) and static flow quality ( $x_{st}$ ; also known as mass quality) are strictly related by the gas and liquid density of the flow, since void fraction is based on space (which is related to volume) and mass quality is related to, well, mass. When considering that both gas and liquid velocities are not equal, the relation then comes into place by another property: flow quality ( $x_f$ ), which is based on mass flow ratio and can be obtained knowing the Slip Ratio (see section 1.3.2). This relation can be seen on the following equations:

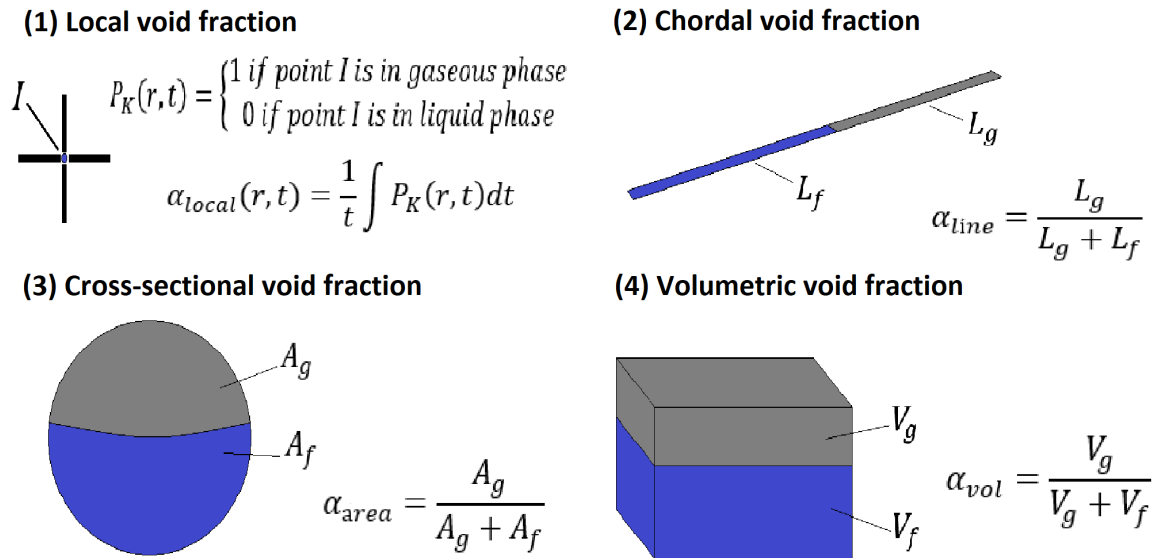


Figure 2 – Void fraction geometrical definitions: local (1), chordal (2), cross-sectional (3), volumetric (4) [4].

$$x_{st} \equiv \frac{M_g}{M_g + M_l} = \frac{A_g \rho_g}{A_g \rho_g + A_l \rho_l} \quad (1.2)$$

$$\alpha \equiv \frac{A_g}{A_g + A_l} = \frac{A_g}{A} = \left[ 1 + \left( \frac{1-x}{x} \right) \left( \frac{\rho_g}{\rho_l} \right) \right]^{-1} \quad (1.3)$$

$$x_f \equiv \frac{\dot{m}_g}{\dot{m}_g + \dot{m}_l} = \frac{u_g A_g \rho_g}{u_g A_g \rho_g + u_l A_l \rho_l} = \frac{x_{st}}{1 + \frac{1-x_{st}}{x_{st}} \frac{\rho_g}{\rho_l} S} S \quad (1.4)$$

$$\alpha = \frac{1}{1 + \frac{1-x_f}{x_f} \frac{\rho_g}{\rho_l} S} \quad (1.5)$$

We can also note that their values increasements behave quite differently. For example, a 0.1 void fraction value means we could have a 0.01 quality value, and if we had a 0.9 of void fraction value, the mass quality would be around 0.8. This value gets affected when the slip ratio is distinct from 1, altering the increasement behavior of the mass quality curve.

### 1.3 VOID FRACTION AND FLOW MODELS

Recalling that void fraction is based on the occupied space by the gas in a section and mass quality on the gas-phase mass quantity in a section, prediction of void fraction value relies on the flow behavior developed. The flow regime map establishes the shape and behavior of the areas and volumes of the phases. The gas concentration, the bubble size, the phase separation or dispersion, the dynamic viscosity difference between phases, whether if the velocities between phases are similar or not, these are all aspects that influence on the flow behavior. Due to this, there are different flow models for the analysis and prediction of the values of parameters such as the void fraction.

Void fraction correlations are generally classified in distinct groups related to the model they are based on. These groups are homogeneous model, slip ratio model, K $\alpha$ H model, drift flux model and miscellaneous or empirical model.

### 1.3.1 HOMOGENEOUS AND $K\alpha_H$ MODELS

The homogenous model considers that gas and liquid velocities are the same and it is represented by Eq. (1.6) [4]. Such model is the base for many other models since its void fraction (known as homogeneous void fraction) gets only modified by some constants.

$$\alpha_H = \left[ 1 + \left( \frac{1-x}{x} \right) \left( \frac{\rho_g}{\rho_l} \right) \right]^{-1} \quad (1.6)$$

In contrast,  $K\alpha_H$  models are correlations that derivate from the homogeneous model, which is defined as:

$$\alpha = K\alpha_H \quad (1.7)$$

Where  $K$  is a coefficient that modifies the homogeneous void fraction value.

### 1.3.2 SLIP MODEL

This model is based on the ratio of the gas velocity and the liquid velocity, in which it is assumed that the phases are separated with different velocities [4]. Thereby, void fraction can be defined as:

$$\alpha = \left[ 1 + \left( \frac{1-x}{x} \right) \left( \frac{\rho_g}{\rho_l} \right) S \right]^{-1} \quad (1.8)$$

where  $S = \frac{j_g}{j_l}$ .

Nevertheless, [Buttersworth \[5\]](#) proposed a correlation where the void fraction is a function of the ratios of gas and liquid mass qualities, the densities and the dynamic viscosities. Such function is described as follows:

$$\alpha = \left[ 1 + A \left( \frac{1-x}{x} \right)^p \left( \frac{\rho_g}{\rho_l} \right)^q \left( \frac{\mu_g}{\mu_l} \right)^r \right]^{-1} \quad (1.9)$$

Where  $A$ ,  $p$ ,  $q$  and  $r$  are constants whose values have been obtained in different studies. It must be said that these values are not the same for each correlation.



### 1.3.3 DRIFT FLUX MODEL

On a two-phase flow, bubble velocity consists of a superficial liquid velocity (also known as volumetric flux, in this case, of the liquid) component,  $j_l$ , a superficial gas velocity component,  $j_g$ , and a buoyance component. This theory was proposed by Nicklin [6] for slug flows and it got demonstrated by Zuber & Findlay [7] on annular and vertical slug flows. Such work resulted in an equation for void fraction that is a function of a distribution parameter,  $C_0$ , and the drift velocity,  $u_{gj}$ .

The drift velocity is the difference between the gas-phase velocity and the two-phase mixture velocity. On the other hand, the distribution parameter considers the lack of uniformity on certain parameters such as the mass quality, the density, the flow direction, among others. Together, these parameters make up for the drift flux model, which is similar to the slip model. It considers not only the difference between the phases' velocities, but also the buoyancy forces and it does not treat the phases independently. Thus, the generalized form of the void fraction in this model is defined as:

$$\alpha = \frac{j_g}{C_0 j + u_{gj}} \quad (1.10)$$

## 1.4 FLOW REGIME

To begin with, flow regime is crucial to know in order to determine properties that contribute to the void fraction calculation such as the volumetric flow. A perfect example to understand what the flow regime is, is that to know the flow regime in two-phase flow is the same as to know whether if the monophasic flow is laminar or turbulent. Since two-phase flow exact solutions currently do not exist, models for specific flow regimes to predict pressure drop, heat transfer and the volumetric flow have been developed. A method for this can be seen on the online video from Teresa Barrachina [8], which will be more detailed on section 4.1.1.

## 1.5 HYPOTHESIS

Since the void fraction is related to the mass quality, the cooling capacity calculation could be enhanced having the refrigerant flow conditions measured at the evaporator inlet. To suppose an isenthalpic process during the expansion might result in significant errors on the cooling capacity calculation. This could be resolved if the void fraction of the refrigerant at the evaporator inlet is known, as this parameter can be measured for an annular flow regime or a flow regime that is between bubbly and slug flow.

Such parameter shall be obtained through the development of a measurement technique for the characterization of the void fraction and the indirect determination of the mass quality on a gas compression evaporator system, particularly at the evaporator inlet after a sudden expansion. That way, a more precise determination of the cooling capacity on nowadays systems will be allowed since this is currently being calculated supposing an isenthalpic expansion process.

The first step to get into the area of refrigeration is the design of a cost-effective and easy-to-install sensor, which is yet another obstacle to surpass. A simpler and cheaper sensor design is believed to still work as good as many other complex sensor ever made in the determination of important factors of the two-phase flow, such as the void fraction and the flow regime.

## 1.6 OBJECTIVES AND OUTLINE

The present study proposes the development of a non-intrusive capacitive and an intrusive impedance void fraction sensor, (more detailed in section 1.6.1 and chapter 3) the examination of the zeotropic refrigerant R-404A during its phase change at an evaporator pressure of 375 kPa employing an air-water calibration facility, and the calibration of the proposed void fraction sensors with image analysis.

This is being done by making a comparison between the behavior of a pure substance and a zeotropic mixture being employed on a refrigeration system with simpler and low-cost sensors.

### 1.6.1 SPECIFIC OBJECTIVES

In order to validate the correct measurement of the void fraction, it is needed to design and construction an experimental facility for the high-speed camera in the refrigeration system at the evaporator inlet.

Firstly, the facility has to be designed and set up, beginning with the installation of the sight-glass at the evaporator inlet, where temperature, pressure and flowmeter sensors are located. Then, the high-speed camera's support is built and installed nearby the sight-glass, favoring some tests to get a good-quality image. Once the desired images are acquired, the first test for void fraction shall be performed. Thus, the void fraction, map flow and the collected data by the sensors will be acquired.

Moreover, along with the camera's setup, the capacitive electrode-based sensor is built. Before laying the electrodes in the experimental facility, the sensor was calibrated in a calibration test facility which has an air-water flow and was calibrated along with the void fraction captured and processed by the high-speed camera.

The same aforementioned process was followed for the impedance needle-probe sensor. However, the impedance sensor measures the local velocity of the flow, hence, the drift velocity was obtained immediately.

After that, the experimental results were analyzed and compared to the theoretical void fraction obtained by correlations, with the usage of the acquired data by the pressure, temperature and flowmeter sensors for each test done.

## 1.7 THESIS CHAPTERS DESCRIPTION

In order to achieve this work's objective, the first chapter is dedicated to present the motivation and main objectives of this thesis, as well as a brief review of some fundamental concepts and works in the field. Secondly, in chapter 2, a background about the two-phase flow and its measurement methods is brought in, as well as the construction, making and calibration process of the capacitance and impedance sensors are described with the purpose of validating such techniques. It is substantial to point out that the information in this section is related to the experimental facility and contrasted with published works by different authors.

In chapter 3, an explanation of the construction of experimental facilities is described, detailing the manipulation of the equipment and the specifications of them. Next, in chapter 4 the experimental tests are then redacted among the processing of the collected data. Results and their analysis are written and explained in chapter 5 via the operated instrumentation, finishing with the final conclusions and further studies on chapter 6. Lastly, references and nomenclature presented in this paper are shown at the end of every chapter <sup>1</sup>.

---

<sup>1</sup>The superscript red letter (*a,b,c...*) in the 'References' sections is a return root for the reference in the exact page where it was mentioned.

## 1.8 NOMENCLATURE

$A$	Area, [m <sup>2</sup> ]
$C_0$	Distribution parameter
$j$	Superficial velocity, [m/s]
$K$	Homogeneous void fraction constant modifier
$L$	Length, [m]
$P_k$	Local phase point value
$S$	Slip ratio
$t$	Time, [s]
$u$	Velocity, [m/s]
$u_j$	Drift velocity, [m/s]
$V$	Volume, [m <sup>3</sup> ]
$x$	Mass quality
 <i>Greek letters</i>	
$\alpha$	Void fraction
$\rho$	Density, [kg/m <sup>3</sup> ]
 <i>Subscript</i>	
$g$	Gaseous phase
$H$	Homogeneous
$l$	Liquid phase

## 1.9 REFERENCES

- [1] Gardenghi, L. R., Filho, E. D. S., Chagas, D. G., Scagnolatto, G., Oliveira, R. M., & Tibiriçá, C. B. (2020). [Overview of Void Fraction Measurement Techniques, Databases and Correlations for Two-Phase Flow in Small Diameter Channels](#). *Fluids*, 5(4), 216. <sup>a</sup>
- [2] Wojtan, L., Ursenbacher, T., & Thome, J. R. (2005). Measurement of dynamic void fractions in stratified types of flow. *Experimental Thermal and Fluid Science*, 29(3), 383–392. <https://doi.org/10.1016/j.expthermflusci.2004.05.017> <sup>a</sup>
- [3] Portillo, Guillermo; Shedd, Timothy A.; and Lehrer, Kathryn H., "Void Fraction Measurement in Minichannels with In-Situ Calibration" (2008). International Refrigeration and Air Conditioning Conference. Paper 887. <http://docs.lib.purdue.edu/iracc/887> <sup>a</sup>
- [4] WOLVERINE TUBE, INC. (s. f.). Void Fractions in Two-Phase Flows. Research Gate. <http://www.thermalfluidscentral.org/e-books/pdf/edb3/20.pdf> <sup>a b c d</sup>
- [5] Butterworth, D. (1975). A comparison of some void-fraction relationships for co-current gas-liquid flow. *International Journal of Multiphase Flow*, 1(6), 845–850. [https://doi.org/10.1016/0301-9322\(75\)90038-5](https://doi.org/10.1016/0301-9322(75)90038-5) <sup>a</sup>
- [6] Nicklin, D. J., Wilkes, J. O. and Davidson, J. F., Two-Phase Flow in Vertical Tube, *Trans. Instn. Chem. Engrs.*, Vol. 40, 61-68 (1962). <sup>a</sup>
- [7] Zuber, N., & Findlay, J. A. (1965). Average Volumetric Concentration in Two-Phase Flow Systems. *Journal of Heat Transfer*, 87(4), 453–468. <https://doi.org/10.1115/1.3689137> <sup>a</sup>
- [8] Universitat Politècnica de València - UPV. (2017, October 19). MAPA DE REGÍMENES DE CAUDAL BIFÁSICO EN TUBERÍAS VERTICALES — — UPV [Video]. YouTube. [https://www.youtube.com/watch?v=lJL2249d0EM&ab\\_channel=UniversitatPolit%C3%A8cnicaVal%C3%A8ncia-UPV](https://www.youtube.com/watch?v=lJL2249d0EM&ab_channel=UniversitatPolit%C3%A8cnicaVal%C3%A8ncia-UPV) <sup>a</sup>

## CHAPTER 2

# INSTRUMENTATION AND EQUIPMENT BACKGROUND

---

Two-phase flow can be described by any of the aforementioned flow models in section 1.3. However, the mathematical definitions of the phases play an important role on the results of the flow characterization, making the coupling between the phases the main issue that affects the quality of the results.

A good comparison does not only rely on the void fraction measurement, but also in the flow regime identification and the velocities of the phases. Therefore, in this chapter void fraction measurement methods are mentioned, as well as the pros and cons they have.

## 2.1 VOID FRACTION MEASUREMENT METHODS

There are several methods for the measurement of the void fraction. There are methods based on conductivity, capacitance, optometry, beams (such as X-ray,  $\gamma$ -ray or neutron beams), ultrasonic, magnetic resonance, to name some. In most of them, parameters as the flow rate, pressure and/or temperature are required to work. These methods can also be used to obtain the flow regime.

Gardenghi et al. [1] made a comparison between many void fraction measurement techniques and their utilized correlations. This work pointed out that, optical techniques such as image capture, have a great precision on spatial and temporal resolution and, while the best functionality is at low mass qualities, it is a very reliable technique. Conversely, capacitance sensors have a similar precision from that of image analysis, though they are intrusive depending on the type. Also, a previous calibration is needed through other measurement techniques such as image analysis or QCV, which is the same problem encountered in most of the other measurement techniques.

## 2.2 IMAGE ANALYSIS METHOD

This kind of digital signal analysis focuses on an outlet signal that comes in form of a pixelated image. Within the image there is a lot of information that can be extracted. Image analysis methods are widely utilized on the two-phase flow associated phenomena study.

There are many techniques that can be employed for the image processing, e.g., edge detection, pattern recognition, cross and auto correlation, among others. To sum it up, there are direct and advanced techniques, where the first category are the most common and employ high-speed cameras, taking pictures with a minimum resolution of 600x600. This is due to the small diameter of the bubbles, the need of capturing as many images per second as possible (at least 30 per second) and its velocity. In addition, these direct visualization techniques are employed for the easy calibration of other measurement methods.

On the second category, the advanced techniques are usually based on the usage of laser beams. These techniques are useful for flows where there is a high amount of bubbles. A well-known technique is the Particle Images Velocimetry (PIV), which is one of the most expensive measurement techniques. An alternative technique is the interferometry, since it is less complex and it relies on the sensing of the beam's intensity.



### 2.2.1 HIGH-SPEED CAMERA

One of the most efficient non-intrusive techniques for void fraction measuring is the image analysis utilizing high-speed cameras, though its costs are quite a deal, it is an 'accessible' direct visualization technique. Still, a frequent issue with it is the image capturing, since noise and other quality issues might be present in the images captured. Another issue found in this technique is that it might present some troubles when measuring a flow of a high density of bubbles.

Many methods that solve these issues have been made, whether it is done in the process of image capture or in the image processing. Widyatama [9] focused on the development of image processing technique wielding MATLAB. This technique enhanced contrast and removed the irregular background. Other methods to obtain better image quality involve illumination such as focused illumination, monochromatic laser [2], fluorescent flow dyeing [10] or special 3-D printed structures.

With these techniques both flow regime and superficial gas velocity can be known. The former by association and gas distribution rate. The latter, by following the histogram and path of a bubble in addition of its traveling time.

## 2.3 CAPACITANCE SENSOR

If in a two-phase flow both phases have different electrical permittivities, then its difference have an effect on the flow capacitance, leading to a change in the inductance generated through the tube.

There are quite a lot of types of capacitance sensors. The first ever made wire-mesh sensor was introduced by Prasser et al. [11] in 1997, and it is still being used in two-phase flow systems. Even though it has a great precision, it is very intrusive, and it may cause a considerable pressure drop, as well as it can change the bubble velocity and shape, so it is pretty rare to find it on small diameter tubes.

There are some ways, however, to measure void fraction with a capacitive sensor through non-intrusive techniques. One of them is via Electric Capacitance Tomography (ECT). Roman et al. [12] utilized this technique to measure R-134a void fraction changes after a sudden expansion, as well as it was also utilized a high-speed camera for two area ratios (0.145 and 0.44). The void fractions determined from the correlations were compared with experimental measurements, but none of them succeeded on depicting the void fraction behavior. Given that, they proposed a modified correlation capable to predict it on an error range of  $\pm 20\%$  in contrast with the experimental data at a mass flow from 50 to 250 kg/m<sup>2</sup>s

### 2.3.1 CAPACITANCE ELECTRODE-BASED SENSOR

There are other techniques for capacitance-based void fraction measurement with lower installation and, namely, acquisition difficulties, such as the one described by Abouelwafa & Kendall [13] for the first time in 1980. In their work, they made a variety of sensor designs capable of measuring in situ void fractions without interfering with the flow, where the designs had parallel, concave, double helix, multiple helix and four concave plates that functioned as sensing electrodes.

A recent study on this type of sensor was made by Qian H. & Hrnjak P. [14], where they named the sensor as a capacitance electrode sensor. They proposed and built some capacitive electrodes with different axial lengths (D, 2D/3 and D/2), utilized to measure the void fraction at a mass flow of 40 kg/m<sup>2</sup>s in cylindrical tubes with a 7 mm inner diameter. The thrice of them presented a satisfactory measurement capacity with a negligible difference between them. Given the results, it is an advantage to take in consideration in this present work the implementation of the capacitance sensor as the testing tube has similar dimensions to the described tube and, in particular, it is easy and low in cost to implement.

This sensor is a capacitive plate mounted around a tube, working as electrodes, in which the affected impedance variation due to the capacitance change is measured,

and such effect can be contemplated in Eq. (2.1) in its rectangular form.

$$Z = R + \frac{1}{j\omega C_{flow}} \quad (2.1)$$

Since the electrodes send an electrical current through the tube, the capacitance is dependant on the relative permittivity of the tube material and the electrodes  $\varepsilon_r$  and the flow permittivity  $\varepsilon_f$ . The last one only changes depending on the spatial amount of the phases, and it can be seen that, theoretically, this is the only parameter that is not constant.

$$C_{flow} = \frac{\varepsilon_r \varepsilon_f A_{elec}}{d_{elec}} \quad (2.2)$$

Where  $A_{elec}$  is the area of the electrode and  $d_{elec}$  is the distance between both electrodes. Since the surroundings of the tube may affect the capacitance due to electromagnetic effects, that part of the tube is usually electrical isolated with dielectric materials.

## 2.4 ELECTRICAL PROBE SENSORS

Different from the capacitance sensors, the impedance probe sensors function principle is based on admittance and capacitance, making the phases' electrical properties the protagonists in these parameter measurements, since the impedance ( $Z$ ) can be expressed as follows:

$$Z = \frac{1}{G_m} + \frac{1}{j\omega C_m} \quad (2.3)$$

Where  $\omega$  is the angular frequency of excitation the conductance and the capacitance are described as follows:

$$G_m = \frac{\sigma_m A_{probe}}{l_{probe}} \quad (2.4)$$

$$C_m = \frac{\varepsilon_m A_{probe}}{l_{probe}} \quad (2.5)$$

Where  $\sigma_m$  is the conductivity of the mixture.

Depending on how the probes and flow properties behave, the impedance could be either affected by both conductance (resistive) and capacity (reactance) parts or merely influenced by only the conductance or the capacitance, making the impedance of the probe mainly active or reactive.

### 2.4.1 IMPEDANCE NEEDLE-PROBE SENSOR

The first comparison between the mesh capacitance sensor and the needle impedance sensor was made by [Manera et. al. \[15\]](#) in 2007. In their work, they measured and compared the void fraction in a 2" (50.8 mm) pipe at gas and liquid phase velocities of 0.036 to 2.089 m/s and 0.647 to 2.554 m/s, respectively. A recent study made by [Chakraborty & Prasanta \[16\]](#) in 2019, on a 2" diameter tube, measured the void fraction of a flow by means of an impedance sensor and various optical sensors. A volumetric flow variation of 0.2 to 75.9 m<sup>3</sup>/h and 0.12 to 1.44 m<sup>3</sup>/h of air and water, respectively, was made in this work.

In both studies, a double impedance probe was utilized. This kind of technique, besides measuring void fraction, allows to measure the bubble velocity, which means it can get the gas-phase velocity, and the size and dimensions of it. It consists on a small and thin electrode (usually a needle) inside a capillary tube (which functions as a physical earth for the circuit) and it is generally excited by an AC current.

If a bubble pass through one of the two needles, then the needle's local impedance changes and the current is affected, rising its value and thus generating a signal amplitude that is inversed into a DC current signal by an electronic circuit. Since both needles are very close to each other, almost always the same bubble will touch the other needle. Having then one of the needles separated in a specific length from the other would make two signals with a gap between them. With the aforementioned information, with the signals correlated and the time gap, a shift signal time value can be calculated in order to maximize the correlation function as stated by [Mendez et. al. \[17\]](#):

$$F_{V_1V_2}(\tau) = \frac{1}{t_s} \int_0^{t_s} V_1(t)V_2(t - \tau)dt \quad (2.6)$$

Where  $t_s$  is the sample time and  $V_1$  and  $V_2$  are the probes voltages. After that, the bubble velocity can be calculated as follows:

$$u_b = \frac{d_{ndl}}{\tau_{max}} \quad (2.7)$$

Where  $d_{ndl}$  is the distance between the tips of the needles.

## 2.5 ISSUES ON MEASUREMENT

A problem that has to be considered when building the experimental facility is the presence of vibration due to inertia effects inside the tubes. These effects alter the results when comparing theoretical with experimental data. [Zhou et al. \[18\]](#) considered a non-linear oscillation over a wide range of vibration parameters, measuring the void fraction with a high-speed camera and an electric impedance sensor. The vibrations had amplitudes of 0 mm at 0 Hz, 2 mm at 2 Hz, 2 mm at 5 Hz and 5 mm at 10 Hz for a liquid and gas flow rate of 0 to 5 m<sup>3</sup>/h and 0.1 to 35 m<sup>3</sup>/h respectively. The void fraction prediction effectivity of the selected correlations, based on the three typical flow models, was pretty low and differed a lot from the experimental measurement. Taking this into account, any vibration presence on the system that could potentially alter the results must be solved in order to prevent errors in the conclusions when comparing theoretical and experimental results.

## 2.6 NOMENCLATURE

A	Area, [m <sup>2</sup> ]
C	Electrical capacitance, [F]
D	Tube diameter, [m]
$d_{ndl}$	Needles tips gap, [m]
G	Conductance, [S]
$l$	Length, [m]
R	Resistance, [ $\Omega$ ]
t	Time, [s]
$u_b$	Bubble velocity, [m/s]
Z	Impedance, [ $\Omega$ ]
 <i>Greek letters</i>	
$\varepsilon$	Electrical permittivity, [F/m]
$\sigma$	Electric conductivity, [S/m]
$\tau$	Gape time, [s]
$\omega$	Angular frequency of excitation, [rad/s]
 <i>Subscript</i>	
$f$	Flow
m	Mixture

## 2.7 REFERENCES

- [1] Gardenghi, L. R., Filho, E. D. S., Chagas, D. G., Scagnolatto, G., Oliveira, R. M., & Tibiriçá, C. B. (2020). [Overview of Void Fraction Measurement Techniques, Databases and Correlations for Two-Phase Flow in Small Diameter Channels](#). *Fluids*, 5(4), 216. <sup>a</sup>
- [2] Wojtan, L., Ursenbacher, T., & Thome, J. R. (2005). Measurement of dynamic void fractions in stratified types of flow. *Experimental Thermal and Fluid Science*, 29(3), 383–392. <https://doi.org/10.1016/j.expthermflusci.2004.05.017> <sup>a</sup>
- [9] Widyatama, A., Dinaryanto, O., Indarto, & Deendarlianto. (2018). The development of image processing technique to study the interfacial behavior of air-water slug two-phase flow in horizontal pipes. *Flow Measurement and Instrumentation*, 59, 168–180. <https://doi.org/10.1016/j.flowmeasinst.2017.12.015> <sup>a</sup>
- [10] Huang, L., Wen, S., Liu, Y., Lin, Z., & He, Z. (2020b). Development of a fluorescence imaging method to measure void fractions of gas–liquid two-phase flows in a small tube-window for transparent fluids. *Measurement Science and Technology*, 31(4), 045301. <https://doi.org/10.1088/1361-6501/ab4dee> <sup>a</sup>
- [11] Manera, A., Prasser, H. M., Lucas, D., & van der Hagen, T. (2006). Three-dimensional flow pattern visualization and bubble size distributions in stationary and transient upward flashing flow. *International Journal of Multiphase Flow*, 32(8), 996–1016. <https://doi.org/10.1016/j.ijmultiphaseflow.2006.03.005> <sup>a</sup>
- [12] Roman, A. J., Ervin, J. S., & Cronin, J. (2020). Studies of two-phase flow through a sudden expansion using electrical capacitance tomography. *International Journal of Refrigeration*, 119, 206–215. <https://doi.org/10.1016/j.ijrefrig.2020.07.002> <sup>a</sup>
- [13] Abouelwafa, M. S. A., & Kendall, E. J. M. (1980). The Use of Capacitance Sensors for Phase Percentage Determination in Multiphase Pipelines. *IEEE Transactions on Instrumentation and Measurement*, 29(1), 24–27.

<https://doi.org/10.1109/tim.1980.4314856> <sup>a</sup>

[14] Qian, H., & Hrnjak, P. (2020). Mass measurement based calibration of a capacitive sensor to measure void fraction for R134a in smooth tubes. *International Journal of Refrigeration*, 110, 168–177. <https://doi.org/10.1016/j.ijrefrig.2019.10.019> <sup>a</sup>

[15] Manera, A., Ozar, B., Paranjape, S., Ishii, M., & Prasser, H. M. (2009b). Comparison between wire-mesh sensors and conductive needle-probes for measurements of two-phase flow parameters. *Nuclear Engineering and Design*, 239(9), 1718–1724. <https://doi.org/10.1016/j.nucengdes.2008.06.015> <sup>a</sup>

[16] Chakraborty, S., & Das, P. K. (2020). Characterisation and classification of gas-liquid two-phase flow using conductivity probe and multiple optical sensors. *International Journal of Multiphase Flow*, 124, 103193. <https://doi.org/10.1016/j.ijmultiphaseflow.2019.103193> <sup>a</sup>

[17] Méndez, S. (2008) *Medida experimental de la concentración de área interfacial en flujos bifásicos finamente dispersos y en transición* [Doctor's degree thesis, Universitat Politècnica de València] Repositorio Institucional de la Universitat Politècnica de València. <https://riunet.upv.es/bitstream/handle/10251/3301/tesisUPV2899.pdf> <sup>a</sup>

[18] Zhou, Y., Chang, H., & Lv, Y. (2019). Gas-liquid two-phase flow in a horizontal channel under nonlinear oscillation: Flow regime, frictional pressure drop and void fraction. *Experimental Thermal and Fluid Science*, 109, 109852. <https://doi.org/10.1016/j.expthermflusci.2019.109852> <sup>a</sup>



# EXPERIMENTAL FACILITIES

## CONSTRUCTION

---

The experimental process has to go through some testing and calibration steps in order to achieve the desired results. On the first facility, the high-speed camera is tested with an economical liquid sight-glass that has a plain circular axial glass. The calibration facility utilizes of a cylindrical pyrex sight-glass, since all the checked literature by the authors make use of this kind of sight-glass or a similar one. Then the calibration facility is setup so the sensors get calibrated along with the image analysis of the camera.

### 3.1 VISUALIZATION TEST FACILITY

The first facility consists on a Danfoss HJZ022D40N condenser unit with a refrigerant charge of 2.8 kg, and a Bohn LET120BCS evaporator unit with a cooling capacity of 3.5168528 kW-h. A brass CASTEL® type SG 1/2" liquid sight-glass is installed in the middle of the solenoid valve outlet, which is a Danfoss 034G5130 ETS 6 solenoid-controlled expansion valve, and the evaporator outlet to visualize the liquid-gas flow, [Fig. 3](#). It was measured in parallel the evaporator inlet pressure (right before the sight-glass, so that it would not affect the flow regime) and

the temperature at the same point with a pressure transducer and a RTD PT1000 temperature sensor in order to compare the experimental data against theoretical data.

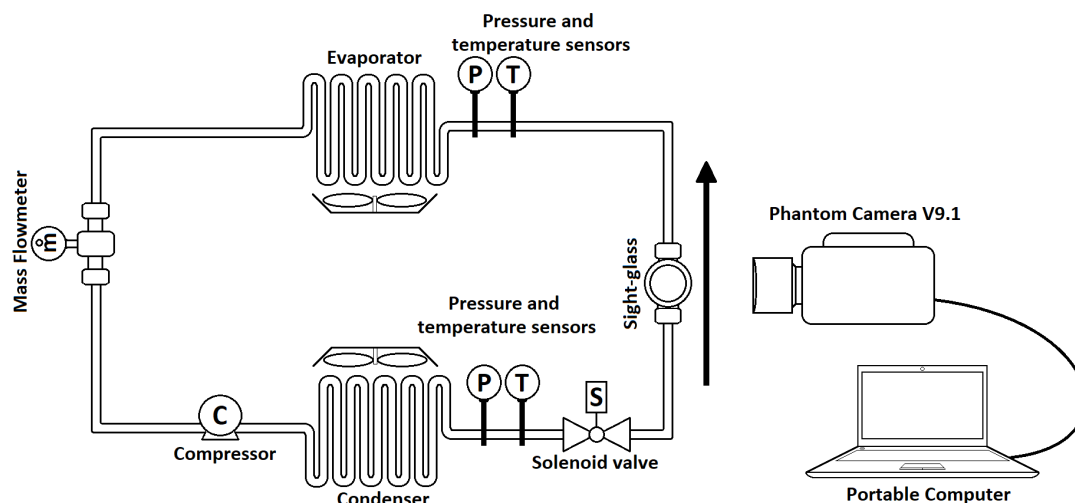


Figure 3 – Visualization testing facility diagram.

Mass flux is measured by an Emerson/Micro Motion CMFS015M319N0A2SCZZ Coriolis mass flowmeter at the evaporator outlet. Finally, a Phantom V9.1 is manipulated to acquire images from the sight-glass.

Results of the void fraction were achieved with little error compared with some correlations, however, superficial gas velocity could not be measured. This is due to the internal geometry of the sight-glass, since there it has a rectangular section that, when the flow passes through, it is dispersed and it collides with the walls. Although it is symmetric (and thus void fraction could be achieved for some models), this collision made a mess with the bubble correlation of position, which is used to calculate the superficial gas velocity, by displaying due to inertia a 'counter-current' flow in the glass, overlapping both bubble flows. Hence, only homogeneous, K-model and Slip models could be taken into account for correlation comparison. A work about this was previously done by the authors and results can be seen on [Silva-Alvarado et. al. \[19\]](#).

## 3.2 CALIBRATION TEST FACILITY

Since the experimental facility replicates an ordinary air conditioning system, the expansion valve is quite near to the evaporator inlet, so it is not recommended to install more than one sensor at time. Not because of the weight, but because the pressure loss affects greatly the efficiency of the system and the superheat would be high and thus energy will be gained, interfering in the cooling process as condensation and frosting may occur. Knowing this, a calibration facility is needed.

It is not usual that in-situ calibrations are made due to the complex process it takes to get a model of calibration, since it is not only about measuring the void fraction, but also the identification of flow regimes and, depending of the sensor, measurement of velocities. There are few works on this, yet. An example is [Portillo et. al. \[3\]](#) who made an in-situ calibration of a capacitance sensor with R-410A. Though this procedure was a success, working at a normalized capacitance value, it is attained to the homogeneous void fraction model at low quality values. The authors mention that this procedure makes the capacitance sensor fit the data values to those of [Rouhani \[20\]](#) void fraction correlation model.

Notwithstanding this, it presented good and reliable results. The calibration procedures by means of image analysis or by QCV are more precise and can identify flow regimes as well as measure velocities at least by the date of this work. Surely an in-situ calibration can be made, nonetheless, this is not the objective of this study.

That said, a calibration facility is build with a 1/4 HP (186.425 W) centrifugal pump and a 1/2 HP (372.85 W) gas compressor, moving two flows in separated channels with their respective flowmeters and pressure sensors at room temperature. Next, both fluids are mixed and flow through a 3/4" (19 mm) copper tube. After more than 10 diameters of distance, so the flow is fully developed, it is analysed by direct visualization and then either the capacitance sensor or the impedance needle-probe sensor, being these two calibrated by the image analysis after the data

captured by the high-speed camera. This process is explained in Chapter 4. Details of the diagram are presented in Fig. 4.

The facility is operated with air and water as the working fluids. Though their thermophysical properties are truly distinct from those of R-404A, the capacitance, which is the responsible for the impedance variations, is not so different, as it has a range difference of only  $6 \mu\text{F}$ . This may or may not be a problem, but it has not been proved by the time of the making of this study.

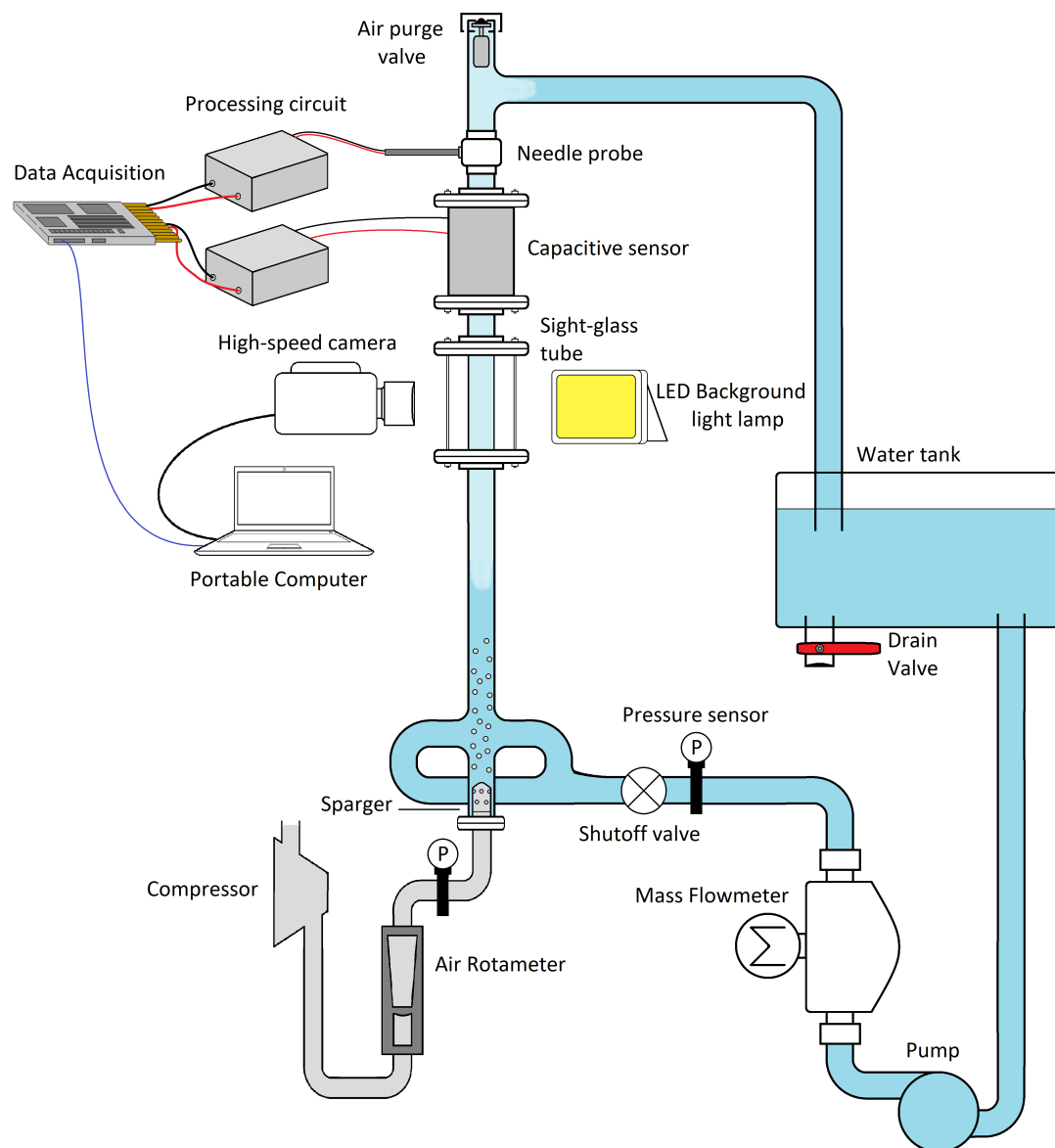


Figure 4 – Calibration test facility.

The flow mixture is, as presented in Fig. 5, with a setup of a 4-way connection, where the lower part has a stainless steel air sparger. For the sparger section, there are two perpendicular inlets of water via a 4-way matching tube so the section can be filled up smoothly, air bubbles can be mixed before and the flow stays mixed when encountering with the 4-way connection. An even more detailed diagram is depicted in Chapter 4.

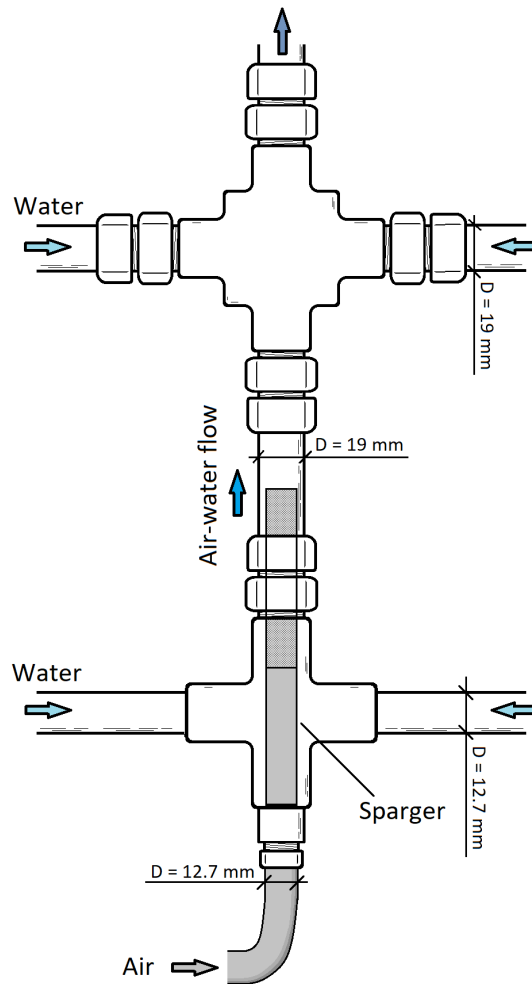


Figure 5 – Air-water mixing section with sparger.

Another important consideration on this facility is that the capacitance and impedance sensor are switchable by using flare couplings. The purpose of this decision is that the flow that goes through the test section has to be similar to the next sensing section, making it a challenge if the travel is long, as the flow will change eventually, so three sections are not plausible.

### 3.3 IMAGE CAPTURE SECTION CONSTRUCTION

Image analysis method by image capture is neither that challenging to manage, nor tricky to install. In fact, it only needs a sight-glass and a camera to work out well. It is the control of the camera and analysis parts that present the challenges for any beginner on this area.

The facility has a 3/4" (19 mm) with an 15 mm inner diameter pyrex sanitary sight-glass tube with a visible length of 87 mm (Fig. 6). On this tube, since it has a clamp connection, a clamp to 3/4" (19 mm) MNPT connection is adapted, as it can be easily exchanged between facilities utilizing flare connections.

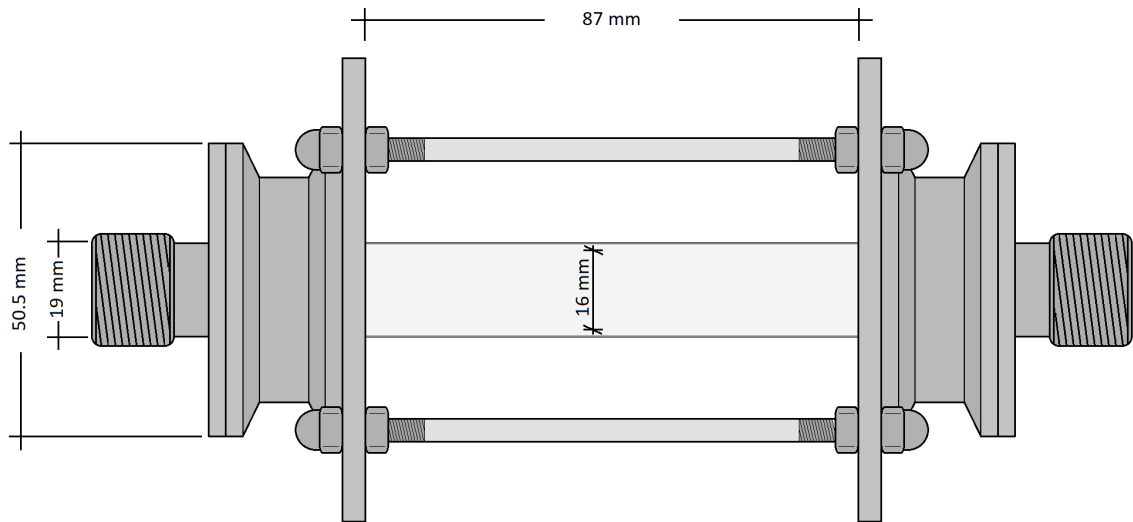


Figure 6 – Sanitary sight-glass section diagram.

The camera's distance from the target has to be fixed so the configuration does not need to change much in parameters such as brightness, definition, among others. A LED light lamp is set at the background to illuminate the flow as well (Fig. 4).

## 3.4 CAPACITANCE SENSOR CONSTRUCTION

As said in Chapter 1, the capacitance sensor is an electrode type. Most of these kind of sensors are based on the sensor developed by [Canière et. al. \[21\]](#) in a 9 mm tube. The sensor construction is based on the one seen in [Qian H. & Hrnjak P. \[14\]](#).

For the construction, it is needed a flexible circuit material to construct the tube wall, since its material and low thickness (usually between 0.1 and 0.05 mm) make its conductance really high, as well as its nature of extremely low moisture absorption maintain electrical, mechanical and dimensional properties in humid environments. Then, the two electrodes are placed over the circuit material with an even separation between both ends.

For mechanical stability, the inner tube with electrodes is placed within an outer grounded metal shielding tube, that also eliminates the influence of the environment as well, and the space between the tubes is filled with an electrical isolator.

### 3.4.1 THE CONSTRUCTION PROCESS

First, the core of this sensor had to be made, since everything depends on the material's capacitive impedance. That said, a 0.102 mm thick CLTE MW Laminate<sup>TM</sup> material, which was donated by ROGERS CORPORATION [\[22\]](#), is employed as the tube section of the sensor itself and as the electrodes utilized in the tube's surface to pass through the high frequency signal. This is easily achieved through acid etching technique, which consists of the remotion of the copper in both sides of the laminate utilizing an acidic solution on the laminate. The circuit has to be drawn in the laminate with a photoresistive material (like the ink of a printer or permanent marker ink) on both sides of the laminate. This process is known for being 'slow' and sometimes the photoresistive material may cease to the acid, so tiny scratches of lost copper might appear ([Fig. 7](#)). These problems can be easily solved as follows.

The circuit of the electrodes are printed into a sheet of white adhesive viynil for a better ink printing on the laminate. The printing on the vinyl was made through the usage of a ink injection printer, but it can be done with a laser printer too. Then, the sheet is printed into the laminate utilizing heat to transfer the ink to the laminate. This was achieved almost perfectly with an electric iron, passing it at each direction for a better printing. Some of the ink might not make it, but this can be solved filling the voids with permanent marker.



**Figure 7 – Failed etching resulting in a scratched laminate. Waiting too much time may cause the ink to be removed and end up with scratches.**

After the circuit is printed in both sides of the laminate, it is then immersed into an acid solution of iron(III) chloride ([Fig. 8](#)), also known as ferric chloride ( $\text{FeCl}_3(\text{H}_2\text{O})_x$ ; not ferrous chloride  $\text{FeCl}_2$ , since its composition is different). Some may recommend to wait about 30 to 40 minutes for the acid to remove the unprotected copper, but a better result comes when stirring the acid, as it takes less time (less than 4 minutes) and it prevents the acid from overcoming the photoresistive material. Thus, the circuit is drawn, cleaned with water and then the ink is removed with either ethy alcohol, acetone or thinner. The result was highly plausible as it can be seen in [Fig. 9](#).





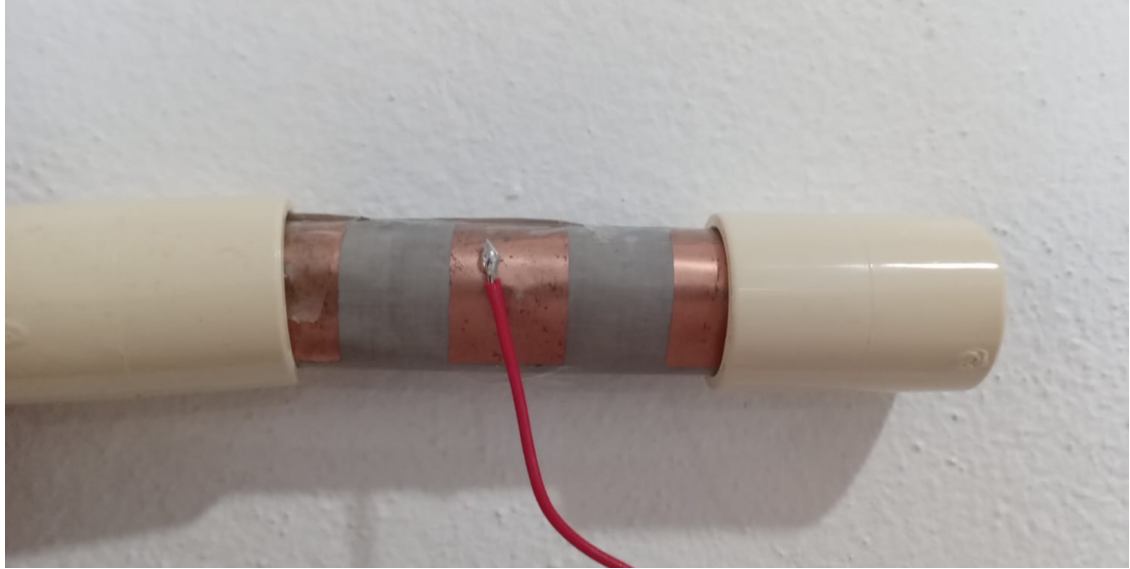
Figure 8 – Laminate immersed in  $\text{FeCl}_3(\text{H}_2\text{O})_x$



Figure 9 – Electrodes made in the laminate by etching technique. All electrodes have a length of one diameter and a radial length of  $160^\circ$ . The electrodes in the center are used for signal transmission and the electrodes at the corners are grounded for better results [21].

Then, the piece of laminate is rolled into the shape a 19mm tube. An electrode angle ( $\beta$ ) of  $160^\circ$ , which it is the radial length of the electrodes, was approximately

gotten as it was intended with the printed circuit and the separation between electrodes was almost equal to  $20^\circ$  in both sides. The tube section is held still with a CPVC coupling at each side (Fig. 10).



**Figure 10 – Tube section held by and attached to CPVC coupling**

The metal shielding is made of a 1 mm thick aluminum sheet (Fig. 11) and, after some drillings and bendings, the shielding consists of two curved sheets with covers at each side, all united with nuts and bolts. The substance utilized to protect the signal from the environment was hot-melt adhesive (colloquially referred as hot glue), which it functions as a good isolator, specially since the thickness is quite large. Nonetheless, it has to be poured at almost  $140^\circ\text{C}$ , which it is quite a problem as some air bubbles can be trapped inside the substance as it solidifies quickly at ambient temperature.

To avoid this, a room at the same level shall be optimal. Since CPVC does not ignite at  $140^\circ\text{C}$  [23], and the isolation of the electrodes cables do not burn as well, the sensor is placed inside a gas oven (Fig. 12) at around  $140^\circ\text{C}$  over a glass refractory baking tray. This is due to it being made of Pyrex and that it does not conducts electricity, so it is safe to manage.



**Figure 11 – Aluminum shielding of the capacitance sensor.**



**Figure 12 – Hot glue being melt inside the capacitance sensor. It can be seen that the sensor was placed at the top level for a slow and smooth heat transfer.**

The schematic of the sensor can be seen on [Fig. 13](#). It is important to note that everything is put together by mechanical force, since soldering is not an option. Soldering a thin layer to a thick copper tube is quite a challenge since the layer can be burnt away, but the true reason for not soldering both tubes is that part of the

signal may be lost. That said, employing CPVC will not only be easier to attach, but also to restrain the signal from choosing another electrical path.

After cooking the sensor, it was ready to go and be attached to the calibration facility. If any fault occurs in the electrodes, the shielding can be easily unscrewed and the hot glue can be removed.

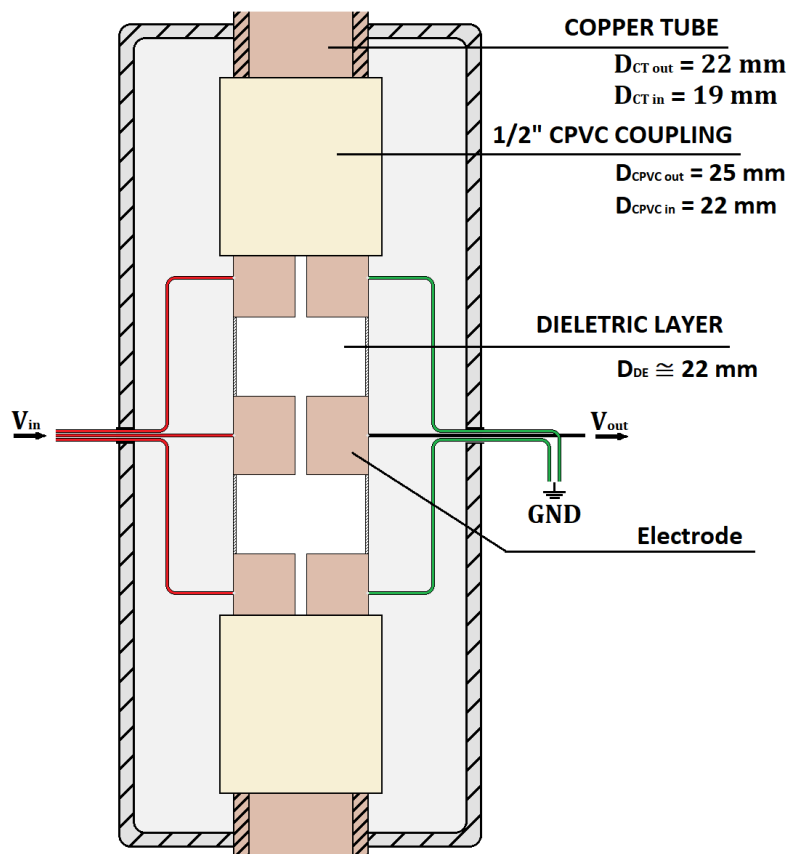


Figure 13 – Capacitance sensor schematic.

From Fig. 13 it can be seen that output electrodes are grounded. This is known as the active guard technique, where two sets of shield electrodes at the sides of the sensing electrodes are grounded to focus the electric field to a known volume. Otherwise, an effect known as fringing occurs, where the electric field lines will jump to other nearby electrodes. This technique was utilized by [Canière et. al. \[21\]](#).

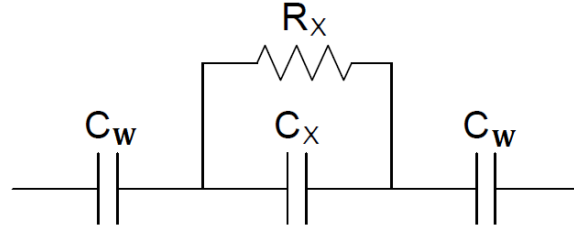


Figure 14 – Equivalent electrical RC circuit of the capacitance sensor.

The equivalent RC circuit of the sensor is represented then as in Fig. 14, where the impedance of the flow is depicted as the parallel of  $R_x$  and  $C_x$  and the capacitance of the tube section wall is  $C_W$ , since the resistivity of the tube section wall is really high and thus can be ignored. Nonetheless, as the laminate has a negligible conductivity, the capacitance of the flow is in series with the wall, making the measured capacitance  $C_m$  be determined as follows:

$$C_m = \left( \frac{1}{C_W} + \frac{1}{C_x} \right)^{-1} = \frac{C_W C_x}{C_W + C_x} \quad (3.1)$$

### 3.5 IMPEDANCE NEEDLE-PROBE SENSOR CONSTRUCTION

Impedance probe sensors have their working principle based on the significant difference in conductivity between both phases. There are many arrangements for this sensor, from double-rod (Liu et. al. [24]), to four-rod (Shen & Nakamura [25]), five-rod (Euh et. al. [26]), and even 4x4 (Hosokawa et. al. [27]) and 5x5 (Ren et. al. [28]) rod bundles. However, since most of these big arrangements are done in wide sections and in our facility the section, though it may not be a capilar tube, it is a small tube compared to the usual 2" (50.8 mm) diameter, so size is a matter due to many geometrical and sensing issues.

Consequently, it is plausible to use a double or four-rod arrangement. There have been some works issuing uncertainty and error problems such in Shen et. al. [29], Wang et. al. [30], Satou et. al. [31]. The last one has remarkable highlight, where Satou et. al. [31] investigated the effect of the meniscus in the error of velocity measurement due to interface deformation on horizontal tubes, utilizing a four-rod and a two-rod impedance probes. They pointed out that size, shape and coating of the sensor affect the error in the measurement.

For simplicity, a double-rod sensor is made on this work. This kind is a practical and reliable measurement technique that has been widely used in many flow regimes and situations (Herringe & Davis [32], Wu & Ishii [33], Revankar & Ishii [34]). This probe consists on two electrically insulated thin needles whose tips are not insulated and separated from the insulated parts. The needles have a known distance between them and they are soldered from the base with thin copper wire (Fig. 15). The signals that the probe send are recorded by the probe circuit and DAQ system.

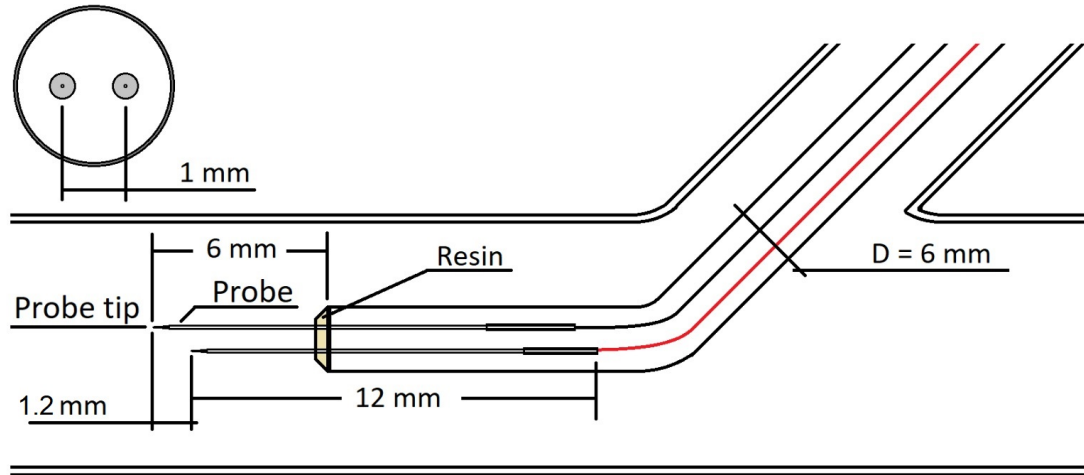


Figure 15 – Impedance Needle-probe Sensor schematic.

A probe is made of a stainless-steel surgical needle made of stainless steel, whose base is soldered with a 24 AWG (0.511 mm) insulated copper wire. The probes are separated by a distance of 2 mm and 1 mm between the needles and the tips respectively, to ensure the time difference between the rise of their signals and

the duration of them. They are put in place with epoxy resin and coated with K-12 dielectric coating inside a 6 mm stainless steel tube of 250 mm long.

### 3.5.1 THE CONSTRUCTION PROCESS

Making an impedance needle-probe sensor is kind of an easy task, though the most difficult part is the assembly of this to the facility. Usually, many would put the sensor inside a huge tube section that is not difficult due to the transversal area being this size and thus not affecting the flow, but that is usually done in the area of fission reactors. Another option would be to make a 3-D printed section or acrylic-milled box sections, which are good options that can be implemented for smaller tubes. However, their elaboration is pretty difficult and the process lasts a lot; the cost of making these sections is high and, if something goes wrong or breaks, it can be laborious to fix it.

On this work, a different technique is proposed. Many people who have worked in the area of refrigeration, plumbery or related, know about the 'Tee union', and this could be implemented instead of the previous assemblies. Nonetheless, it may be hard to pull off because of the 90 degree angle the sensor would have, so fitting it is possibly an impossible task. Yet, there is a way to make this, not with a Tee union, but with a 'Yee union' (Fig. 16). This union has a 45 degree angle connection where the sensor can easily pass through, making this a possible great replacement for the assembly of the sensor to the facility, since it is available on many places.



**Figure 16 – 3/4” (19 mm) Yee union.**

With this union, the sensor’s stainless steel tube has to be bent only 45 degrees (Fig. 17), which can be easily done without breaking or getting deformed after the springback. Then, the union gets soldered at each side to adapt it to the facility and, for the most important part, a 1/2” (12.7 mm) tube gland is implemented, so the sensor remains dry on the inside and the flow does not escape. Other adaptations had to be made since ideal unions were not available in the area.



**Figure 17 – Stainless-steel tube bent at 45 degrees.**



As it can be seen on Fig. 18 on the down-rightmost side, a cap is soldered to a soldable M union and drilled for a 1/4" (6.3 mm) tube, which passes through it and is soldered too. This tube has a 1/2" (12.7 mm) Flare conector, which connects to a 1/2" M Flare-F BSPT union that then connects to the tube gland. There is some length left for the sensor to be attached to the tube gland while the sensor is already inside the Yee union (Fig. 19).

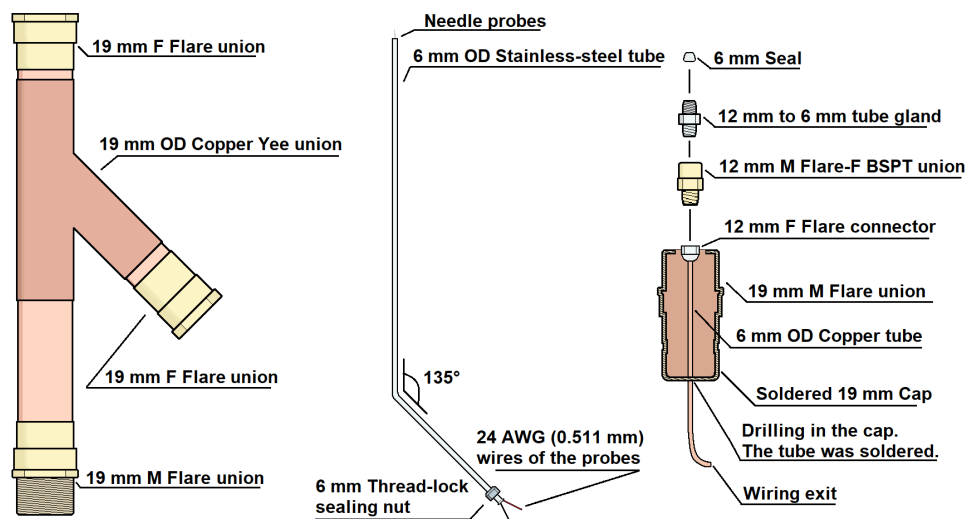


Figure 18 – Impedance sensor assembly parts.



Figure 19 – Assembled impedance sensor example.

This is how the sensor is assembled to be adapted to the facility. Now, about the construction of the sensor, it all begins with the soldering of the needles to the wires (Fig. 20). In this case, the needles are soldered to the 24 AWG wires by using tin with a 5 percent of silver, utilizing propylene to melt the soldering first and then using it to quickly solder the tiny union.

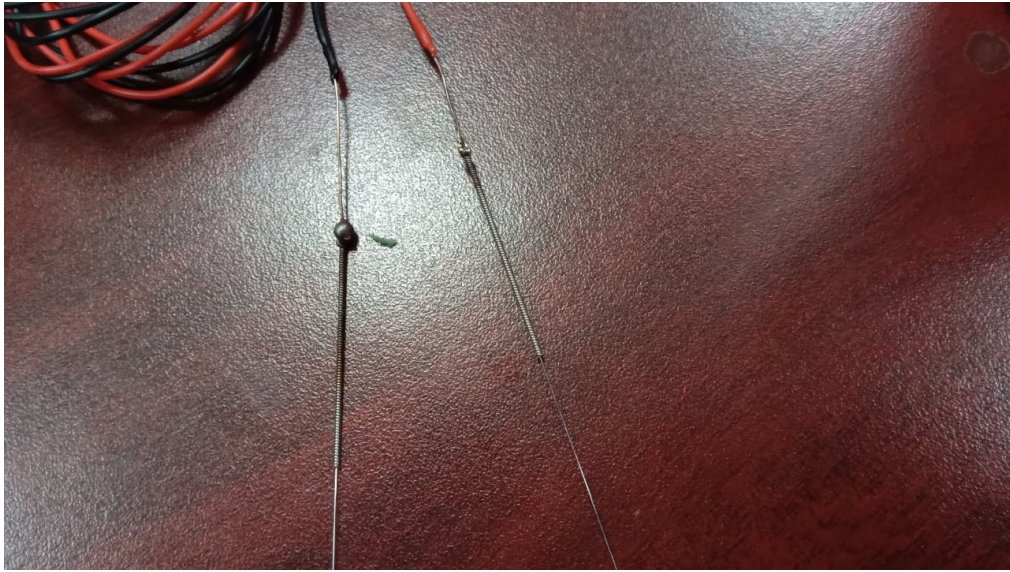


Figure 20 – Soldered needles.

The next step is the coating of the needles (Fig. 21), which are dipped into the coating and pulled out slowly, so the liquid distributes smoothly and drops are not left. Due to the surface tension effects, the tips of the needles will never get coated. Then, once the needles are completely coated and dry, they get inside the tube and positioned with the aid of an optical comparator. Doing this, the distance between the tips and the needles are assured, so they get fixed in position utilizing epoxy resin (Fig. 22).



**Figure 21 – Coated needles.**



**Figure 22 – Epoxy on the impedance needle-probe sensor.**

Of course, there are some things that have to be avoided, since this sensor is weak to mechanical forces as bending and filtering are its weak points. At least for this setup, the outlet of the wires from the steel rod had to also be covered in epoxy, since some water would filter at high pressures. Having water inside the rod affects

the measuring of the needles as they detect the signal with higher impedance due to the water.

In regard of the bending, the sensor has to go through inside the copper tubes, so bumping with an union very likely to happen. That said, it needs to be slowly and carefully driven. After that, the signal must be tested both in full air, full water and mixture conditions to verify if it is working, since sometimes the bent part may not be visible (Fig. 23) and thus the sensor's needles have to be replaced.



**Figure 23 – Tip of the needle bent. The size of the bent was about 0.2 mm and it already affected the measurements.**

### 3.6 ACQUISITION OF THE SIGNALS

A direct measurement can be made, since it is just a vector resulting from the influence of reactance over resistance, and the impedance will change depending

on the input and output voltage due to the phase shift. Thus it can be found that impedance can be measured as:

$$Z = \left( \frac{V_{in}}{V_{in} - V_{out}} \right) R \quad (3.2)$$

Despite this looking easy, the resistance ( $R$ ) has to be precisely known and quite small to achieve better measurements. That said, in order to measure the signals of each sensor, an electronic circuit is needed to obtain a voltage output for the data acquisition (DAQ) system. There are many methods to sense these and it is necessary to check all of them, since some methods are better than others depending on the sensor type and some of them are easier or harder to develop. There are many circuits for this purpose, but we will mention only some categories.

### 3.6.1 BRIDGE CIRCUIT

These kind of circuits are widely used for impedance measurements in electronics. These are low-cost and quite easy to arrange. Its simplified configuration can be seen on [Fig. 24](#).

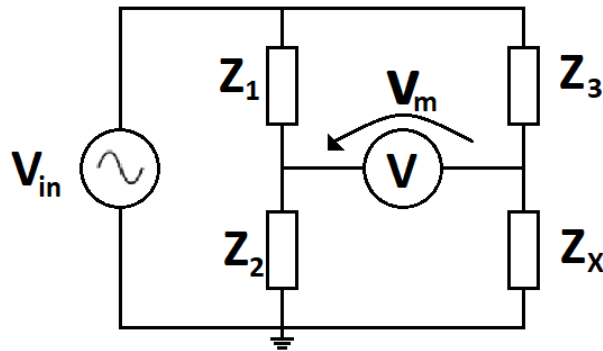


Figure 24 – General bridge circuit configuration.

The working principle of the circuit is based on the assumption that if the bridge is balanced, the relation between impedances  $Z_1$  and  $Z_2$  are equal to the

relation between  $Z_3$  and  $Z_x$ . That is, when the voltage  $V_m$  is 0, the following condition holds:

$$\frac{Z_1}{Z_2} = \frac{Z_3}{Z_x} \quad (3.3)$$

Some examples of bridges are the renowned Wheatstone and Wien bridges. These are used for knowing the resistance of a component and the frequency of a circuit respectively. However, the Wheatstone bridge is usually employed with DC current and Wien bridge may be difficult to manage since frequency loss is only discernible at high-frequency sensitive reactive circuits. Other bridges are the Maxwell, Hay and Schering bridges, which work on AC current and are utilized for impedance measurement.

The utility of these bridges come out when a balanced bridge obtained for, let us say, full liquid phase and when it starts to change its void fraction, the balance breaks down and a voltage raises in  $V_m$ . This allows to know the void fraction knowing that the value of  $V_{liq}$  is 0 and the value of  $V_{gas}$  is the maximum voltage.

### 3.6.2 RLC CIRCUITS

Resonance is another method which comes from RLC circuits to determine impedance. We have previously said that frequency loss is only discernible at high-frequency sensitive reactive circuits, that is why resonance frequency comes into play. An RLC circuit where its input current is at the same frequency as the resonance frequency of the LC part lets the impedance be its maximum value and, consequently, make the reactances cancel each other. Thus, whenever the impedance value changes due to the flow, the voltage will drop from its maximum value. Though, it is needed to know at least one the exact value of the resistance and of either the inductance or the capacitance.

### 3.6.3 COMPARATOR CIRCUITS

If varying values to get a balance state is a hard and long task, application of operational amplifiers (op-amp) to make comparator circuits might be another option. The usage of an op-amp with a high-input and low-output resistance can better the measurement of a direct and single input. This type of circuit is known as auto-balance bridge (though it differs from a bridge circuit configuration) and it is typical for many types of impedance measuring circuits. It presents high signal-to-noise ratio and stray-capacitance immunity (which is the tiny capacitance that merges from the grounding of the tube) and its output voltage depends only on the impedances of the circuit (Fig. 25). It may be difficult to understand how it works at first sight, however, the output voltage, when op-amp conditions are met ( $I_{op-amp} = \infty$  and  $V_{op-amp} = \infty$ ), is simply the gain made by the impedances times the input voltage as it is shown in the following equation:

$$V_{out} = -V_{in} \frac{Z_f}{Z_x} \quad (3.4)$$

Where the output signal will be delayed  $180^\circ$  as the op-amp works as an inverting op-amp. Some may wonder what is the point of this circuit if the signal is only getting a gain. The reason behind this is that this arrangement makes the output signal dependant only on a gain and the phase shift will not be present. Thus, if we consider a gain of 1, no matter what values the impedances have, the output voltage will be the same as the input but inverted.

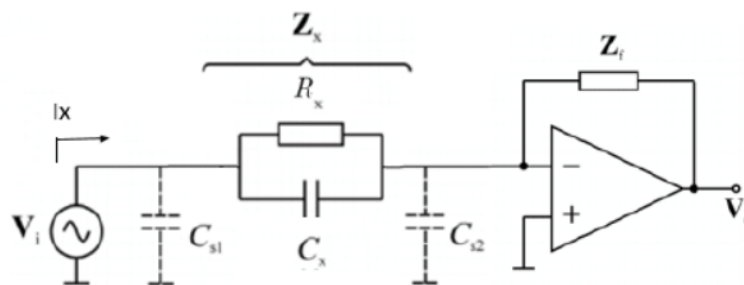


Figure 25 – Auto-balance bridge circuit configuration.

There are other ways to use the op-amps. For instance, differential amplifiers could be employed for fast-flow measurements.

### 3.6.4 THE DESIGNED CIRCUITS

In this work, an impedance and a capacitance sensors are developed, so the circuit used for each sensor may not be the same.

#### **Capacitance sensor circuit**

For example, since measured capacitances are small, an amplification circuit is usually recommended. [Chakraborty & Prasanta \[16\]](#) made an amplification circuit that was as well a bridge-differential circuit for more precision in an impedance probe sensor, making use of a Wien bridge oscillator in order to reach high frequencies, and a Wheatstone bridge to measure the difference of the signals through a comparison with a differential op-amp whenever the probes impedance changed. However, we chose for the capacitance measurement to make use of the Schering bridge circuit, since this one has not been used for void fraction measurement purposes and it can be employed for measuring the capacitance of the flow at zero and maximum voltage.

The Schering circuit consists of an AC bridge having four arms ([Fig. 26](#)), where one arm consists of a single resistor, one arm consists of a parallel combination of a resistor and a capacitor, another arm consists of a single capacitor and the measuring arm consists of a series combination of a resistor and a capacitor.



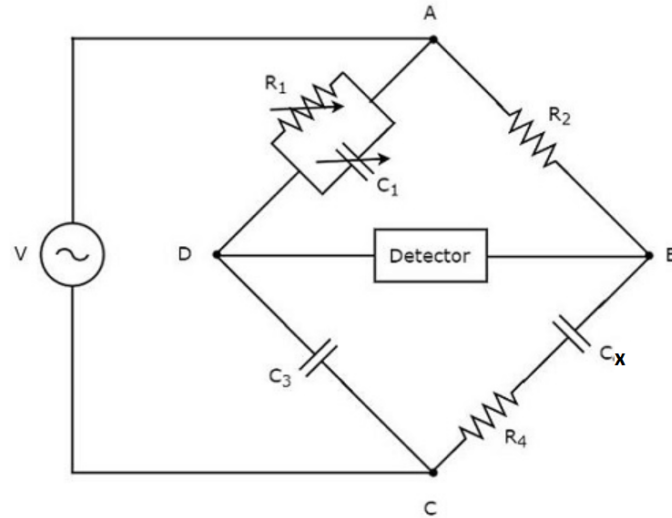


Figure 26 – Schering bridge circuit configuration.

The value of impedances will be as follows.

For  $Z_1$ :

$$Z_1 = \frac{R_1 X_1}{R_1 + X_1} = \frac{R_1 \left( \frac{1}{j\omega C_1} \right)}{R_1 + \left( \frac{1}{j\omega C_1} \right)} \quad (3.5)$$

$$Z_1 = \frac{R_1}{1 + j\omega R_1 C_1} \quad (3.6)$$

For  $Z_2$ :

$$Z_2 = R_2 \quad (3.7)$$

For  $Z_3$ :

$$Z_3 = X_3 = \frac{1}{j\omega C_3} \quad (3.8)$$

For  $Z_4$ :

$$Z_4 = R_4 + X_x = R_4 + \frac{1}{j\omega C_x} \quad (3.9)$$

$$Z_4 = \frac{1 + j\omega R_4 C_x}{j\omega C_x} \quad (3.10)$$

Utilizing Eq. (3.2), we have that the value of  $Z_4$  would be:

$$Z_4 = \frac{Z_2 Z_3}{Z_1} \quad (3.11)$$

Replacing the values of the impedances  $Z_1$ ,  $Z_2$ ,  $Z_3$  and  $Z_4$  for Eqs. (3.6), (3.7), (3.8) and (3.10) respectively,

$$\frac{1 + j\omega R_4 C_x}{j\omega C_x} = \frac{R_2 \left( \frac{1}{j\omega C_3} \right)}{\left( \frac{R_1}{1 + j\omega R_1 C_1} \right)} \quad (3.12)$$

$$\frac{1 + j\omega R_4 C_x}{j\omega C_x} = \frac{R_2 (1 + j\omega R_1 C_1)}{j\omega R_1 C_3} \quad (3.13)$$

And finally rearranging for  $C_x$  and  $R_4$ ,

$$\frac{1}{C_x} + j\omega R_4 = \frac{R_2}{R_1 C_3} + \frac{j\omega C_1 R_2}{C_3} \quad (3.14)$$

Thus we have the respective values of the real and imaginary terms of the above equation that can be compared and described as follows:

$$C_x = \frac{R_1 C_3}{R_2} \quad (3.15)$$

$$R_4 = \frac{C_1 R_2}{C_3} \quad (3.16)$$

Since impedance of the tube utilized for the capacitive sensor is highly capacitive,  $C_x$  is the only variable term. That said, the circuit has to be highly capacitive and it needs an high-frequency input.

### Impedance needle-probe sensor circuit

For the impedance probe sensor, on the other hand, the selected circuit is based on that from Mendez et. al. [17]. This simple but effective circuit (Fig. 27), which consists of a resistor ( $R = 100 \text{ k}\Omega$ ), a potentiometer ( $R_V = 0 - 100 \text{ k}\Omega$ ) and an impedance which is highly resistive ( $R_m$ ), making it an easy way to measure the

voltage drawn from the needle  $R_m$ . The resistor limits the current that flows through the circuit as its input voltage is fixed. The utility of the potentiometer comes when adjusting the signal voltage value that goes into the needle.

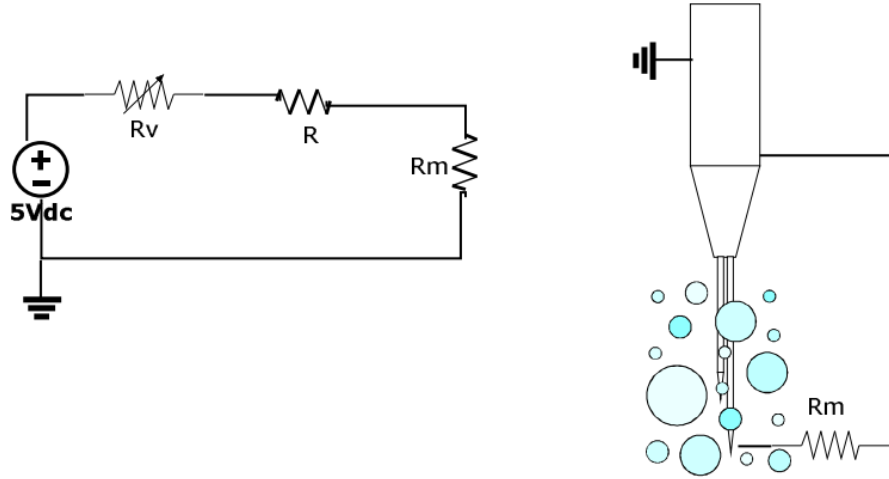


Figure 27 – Single-probe circuit configuration [17].

It is important to denote that  $R_m$  is a series resistance in the circuit generated from the resistance due to flow and that is present in the uncoated needle tip, which changes depending on the resistance of the medium passing through the needle. Thus the voltage in  $R_m$  will be highly influenced by the flow, since water and air resistance have a huge difference of approximately 500 times ([17]). The resistance  $R_m$  also limits the current, as it can be seen on the next demonstration:

$$V_T = V_R + V_{R_V} + V_{R_m} = (R + R_V + R_m)I \quad (3.17)$$

$$R_m = \frac{V_T}{I} - (R + R_V) \quad (3.18)$$

This way, whenever  $R_m$  changes, so will the current across the circuit and the voltage in  $R_m$  will also change.

### 3.7 NOMENCLATURE

C	Capacitance, [F]
R	Electrical resistance, [ $\Omega$ ]
V	Voltage, [V]
X	Electrical reactance, [ $\Omega$ ]
Z	Electrical impedance, [ $\Omega$ ]

*Greek letters*

$\omega$	Angular frequency of excitation, [rad/s]
----------	---

*Subscript*

f	Flow
W	Tube section wall

### 3.8 REFERENCES

- [3] Portillo, Guillermo; Shedd, Timothy A.; and Lehrer, Kathryn H., "Void Fraction Measurement in Minichannels with In-Situ Calibration" (2008). International Refrigeration and Air Conditioning Conference. Paper 887. <http://docs.lib.purdue.edu/iracc/887> <sup>a</sup>
- [14] Qian, H., & Hrnjak, P. (2020). Mass measurement based calibration of a capacitive sensor to measure void fraction for R134a in smooth tubes. *International Journal of Refrigeration*, 110, 168–177. <https://doi.org/10.1016/j.ijrefrig.2019.10.019> <sup>a</sup>
- [16] Chakraborty, S., & Das, P. K. (2020). Characterisation and classification of gas-liquid two-phase flow using conductivity probe and multiple optical sensors. *International Journal of Multiphase Flow*, 124, 103193. <https://doi.org/10.1016/j.ijmultiphaseflow.2019.103193> <sup>a</sup>
- [17] Méndez, S. (2008) *Medida experimental de la concentración de área interfacial en flujos bifásicos finamente dispersos y en transición* [Doctor's degree thesis, Universitat Politècnica de València] Repositorio Institucional de la Universitat Politècnica de València. <https://riunet.upv.es/bitstream/handle/10251/3301/tesisUPV2899.pdf>  
<sup>a b c</sup>
- [19] Silva-Alvarado, O., Villanueva-Garza, C. I., Morales-Fuente, A., Sánchez-Cruz, F. A., Martínez-Martínez, S., Méndez-Díaz, S. (2022). Zeotropic refrigerants: Image analysis for void fraction measurement at evaporator's inlet for R-404A. XXVIII Congreso Internacional Anual de la SOMIM - Termofluidos. (n.d.). T 161– T 167. <https://somim.org.mx/memorias/memorias2022/articulos/A4.107.pdf> <sup>a</sup>
- [20] Rouhani, Z., 1969, AB Atomenergi, Sweden, International Report, AE-RTV 841. <sup>a</sup>
- [21] Canière, H., T'Joel, C., Willockx, A., Paeppe, M. D., Christians, M., Rooyen, E. V., Liebenberg, L., & Meyer, J. P. (2007). Horizontal two-phase flow characteriza-

tion for small diameter tubes with a capacitance sensor. *Measurement Science and Technology*, 18(9), 2898–2906. <https://doi.org/10.1088/0957-0233/18/9/020> <sup>a b c</sup>

[22] ROGERS CORPORATION. CLTE-MWTM Laminates<sup>TM</sup>. (s. f.). <https://www.rogerscorp.com/advanced-electronics-solutions/clte-series-laminates/clte-mw-laminates> <sup>a</sup>

[23] Chattopadhyay, S. (2022). Is CPVC Pipe Fire Rated? What to Look For When Choosing Fire Protection Materials. [www.blazemaster.com](http://www.blazemaster.com). [https://www.blazemaster.com/blog-in/is-cpvc-pipe-fire-rated-what-to-look-for-when-choosing-fire-protection-materials#:~:text=CPVC%20has%20an%20extremely%20high,500%C2%B0F\)%20or%20lower](https://www.blazemaster.com/blog-in/is-cpvc-pipe-fire-rated-what-to-look-for-when-choosing-fire-protection-materials#:~:text=CPVC%20has%20an%20extremely%20high,500%C2%B0F)%20or%20lower) <sup>a</sup>

[24] Liu, Y., Yang, X., Zhu, Q., Ju, P., Ishii, M., & Buchanan, J. (2017). Development of the droplet-capable conductivity probe for measurement of liquid-dispersed two-phase flow. *International Journal of Multiphase Flow*, 88, 238–250. <https://doi.org/10.1016/j.ijmultiphaseflow.2016.06.012> <sup>a</sup>

[25] Shen, X., & Nakamura, H. (2013). Local interfacial velocity measurement method using a four-sensor probe. *International Journal of Heat and Mass Transfer*, 67, 843–852. <https://doi.org/10.1016/j.ijheatmasstransfer.2013.08.064> <sup>a</sup>

[26] Euh, D., Yun, B., Song, C., Kwon, T., Chung, M., & Lee, U. (2001). Development of the five-sensor conductivity probe method for the measurement of the interfacial area concentration. *Nuclear Engineering and Design*, 205(1–2), 35–51. [https://doi.org/10.1016/s0029-5493\(00\)00376-9](https://doi.org/10.1016/s0029-5493(00)00376-9) <sup>a</sup>

[27] Hosokawa, S., Hayashi, K., & Tomiyama, A. (2013). Void distribution and bubble motion in bubbly flows in a 4×4 rod bundle. Part I: Experiments. *Journal of Nuclear Science and Technology*, 51(2), 220–230. <https://doi.org/10.1080/00223131.2013.862189> <sup>a</sup>

[28] Ren, Q. Y., Pan, L. M., Pu, Z., Zhu, F., & He, H. (2021). Two-group phase distribution characteristics for air-water flow in 5 × 5 vertical rod bundle channel

with mixing vane spacer grids. *International Journal of Heat and Mass Transfer*, 176, 121444. <https://doi.org/10.1016/j.ijheatmasstransfer.2021.121444> <sup>a</sup>

[29] Shen, X., Mishima, K., & Nakamura, H. (2008). Error reduction, evaluation and correction for the intrusive optical four-sensor probe measurement in multi-dimensional two-phase flow. *International Journal of Heat and Mass Transfer*, 51(3–4), 882–895. <https://doi.org/10.1016/j.ijheatmasstransfer.2006.01.054> <sup>a</sup>

[30] Wang, D., Fu, Y., Liu, Y., Talley, J. D., Worosz, T., Hogan, K., & Buchanan, J. R. (2021). A comprehensive uncertainty evaluation of double-sensor conductivity probe. *Progress in Nuclear Energy*, 136, 103741. <https://doi.org/10.1016/j.pnucene.2021.103741> <sup>a</sup>

[31] Satou, A., Sagawa, J., Sun, H., Sibamoto, Y., & Yonomoto, T. (2021). Error in bubble velocity measurement using 4-sensor void probe due to interface deformation. *Nuclear Engineering and Design*, 379, 111234. <https://doi.org/10.1016/j.nucengdes.2021.111234> <sup>a</sup>

[32] Heringe, R., & Davis, M. R. (1976). Structural development of gas-liquid mixture flows. *Journal of Fluid Mechanics*, 73(1), 97–123. <https://doi.org/10.1017/s0022112076001274> <sup>a</sup>

[33] Wu, Q., & Ishii, M. (1999). Sensitivity study on double-sensor conductivity probe for the measurement of interfacial area concentration in bubbly flow. *International Journal of Multiphase Flow*, 25(1), 155–173. [https://doi.org/10.1016/s0301-9322\(98\)00037-8](https://doi.org/10.1016/s0301-9322(98)00037-8) <sup>a</sup>

[34] Revankar, S. T., & Ishii, M. (1992). Local interfacial area measurement in bubbly flow. *International Journal of Heat and Mass Transfer*, 35(4), 913–925. [https://doi.org/10.1016/0017-9310\(92\)90257-s](https://doi.org/10.1016/0017-9310(92)90257-s) <sup>a</sup>

# EXPERIMENTAL CAMPAIGN

---

## 4.1 CALIBRATION PROCEDURE

It is important to know the total volume inside the facility as it provides advantage on quality and void fraction measurements for the sensors' calibration. There are two ways to determine this: theoretical and experimental. The first one relies on the calculation of the inner volume with the dimension measurements and items like a pump. However, since it is not quite accurate, as there are couplings and connectors that can change all of this after soldering and attaching, the second method is the most suitable, as it consists of filling up all the facility with water and measuring the used volume.

Tests at different flow rates for water and air are managed. The first one has to be at full liquid, making the measured void fraction equal to 0 and the capacitance or impedance, depending on the sensors, equal to  $C_l$  and  $Z_l$  respectively. Then, measurements will be running for 90 seconds per test and measured void fraction, capacitance and impedance will be averaged in time. In every test the void fraction will be augmented until it reaches the value of 1, which means a full-air flow. This will result on getting a capacitance and impedance value of  $C_g$  and  $Z_g$  respectively.

At every measurement a normalized value is calculated utilizing the full-liquid



and full-gas values as follows:

$$C_{norm} = \frac{C_l - C_{measured}}{C_l - C_g} \quad (4.1)$$

$$Z_{norm} = \frac{Z_l - Z_{measured}}{Z_l - Z_g} \quad (4.2)$$

It can be seen that in all the cases the normalized value equation behaves similar and can be applied to using the measured voltage instead too. Still, quality of the measurements depend on the sensors capacity and calibration accuracy. Then, for the final step, normalized data points are plotted versus void fraction data points, resulting on the creation of a curve that could fit to the data. This could lead to an error adjustment on the sensing for every run until the result is satisfactory.

Another calibration procedure followed is utilizing pressure rates differences at the beginning and ending of the testing section, that is, immediately after the mixing section and the to-be-calibrated sensor section. This is made knowing the difference on values between the upper and bottom sensors due to the column of pressure between them. As air starts to be pumped and mixed, the flow will decrease its pressure, giving us the information we need to calculate the void fraction of that section, as it can be seen as follows:

$$V_{norm} = \frac{V_l - V_{measured}}{V_l - V_g} \quad (4.3)$$

We can also have another way to know and calibrate the void fraction and relate it with flow regimes through the usage of phase velocities, as we measure individually water and air fluxes.

A detailed diagram of these measuring instruments can be seen on [Fig. 28](#). The facility ([Fig. 29](#) and [Fig. 30](#)) has the DAQ away from the test facility for security purposes of the electronics. It can be seen that the image acquisition section had been hidden from external light with a plywood box, so the only lights that enters

comes from a hole at the other side of the hole made for the camera, giving a better image to analyze.

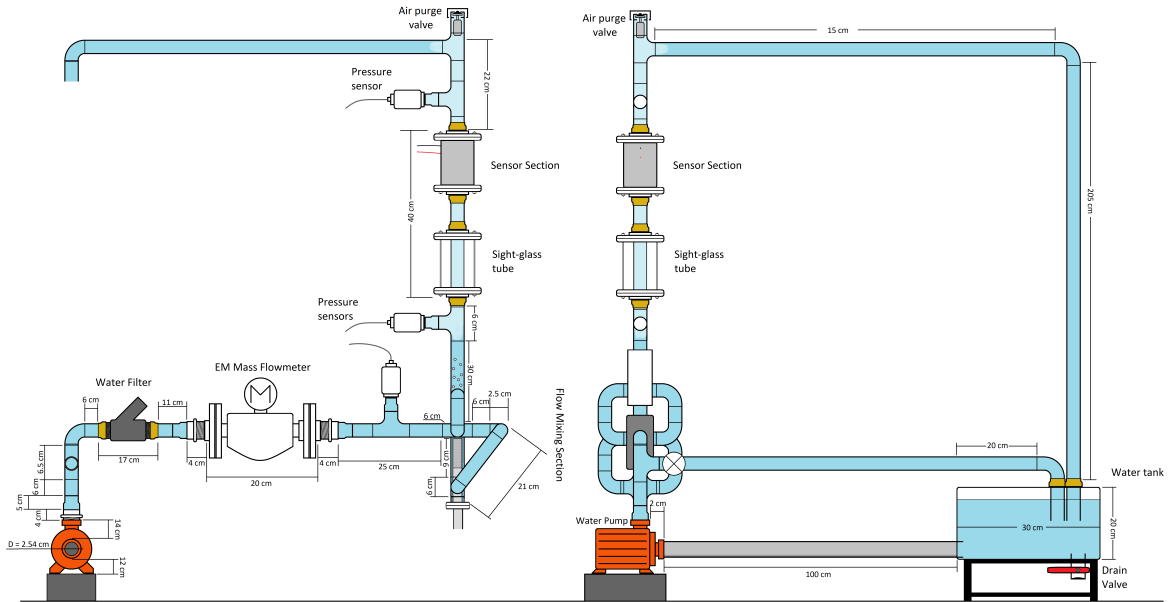


Figure 28 – Calibration facility sensors diagram.

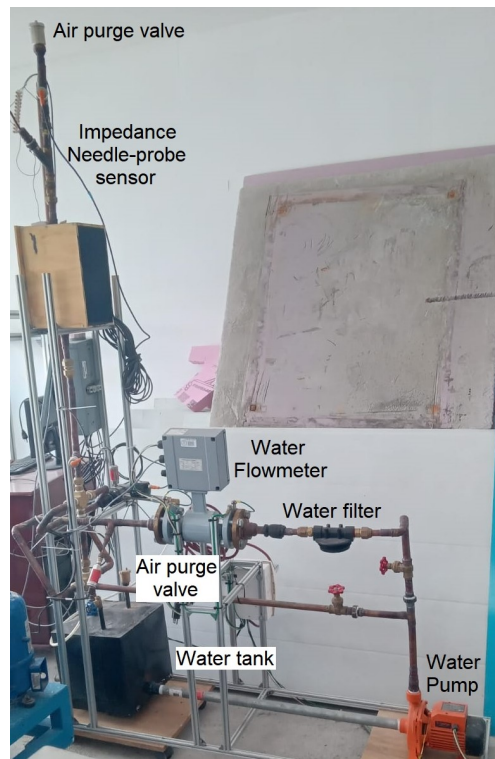


Figure 29 – Calibration facility (Side view).

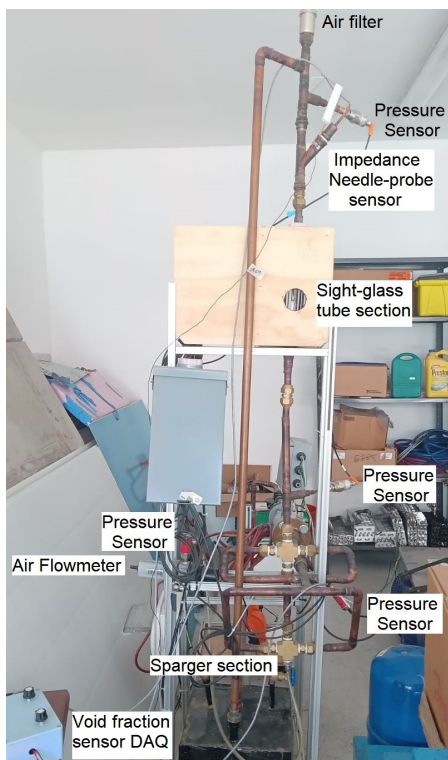


Figure 30 – Calibration facility (Front view).

Tests were runned for different water flow rates at a fixed inlet air flow rate, taking care of getting different bubble sizes and flow regimes.

## 4.2 CAPTURED IMAGES ANALYSIS

The images acquired by the Phantom V9.1 camera are analyzed utilizing the development platform LabVIEW with package tools such as toolkits NI-IMAQdx, NI-IMAQ, Vision Builder, and Vision Development Module, among others. Consecutive images were acquired at a speed of 900 fps for the first test and 1,200 fps for the second and third tests.

The image analysis of each frame let us obtain the void fraction, as well as it let us identify the flow regime map and measure the superficial gas velocity. For this purpose, the flow is firstly captured in two cases: 1) at full liquid flow and 2) at a fully developed flow. This way, the flow can be analyzed by a position correlation in LabVIEW.

### 4.2.1 IMAGE ANALYSIS VOID FRACTION

The acquisition camera [Fig. 31](#) saves the capture in an Audio Video Interleave (AVI) file. The built app detaches each frame from the video, isolates the region of interest (ROI) and binarizes it, discriminating the liquid phase from the gaseous phase. The available area for the analysis measures the occupied surface by the gaseous phase through an image histogram analysis. The void fraction is calculated then as the rate between the occupied surface by the gas and the total surface. [Fig. 32](#) shows the ROI where a mask is applied to isolate the information of interest that contains the refrigerant flow.



Figure 31 – Phantom high-speed camera utilized for image acquisition.

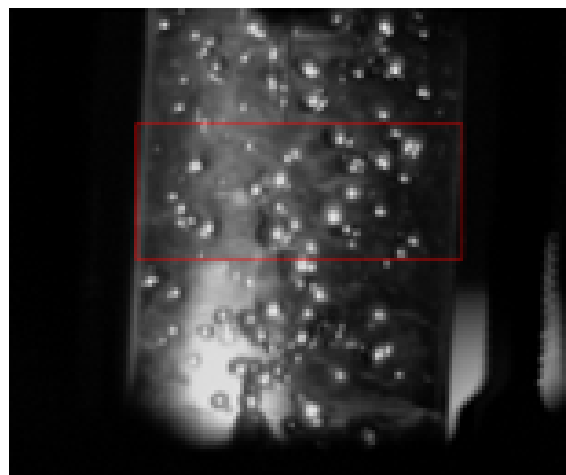


Figure 32 – Region of interest of the flow inside the sight-glass. The region limits only the vertical flow and it is delimited by the red rectangle.

In the ROI, the threshold algorithm, which binarizes the frames, is applied, discriminating the liquid from the gas by indicating that 1 is “liquid” and 0 is “gas”, Fig. 33a. Afterwards, the histogram (Fig. 33b) of each line of the frame is made and the pixels that represent the gaseous phase are added. The result provides the total occupation of the gas in the radial direction. Therewith, the area fraction that occupies the gas is acquired.

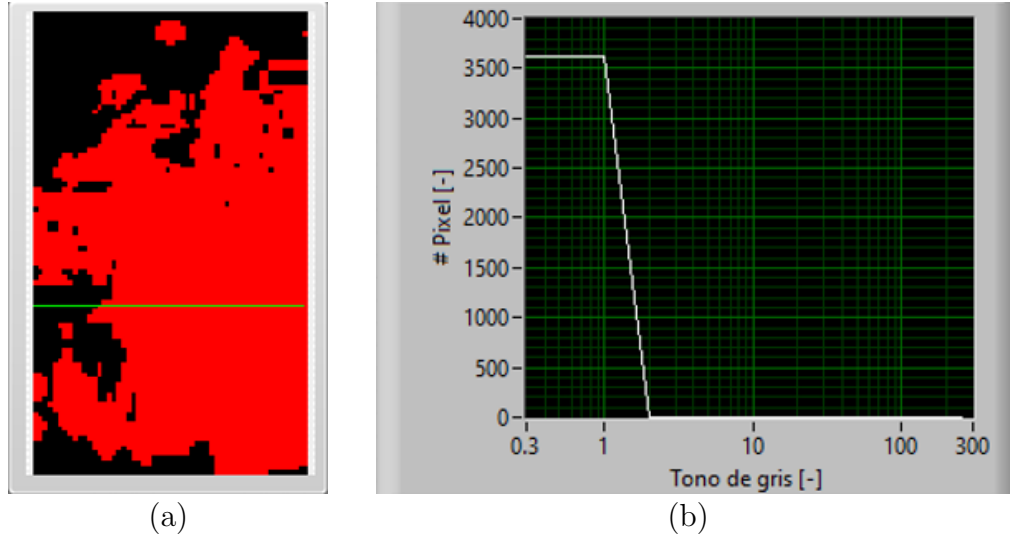


Figure 33 – (a) Binarized image. The 1 (black) indicate liquid presence and the 0 (red) indicate gas presence. (b) Binarized image histogram of a line.

The time-averaged void fraction,  $FV'$ , is obtained by the amount of void fraction of each frame,  $\langle FV \rangle$ , divided by the total captured frames in the video,  $N$ .

$$FV' = \frac{\sum \langle FV_i \rangle}{N} \quad (4.4)$$

The void fraction of each frame,  $\langle FV_i \rangle$ , is calculated using the void fraction in the radial direction, that is, the average of the proportion of pixels of value different from 1 (liquid) in relation to the total of pixel columns ( $n$ ) in the ROI, of size  $m \times n$ , row  $x$  column.

$$\langle FV_i \rangle = \frac{\sum \left(1 - \frac{Pix_i}{n}\right)}{m} \quad (4.5)$$

The code (Fig. 34) basically opens each image and its consecutive frame image. Afterwards, the images are converted from its RGB U8 (Red, Green and Blue color

scaled image) format to a 8-bit monochromatic format in grayscale, in which every pixel intensity's value range from 0 to 256. The ROI is selected (Fig. 35) and it is the same for every frame of a complete sequence. After that, the portion defined as the ROI is extracted. Thus, the image is binaryzed utilizing the threshold tool, which establishes a limit that, for those pixels that are under an intensity of 128, assign a value of 0 (black color) and, for those that exceed the value of 128, are assigned to a value of 1 (white color). In this way, every particle, bubble or gas volume is managed to be separated from the rest of the image.

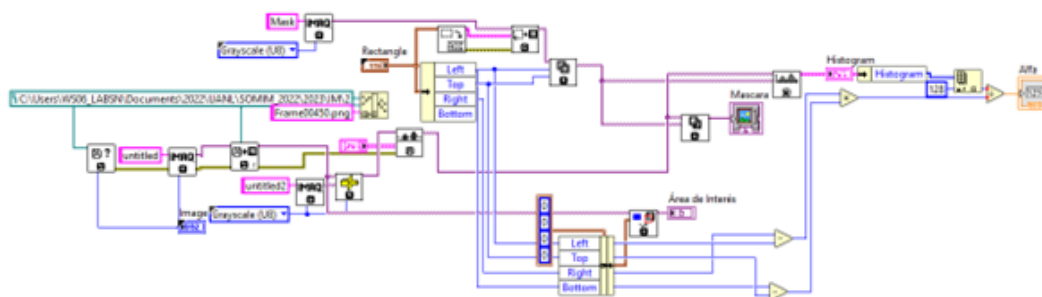


Figure 34 – Code utilized to calculate the mean void fraction.

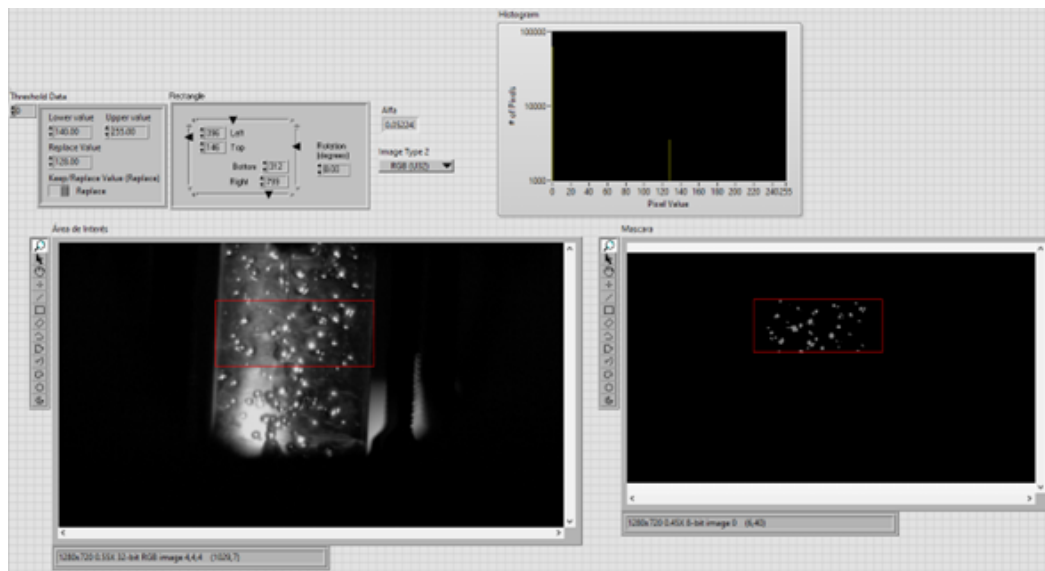


Figure 35 – Code screen run of the frames processed to calculate the mean void fraction.

Then, throughout the usage of a histogram, pixels of 128 scaling are counted and divided in respect to the rest of the ROI pixels. After that, the portion occupied by the gas in the frame is ponderated.

Subsequently, the same algorithm is applied to the complete images sequence and the mean void fraction is calculated from there with the method described previously.

#### 4.2.2 IMAGE ANALYSIS SUPERFICIAL GAS VELOCITY

To obtain the superficial gas velocity, each image and its consecutive frame image are opened in the code (Fig. 36). Afterwards, the images are converted from its RGB U8 (Red, Green and Blue color scaled image) format to a 8-bit monochromatic format in grayscale, in which every pixel intensity's value range from 0 to 256. The ROI is selected (Fig. 37) and it is the same for every frame of a complete sequence. After that, the portion defined as the ROI is extracted. Thus, the image is binaryzed utilizing the threshold tool, which establishes a limit that, for those pixels that are under an intensity of 128, assign a value of 0 (black color) and, for those that exceed the value of 128, are assigned to a value of 1 (white color). In this way, every particle, bubble or gas volume is managed to be separated from the rest of the image.

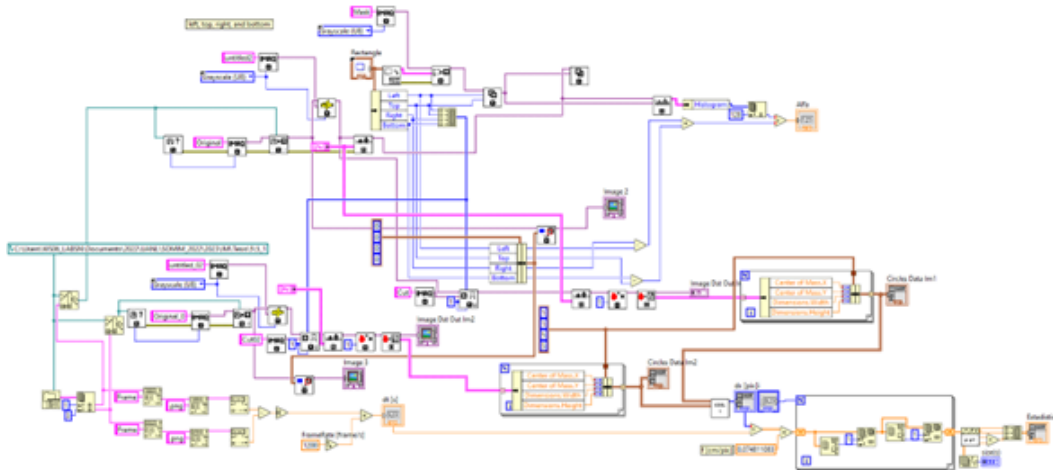
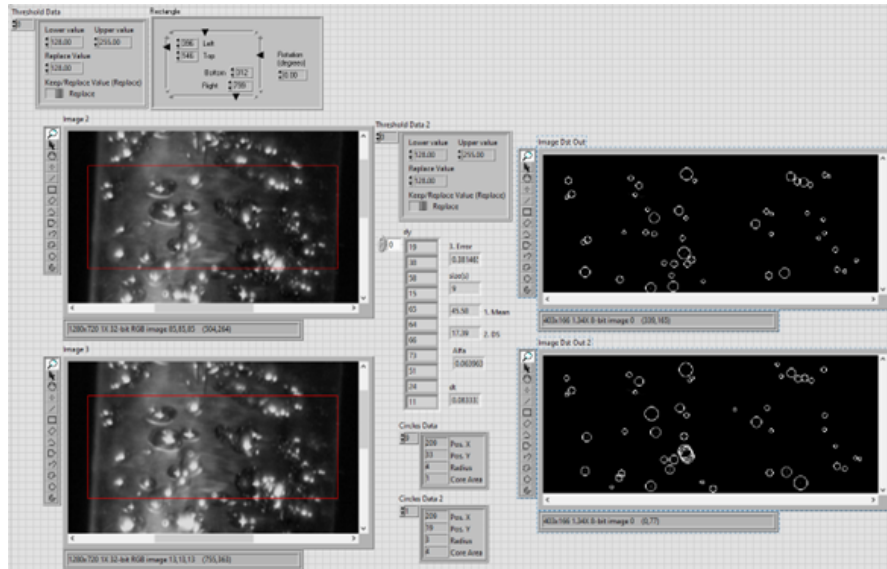


Figure 36 – Code utilized to calculate the mean superficial gas velocity.



**Figure 37** – Code screen run of the frames processed to calculate the superficial gas velocity.

After all of that, every particle on each ROI is counted; each of those particles has their centre of inertia and equivalent diameter calculated. From the acquired data of the first frame a 2-D ROI is made, and for the next frame, on the same ROI, the particle with the most similar diameter is identified. Thus, the movement of the centre of inertia is calculated.

Each frame is already saved with a sequential number name. The sequential numbers indicate implicitly the time at which they were acquired. This means that the difference between the sequential numbers times the sample rate equals to the time between each taken frame. Throughout a pixel/milimeter calibration process, the image is adjusted and the velocity is obtained via the movement of the bubble over the time between frames.

The algorithm is applied to the all detected particles. Thus, the mean superficial gas velocity is obtained as well as other statistical parameters. Afterwards, the code is applied for the complete sequence and a total mean superficial gas velocity is acquired.



## 4.3 FLOW REGIME IDENTIFICATION

Depending on the sensing method, certain flow regimes can be identified, as the sensors' construction, location, geometry and/or method limit the capacity and accuracy for the flow regime identification.

Depending on the bubble sizes, void fraction and velocities, flow regimes can be identified. An efficient way to identify the regime is using statistical tools, since these attain characteristic signals associated with the passage of the dispersed phase over the probes field. These are quite a lot of statistical tools, as mentioned by [Simões-Moreira \[35\]](#), however, the most common to use is the Probability Density Function (PDF).

### 4.3.1 THE PROBABILITY DENSITY FUNCTION (PDF)

The PDF is an amplitude histogram related to an specific value of a time series signal for a determined range of possible values. In other words, we use this function to transform a range of voltage of the signal analysis, which goes from 0 to  $V_{max}$ , into a range of how much a value of voltage from 0 to 1 (0 to 100 percentile) appears in the signal (probability).

Basically, the probability of X lying in an interval (a,b) is calculated. The PDF formula for a continuous X is:

$$P(a \leq X \leq b) = \int_a^b f(x)dx \quad (4.6)$$

For better resolutions, the PDF is based on the making of a histogram, which is the frequency of a value. This is made by finding the minimum data points (k) needed for the histogram, based on the number of data points (Eq. 4.8). The range has a minimum value for every interval or bin ( $k_i$ ), which is basically the inverse

of the minimum data points (Eq. 4.9). In this case, our range is the limits of void fraction (0 and 1).

$$k = \sqrt{\text{Number of Data Points}} \quad (4.7)$$

$$k_i = \frac{1}{\text{Number of Data Points}} \quad (4.8)$$

Afterwards, the next step is to calculate the void fraction for each data value (Eq. 4.10). With these values, a histogram is made drawing frequencies taken from each bin over the range (Eq. 4.11). As for the PDF, knowing the bin value is essential, as the PDF utilizes the middle value of the interval  $X$  ( $X_{mid}$ ). Then, the PDF function can be calculated as the frequency of a value over the number of data points and the value of an interval  $X$ .

$$\alpha_i = 1 - \frac{V_{max} - V_m}{V_{max} - V_{min}} \quad (4.9)$$

$$n = \sum_{i=1}^k m_i \quad (4.10)$$

Where  $m_i$  is the histogram data.

$$PDF, f(x) = \frac{\text{Frequency}}{(\text{Number of Data Points})k_i} \quad (4.11)$$

With this, peaks of PDF can appear in different quantities and lengths, where a sharp and high peak of low voltage would mean a bubbly flow due to being most of the time the pipeline occupied by liquid; for a slug flow, there are two high peaks encountered near the 0 and 1 PDF value, being the last one quite small compared to the first one, since in slug flow there is a presence of many small bubbles and a few big bubbles; for churn flow, due to its erratic nature, there is no peak at all. These assumptions and analysis will be used to identify the flow regime.

## 4.4 FLOW REGIME THEORETICAL DETERMINATION

By utilizing the image analysis, it can be determined the flow regime. This has to be supposed by observing the flow, but it can be obtained theoretically. Once the observed flow regime is determined, it is compared to the calculation of theoretical data through the following methods for calculating the flow regime in vertical flows.

### 4.4.1 3-D FLOW REGIME MAP

As mentioned before in section 1.5, this method consists of a 3D vertical flow regimes map (Fig. 38) that goes through three parameters that have to be calculated one by one, and it works for vertical flow regimes with an angle in the range of 45 to 90 degrees (Teresa Barrachina [8], Chung et al. [36]). The mixture velocity,  $v_m$ , determines the way the phases are distributed. The superheat gives the line in where flow regimes develop and, finally, the flow regime void fraction comparison enacts which flow regime the flow belongs to.

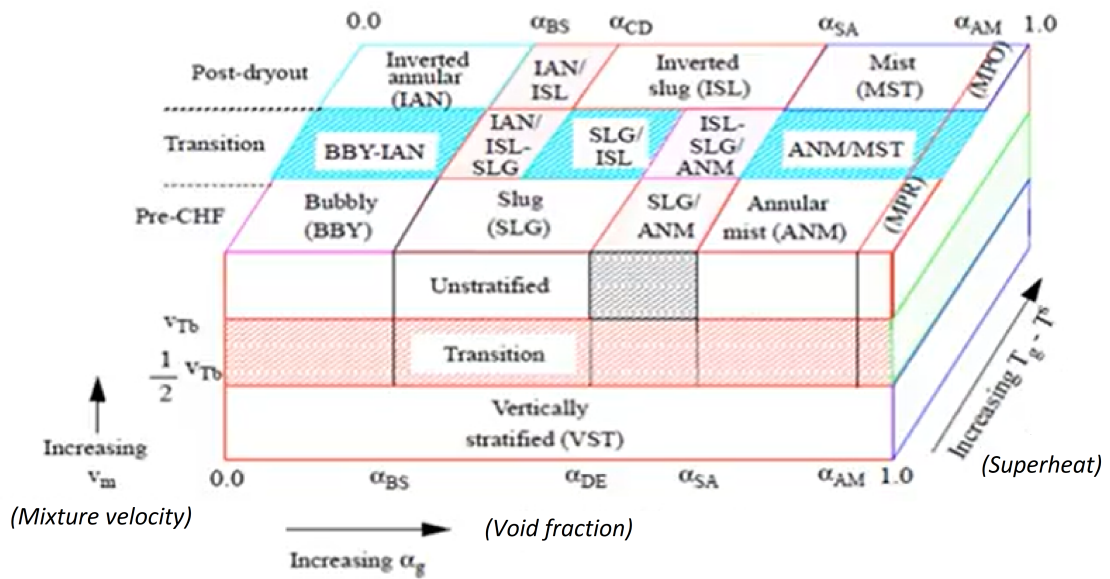


Figure 38 – 3-D vertical flow regime map. [8]

The method begins with the calculation of the mixture velocity,  $v_m$ , employing Eq. (4.12). That way it can be determined whether if the flow is stratified, unstratified or in transition between these. For this purpose, the transition criteria has to be calculated via Eq. (4.14), which is the Taylor-bubble transition velocity, and then compared with the mixture velocity.

$$v_m = \frac{G_m}{\rho_m} \quad (4.12)$$

Where  $G_m$  is the mixture mass flux and  $\rho_m$  is the mixture density whose value is:

$$\rho_m = \alpha_H \rho_g + (1 - \alpha_H) \rho_l \quad (4.13)$$

The Taylor-bubble transition velocity is then:

$$v_{Tb} = 0.35 D^* \left[ \frac{\sigma}{D \rho_l} \right]^{\frac{1}{2}} \quad (4.14)$$

Where  $D^*$  is the dimensionless tube diameter.

$$D^* = D \left[ \frac{g(\rho_l - \rho_g)}{\sigma} \right]^{\frac{1}{2}} \quad (4.15)$$

Thus, both velocities are compared. If  $v_m$  is equal or greater than  $v_{Tb}$ , then the flow is unstratified. However, if  $v_m$  is equal or greater than half the  $v_{Tb}$  and lower than  $v_m$ , the flow is considered in transition. Finally, if  $v_m$  is lower than half the  $v_{Tb}$ , the flow is stratified.

Now, superheat is defined as the difference between the gas temperature and the saturation temperature. If the superheat is 0 K, the flow is in the line of pre-Critical Heat Flux (CHF). Nonetheless, getting a value between 0 and 1 K leads to a flow in transition and, if it is greater than 1 K, the flow is in post-CHF. Knowing these conditions, it is very likely that the flow would be in the last region, since a superheat of less than 1 K is, in reality, a little difficult to obtain. Lastly, to know which flow regime our flow belongs to, void fraction for every flow regime is calculated. In other words, for every flow regime, there are some limits which have to be calculated and then compared to the required data. For this purpose,

transition criteria are explained in the next sections. It has to be remembered that the homogeneous void fraction determines the flow regime since it has to be between the limits imposed by the criteria.

### Bubbly – Slug transition criterion

This criterion is represented as  $\alpha_{BS}$  and it requires to have a mass flux which determines the condition the liquid void fraction,  $\alpha_l$ , has to accomplish.

$\alpha_l$  is defined as:

$$\alpha_l = 0.25 \min \left[ 1.0, \left( \frac{D^*}{22.22} \right)^8 \right] \quad (4.16)$$

If  $G_m$  is lower than 2000 kg/m<sup>2</sup>s:

$$\alpha_{BS} = \alpha_l \quad (4.17)$$

If  $G_m$  is between 2000 and 3000 kg/m<sup>2</sup>s:

$$\alpha_{BS} = \alpha_l + 0.001(0.5 - \alpha_l)(G_m - 2000) \quad (4.18)$$

If  $G_m$  is equal or greater than 3000 kg/m<sup>2</sup>s:

$$\alpha_{BS} = 0.5 \quad (4.19)$$

There is an exception where this state is theorized not to exist, however. As mentioned by [Chung et al. \[36\]](#), when the rise of velocity bubbles ( $v_{sb}$ ) in the bubbly flow regime exceeds  $v_{Tb}$ , the bubbles will approach the trailing edges of Taylor bubbles and coalesce. The equating of these two velocities yields to the critical pipe diameter ( $D_{crit}$ ). Below this diameter bubbly flow does not theoretically exist.

$$v_{sb} = 1.53 \left[ \frac{g(\rho_l - \rho_g)\sigma}{\rho_l^2} \right]^{\frac{1}{4}} \quad (4.20)$$

$$D_{crit} = 19.11 \left[ \frac{\sigma}{g(\rho_l - \rho_g)} \right]^{\frac{1}{2}} \quad (4.21)$$

### Slug – Slug/Annular – Mist transition criterion

This criterion is represented as  $\alpha_{DE}$  and it requires to have the void fraction of the previous criteria, as well as the Slug-Annular void fraction,  $\alpha_{SA}$ .

$$\alpha_{DE} = \max(\alpha_{BS}, \alpha_{SA} - 0.05) \quad (4.22)$$

$$\alpha_{SA} = \min(\alpha_{crit}^f, \alpha_{crit}^e) \quad (4.23)$$

Where  $\alpha_{crit}^f$  has two definitions. If the flow direction goes upwards, then:

$$\alpha_{crit}^f = \frac{1}{u_g} \left[ \frac{gD(\rho_l - \rho_g)}{\rho_g} \right]^{\frac{1}{2}} \quad (4.24)$$

If the flow direction is downwards or counterflow, then:

$$\alpha_{crit}^f = 0.75 \quad (4.25)$$

And finally,  $\alpha_{crit}^e$  is defined as:

$$\alpha_{crit}^e = \frac{3.2}{u_g} \left[ \frac{gD(\rho_l - \rho_g)}{\rho_g^2} \right]^{\frac{1}{4}} \quad (4.26)$$

### Slug/Annular Mist – Annular Mist transition criterion

This criterion, represented as  $\alpha_{SA}$ , is already defined in Eq. (4.23), since it is required to calculate the previous criteria and it is used in every line of the superheat region.

### Inverted Annular/Inverted Slug – Inverted Slug transition criterion

A special criterion that only happens to be in the post-CHF line region, albeit it is a very common region to land on. It is represented as  $\alpha_{CD}$ , and it belongs after the Bubbly-Slug transition criterion.

$$\alpha_{CD} = \alpha_{BS} + 0.2 \quad (4.27)$$

#### 4.4.2 AIR-WATER FLOW REGIME MAP COMPARISON

This method is a more simple and specific way to compare the results against data that already exists in literature. Air-water flow regimes have been studied since Taitel et al. [37], where they made a flow regime map for various regimes. However, Hibiki et al. [38] made a deeper research on this for a tube diameter of 50.8 mm and with the superficial liquid velocity and the void fraction, ranging from 0.491 to 5.00 m/s and from 0.049 to 0.442 respectively. They utilized the data from Taitel et al. and made a smoother chart which is shown in Fig. 39.

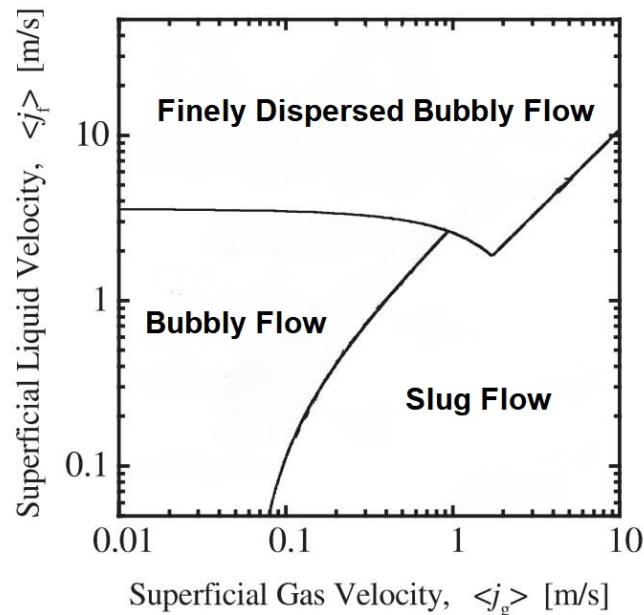


Figure 39 – Air-water vertical flow regime map drawn from [38].

### 4.5 THEORETICAL VOID FRACTION ANALYSIS

The correlations study for the determination of the void fraction is wide among many flow models that, on the knowledge of the author, are done with a water-air or water-steam flow. Many correlations were considered for the comparison and many of them come from the Homogeneous, Slip ratio and Drift Flux models. Some of these

correlations were derived from higher or lower tube diameters and flow rates; some of them were driven with water-air, water-steam or specific refrigerants. It is the result of using these correlations that it is important, however, it is also relevant to know the origin of these correlations, as it may or may not affect the result. Nevertheless, all the cases were considered. For this purpose, various correlations were gathered, which were obtained from the papers of [Xia et al. \[39\]](#), [Woldesemayat & Ghajar \[40\]](#) and [Gardenghi et al. \[1\]](#) and can be seen in [Table 1](#). In total, 31 correlations were used. A few of these, nonetheless, have more than one equation and, therefore, only the most likely cases of equations are shown, since it might get too long to fit in three pages and some cases are simply not related to these facilities (as in the correlation of [Hibiki & Ishii \[41\]](#)).

It is important to note that all of the Drift Flux model correlations are calculated with the [Eq. 1.10](#), except for those that have a specified void fraction correlation.

With the objective of evaluating the correlations, evaporator inlet temperature and pressure measurements are required to obtain properties such as the liquid and gas densities. Surface tension, liquid and gas dynamic viscosities as well. Furthermore, supposing an isenthalpic process, flow enthalpies for the mass quality calculus can be obtained.

These properties are utilized for most of the correlations, specifically, for the homogeneous and slip flow models. However, for the drift flux model, it is required to have at least the superficial gas velocity. Hence, the drift flux model correlations analysis is dependant on the gas-phase velocity.



Table 1 – Void fraction flow equations of the selected correlations. H = homogeneous, S = slip, D = drift flux. <sup>a</sup> Mentioned by Gardenghi et al. [1]; <sup>b</sup> mentioned by Xia et al. [39]; <sup>c</sup> mentioned by Woldesemayat & Ghajar [40].

Type	Author	Correlation
H	Nishima & Yamazaki <sup>b</sup>	$\alpha = 1 - \left( \frac{1-x}{x} \frac{\rho_g}{\rho_l} \alpha_H \right)^{0.5}$
H	Czop et al. <sup>b</sup>	$\alpha = -0.285 + 1.097\alpha_H$
H	Armand <sup>c</sup>	$\alpha = 0.833\alpha_H$
H	Guzhov et. al. <sup>b</sup>	$\alpha = 0.81\alpha_H \left( 1 - \exp^{-2.2Fr^{0.5}} \right)$
H	Chisholm <sup>b</sup>	$\alpha = \frac{\alpha_H}{\alpha_H + (1-\alpha_H)^{0.5}}$
S	Lockhart & Martinelli <sup>a</sup>	$\alpha = \left[ 1 + 0.28 \left( \frac{1-x}{x} \right)^{0.64} \left( \frac{\rho_g}{\rho_l} \right)^{0.36} \left( \frac{\mu_g}{\mu_l} \right)^{0.07} \right]^{-1}$
S	Spedding & Chen <sup>a</sup>	$\alpha = \left[ 1 + 2.22 \left( \frac{1-x}{x} \right)^{0.65} \left( \frac{\rho_g}{\rho_l} \right)^{0.35} \right]^{-1}$
S	Chen <sup>b</sup>	$\alpha = \left[ 1 + 0.18 \left( \frac{1-x}{x} \right)^{0.6} \left( \frac{\rho_g}{\rho_l} \right)^{0.33} \left( \frac{\mu_g}{\mu_l} \right)^{0.07} \right]^{-1}$
S	Fauske <sup>b</sup>	$\alpha = \left[ 1 + \left( \frac{1-x}{x} \right) \left( \frac{\rho_g}{\rho_l} \right)^{0.5} \right]^{-1}$
S	Thom <sup>b</sup>	$\alpha = \left[ 1 + \left( \frac{1-x}{x} \right) \left( \frac{\rho_g}{\rho_l} \right)^{0.89} \left( \frac{\mu_g}{\mu_l} \right)^{0.18} \right]^{-1}$
S	Zivi <sup>b</sup>	$\alpha = \left[ 1 + \left( \frac{1-x}{x} \right) \left( \frac{\rho_g}{\rho_l} \right)^{0.67} \right]^{-1}$
S	Turner & Wallis <sup>b</sup>	$\alpha = \left[ 1 + \left( \frac{1-x}{x} \right)^{0.72} \left( \frac{\rho_g}{\rho_l} \right)^{0.4} \left( \frac{\mu_g}{\mu_l} \right)^{0.08} \right]^{-1}$
S	Baroczy <sup>b</sup>	$\alpha = \left[ 1 + \left( \frac{1-x}{x} \right)^{0.74} \left( \frac{\rho_g}{\rho_l} \right)^{0.65} \left( \frac{\mu_g}{\mu_l} \right)^{0.13} \right]^{-1}$

Table 1 – (Continue)

Type	Author	Correlation
S	Smith <sup>b</sup>	$\alpha = \left[ 1 + A_S \left( \frac{1-x}{x} \right) \left( \frac{\rho_g}{\rho_l} \right) \right]^{-1}$ $A_S = 0.4 + 0.6 \sqrt{\frac{\left( \frac{\rho_g}{\rho_l} \right) + 0.04 \left( \frac{1-x}{x} \right)}{1 + 0.04 \left( \frac{1-x}{x} \right)}}$
S	Chisholm <sup>b</sup>	$\alpha = \left[ 1 + A_S \left( \frac{1-x}{x} \right) \left( \frac{\rho_g}{\rho_l} \right) \right]^{-1}$ $A_S = 0.4 + 0.6 \sqrt{1 - x \left( 1 - \frac{\rho_g}{\rho_l} \right)}$
S	Hamersma & Hart <sup>b</sup>	$\alpha = \left[ 1 + 0.26 \left( \frac{1-x}{x} \right)^{0.67} \left( \frac{\rho_g}{\rho_l} \right)^{0.33} \right]^{-1}$
S	Xu & Fang <sup>a</sup>	$\alpha = \left[ 1 + \left( 1 + 2Fr_{lo}^{-0.2} \alpha_l^{3.5} \right) \left( \frac{1-x}{x} \right) \left( \frac{\rho_g}{\rho_l} \right) \right]^{-1}$
D	Dix <sup>c</sup>	$C_0 = \frac{j_g}{j_g + j_l} \left[ 1 + \left( \frac{j_l}{j_g} \right) \left( \frac{\rho_g}{\rho_l} \right)^{0.1} \right]$ $j_{gm} = 2.9 \left[ \frac{g\sigma(\rho_l - \rho_g)}{\rho_l^2} \right]$
D	Toshiba <sup>c</sup>	$\alpha = \frac{j_g}{1.08j_l + 0.45}$
D	Jowitt et al. <sup>b</sup>	$C_0 = 1 + 0.796 e^{(0.061 \sqrt{\frac{\rho_g}{\rho_l}})}$ $j_{gm} = 0.034 \left( \sqrt{\frac{\rho_g}{\rho_l}} - 1 \right)$
D	Nicklin et al. <sup>b</sup>	$\alpha = \frac{j_g}{1.2j_l + 0.35 \sqrt{gD}}$
D	Rouhani & Axelsson <sup>a</sup>	$C_0 = 1 + 0.2(1-x) \left( \frac{gD\rho_l^2}{G_m^2} \right)^{0.25}, \alpha \leq 0.1$ $C_0 = 1 + 0.2(1-x), \alpha \geq 0.1$ $j_{gm} = 1.18 \left[ \frac{g\sigma(\rho_l - \rho_g)}{\rho_l^2} \right]^{0.25}$
D	Bonnecaze et al. <sup>b</sup>	$C_0 = 1.2$ $j_{gm} = 0.35(gD)^{0.5} \left( 1 - \frac{\rho_g}{\rho_l} \right)$

Table 1 – (Continue)

Type	Author	Correlation
D	Greskovich & Cooper <sup>b</sup>	$C_0 = \frac{1}{0.82+0.18\left(\frac{P_{sys}}{P_{crit}}\right)}$ $j_{gm} = 0.671(gD)^{0.5}(Sin\theta)^{0.263}$
D	Sun et al. <sup>b</sup>	$C_0 = \frac{1}{0.82+0.18\left(\frac{P_{sys}}{P_{crit}}\right)}$ $j_{gm} = 1.41 \left[ \frac{g\sigma(\rho_l - \rho_g)}{\rho_l^2} \right]^{0.25}$
D	Bestion <sup>b</sup>	$C_0 = 1$ $j_{gm} = 0.188 \left[ \frac{gD(\rho_l - \rho_g)}{\rho_l} \right]^{0.5}$
D	Mattar & Gregory <sup>b</sup>	$C_0 = 1.3$ $j_{gm} = 0.7$
D	Mishima & Hibiki <sup>b</sup>	$C_0 = 1.2 + 0.51e^{-0.691D}$ $j_{gm} = 0$
D	Woldesemayat & Ghajar [40]	$C_0 = \frac{j_g}{j_g + j_l} \left[ 1 + \left( \frac{j_l}{j_g} \right) \left( \frac{\rho_g}{\rho_l} \right)^{0.1} \right]$ $j_{gm} = 2.9 \left[ \frac{gD\sigma(1+Cos\theta)(\rho_l - \rho_g)}{\rho_l^2} \right]^{0.25} (1.22 +$ $1.22Sin\theta) \left( \frac{P_{atm}}{P_{syst}} \right)$
D	Hughmark <sup>a</sup>	$\alpha = \frac{j_g}{1.2j}$
D	Hibiki & Ishii [41]	$C_0 = 1.2 - 0.2 \left( \frac{\rho_g}{\rho_l} \right)$ $j_{gm} = 0.92 \left( \frac{\rho_g}{\rho_l} \right)^{-0.157} N_{\mu_l}^{-0.562}$ $N_{\mu_l} = \frac{\mu_l}{\left[ \rho_l \sigma \left( \frac{\sigma}{g(\rho_l - \rho_g)} \right)^{0.5} \right]^{0.5}}$

Moving onto the tests performed in the calibration facility, for the comparison to be made, certain parameters have to be calculated. The superficial velocities  $j_g$  and  $j_l$ , mass flow quality ( $x_f$ ), homogeneous void fraction ( $\alpha_H$ ) and the mass flux ( $G_m$ ) are highly important for the correlations to be employed.

As to how the  $j_l$  was calculated, it just simply was utilized the inner tube diameter of the sight-glass (15 mm) and the volumetric flow read by the water flowmeter in the facility. The value is obtained with the Eq. (4.28).

$$j_l = \frac{\dot{V}_l}{A} \quad (4.28)$$

For the calculation of  $j_g$ , the gas-phase velocity ( $u_g$ ) has to be obtained in the case of the impedance needle-probe sensor utilizing its data. This is made by measuring the distance between the needles' tips over the time between the voltage rises and falls of the needles when a bubble passes through (Eq. 4.29). The time is basically obtain by counting the number of data points between voltage peaks of the needles and dividing this by the sample rate, which, in this case, it was 10,000 sps (Eq. 4.30).

$$u_g = \frac{d_{ndl}}{t_{ndl}} \quad (4.29)$$

$$t_{ndl} = \frac{\text{Number of data points between voltage peaks}}{\text{Sample rate}} \quad (4.30)$$

Then,  $j_g$  is calculated as follows:

$$j_g = u_g \alpha_m \quad (4.31)$$

In the drift flux model, where relative motion and separated flows are considered, the drift flux ( $j_f$ ) is given by the product of the drift velocity ( $u_j$ ) and the void fraction ( $\alpha$ ). The drift velocity is the velocity that separates from the total

superficial velocity ( $j$ ) regarding a mean velocity ( $u$ ). In this case, the gas phase is the main focus. That said:

$$j_{gf} = \alpha u_{gj} \quad (4.32)$$

$$u_{gj} = u_g - j \quad (4.33)$$

This means  $u_g$  can be expressed as the sum of  $j$  and  $u_{gj}$ . But, in the drift flux model homogeneous flows are not possible, so a distribution parameter,  $C_0$ , affects the superficial velocity, meaning that:

$$u_{gj} = u_g - C_0 j \quad (4.34)$$

And thus, the value of  $u_g$  can be expressed as:

$$\frac{u_g}{j} = C_0 + \frac{u_{gj}}{j} \quad (4.35)$$

A relation can be made with the volumetric quality ( $\beta$ ), which is the relation of the volumetric gas flow and the volumetric flow.

$$\beta = \frac{\dot{V}_g}{\dot{V}} \quad (4.36)$$

Since

$$j = \frac{\dot{V}}{A} \quad (4.37)$$

and

$$u_g = \frac{\dot{V}_g}{A_g} \quad (4.38)$$

Then,

$$\beta = \frac{A_g u_g}{A j} \quad (4.39)$$

Meaning that, if Eq. (4.39) is rearranged and replaced in Eq. (4.35), the relation between the void fraction and the volumetric quality can be expressed as:

$$\frac{\beta}{\alpha} = C_0 + \frac{u_{gj}}{j} \quad (4.40)$$

This means that, for a case of no relative motion between phases ( $U_{gj} = 0$ ),  $C_0$  is equal to the relation between  $\alpha$  and  $\beta$ . Considering that, in a homogeneous flow it follows that:

$$\alpha = \alpha_H = \beta \quad (4.41)$$

Knowing that the ideal, or homogeneous, void fraction is a ratio of the space occupied by the gas phase and obtaining  $\beta$  with the superficial velocities, the equation of the homogeneous void fraction can be rearranged in terms of the mass quality.

$$\alpha_H = \beta = \frac{1}{1 + \left[ \left( \frac{1-x}{x} \right) \left( \frac{\rho_g}{\rho_l} \right) \right]} \quad (4.42)$$

$$x_f = \frac{\beta \rho_{gl}}{1 - \beta + \beta \rho_{gl}} \quad (4.43)$$

Where  $\beta \neq \frac{1}{\rho_{gl}-1}$  and  $\rho_{gl} = \left( \frac{\rho_g}{\rho_l} \right)$

Lastly, the mass flux of the mixture,  $G_m$ , is obtained as follows:

$$\dot{V}_g = \frac{\dot{m}_g}{\rho_g} \quad (4.44)$$

$$\dot{V}_l = \frac{\dot{m}_l}{\rho_l} \quad (4.45)$$

$$\dot{V} = \dot{V}_g + \dot{V}_l \quad (4.46)$$

Where  $\dot{m}$  is the mass flow, which is the product of the density, the velocity ( $u$ ) and the transversal area ( $A$ ) (which is obtained from [Eq. 1.3](#)) of the respective phase. Also, for  $u_l$  to be calculated,  $j_l$  has to be divided by  $1-\alpha$ . Thus, replacing Eqs. [\(4.44\)](#) and [\(4.45\)](#) in [Eq. \(4.46\)](#), the mass flow of the mixture can be represented as follows:

$$\dot{V} = \rho_g u_g A_g + \rho_l u_l A_l = \rho_g u_g A \alpha + \rho_l u_l A (1 - \alpha) \quad (4.47)$$

Thus,  $G_m$  is calculated as:

$$G_m = \frac{\dot{V}}{A} \quad (4.48)$$

Utilizing these parameters, the correlations can be handled with the tests results. It is important to note that all the correlations employed in this work, need superficial velocities and not phase velocities, since most of them are based on a transversal area flow.

## 4.6 NOMENCLATURE

$\langle FV_i \rangle$	Void fraction of a frame
C	Capacitance, [F]
$C_0$	Distribution parameter
$d_{ndl}$	Needles tips gap, [m]
D	Tube diameter, [m]
$D^*$	Non-dimensional tube diameter
$FV'$	Time-averaged void fraction
g	Gravity, [ $m/s^2$ ]
$G_m$	Mixture mass flux, [ $kg/m^2s$ ]
$j$	Phase velocity, [m/s]
$m$	Number of columns
$N$	Total captured frames
$n$	Number of rows
$P_{atm}$	Atmospheric pressure, [atm]
$P_{crit}$	Critical pressure, [Pa]
$P_{sys}$	System pressure, [Pa]
PDF	Probability density function
$Pix_i$	Pixel quantity distinct from 1
$t_{ndl}$	Time between voltage peaks of the needles, [s]
u	Velocity, [m/s]
V	Voltage, [V]
$v_m$	Mixture velocity, [m/s]
$v_{sb}$	Bubble rise velocity, [m/s]
$v_{Tb}$	Taylor-bubble transition velocity, [m/s]
$\dot{V}$	Volumetric flow, [ $m^3/s$ ]
x	Mass quality
Z	Electrical impedance, [ $\Omega$ ]



*Greek letters*

$\alpha$	Void fraction
$\theta$	Inclination angle, [°]
$\mu$	Dynamic viscosity, [kg/ms]
$\rho$	Density, [kg/m <sup>3</sup> ]
$\rho_m$	Mixture density, [kg/m <sup>3</sup> ]
$\sigma$	Surface tension, [kg/s <sup>2</sup> ]

*Subscript*

AM	Annular Mist-MPR
BS	Bubbly-Slug
CD	Inverted Annular/Inverted Slug – Inverted Slug
DE	Slug-Slug/Annular – Mist
$g$	Gaseous phase
H	Homogeneous
$l$	Liquid phase
SA	Slug-Annular

*Dimensionless parameters*

Fr	Froude number
Fr <sub>lo</sub>	Liquid-only Froude number
N <sub>μ</sub>	Viscous number

## 4.7 REFERENCES

- [1] Gardenghi, L. R., Filho, E. D. S., Chagas, D. G., Scagnolatto, G., Oliveira, R. M., & Tibiriçá, C. B. (2020). [Overview of Void Fraction Measurement Techniques, Databases and Correlations for Two-Phase Flow in Small Diameter Channels](#). *Fluids*, 5(4), 216. <sup>a b</sup>
- [8] Universitat Politècnica de València - UPV. (2017, October 19). MAPA DE REGÍMENES DE CAUDAL BIFÁSICO EN TUBERÍAS VERTICALES — — UPV [Video]. YouTube. [https://www.youtube.com/watch?v=lJL2249d0EM&ab\\_channel=UniversitatPolit%C3%A8nicadeVal%C3%A8ncia-UPV](https://www.youtube.com/watch?v=lJL2249d0EM&ab_channel=UniversitatPolit%C3%A8nicadeVal%C3%A8ncia-UPV) <sup>a b</sup>
- [35] Simões-Moreira, J. R. (2008, noviembre). Void Fraction Measurement and Signal Analysis from Multiple-Electrode Impedance Sensors. *Heat Transfer Engineering*, 29(11), 924-935. <https://doi.org/10.1080/01457630802186015> <sup>a</sup>
- [36] Chung, Bub Dong, Bae, Sung Won, Lee, Seung Wook, Yoon, Churl, Hwang, Moon Kyu, Kim, Kyung Doo, & Jeong, Jae Jun (2010). MARS CODE MANUAL VOLUME V: Models and Correlations (KAERI/TR-3872/2009). Korea, Republic of. [https://inis.iaea.org/search/search.aspx?orig\\_q=RN:42004666](https://inis.iaea.org/search/search.aspx?orig_q=RN:42004666) <sup>a b</sup>
- [37] Taitel, Y., Barnea, D., & Dukler, A. E. (1980). Modelling flow pattern transitions for steady upward gas-liquid flow in vertical tubes. *Aiche Journal*, 26(3), 345–354. <https://doi.org/10.1002/aic.690260304> <sup>a</sup>
- [38] Hibiki, T., Ishii, M., & Xiao, Z. (2001). Axial interfacial area transport of vertical bubbly flows. *International Journal of Heat and Mass Transfer*, 44(10), 1869–1888. [https://doi.org/10.1016/s0017-9310\(00\)00232-5](https://doi.org/10.1016/s0017-9310(00)00232-5) <sup>a b</sup>
- [39] Xia, G., Cai, B., Cheng, L., Wang, Z., & Jia, Y. (2018). Experimental study and modelling of average void fraction of gas-liquid two-phase flow in a helically coiled rectangular channel. *Experimental Thermal and Fluid Science*, 94, 9–22.

<https://doi.org/10.1016/j.expthermflusci.2018.01.027> <sup>a b</sup>

[40] Woldesemayat, M. A., & Ghajar, A. J. (2007). Comparison of void fraction correlations for different flow patterns in horizontal and upward inclined pipes. *International Journal of Multiphase Flow*, 33(4), 347–370. <https://doi.org/10.1016/j.ijmultiphaseflow.2006.09.004> <sup>a b c</sup>

[41] Hibiki, T., & Ishii, M. (2003). One-dimensional drift–flux model for two-phase flow in a large diameter pipe. *International Journal of Heat and Mass Transfer*, 46(10), 1773–1790. [https://doi.org/10.1016/S0017-9310\(02\)00473-8](https://doi.org/10.1016/S0017-9310(02)00473-8) <sup>a b</sup>

# RESULTS

---

## 5.1 IMPEDANCE NEEDLE PROBE SENSOR

The information obtained by this sensor comes from each probe tip, where the voltage, due to the change of impedance whenever the phase proportions inside the flow change, is read independently from either of the tips. Notwithstanding this, both lectures aside from being almost the same, they have a separated time from each other. Each signal is averaged in time as to obtain the void fraction of the flow. It can be used only one needle for this purpose, there is no need of any more except for comparing. However, the reason behind as to why we use two needles is to calculate the velocity of the gas-phase velocity, since with this we can make theoretical drift flux comparisons and also define the flow regime by phase velocities.

In the first run, 14 tests were driven for low and high inlet air flow rates, where the flow rate of the liquid phase was the fixed parameter, and for each one of them, a condition of the gas-phase velocity was studied. Void fraction was acquired utilizing the PDF of each test, with which flow regimes of bubbly, bubbly-slug, slug and slug-churn were identified. [Table 2](#) shows a summary of the flow conditions employed for the impedance needle-probe sensor.

**Table 2 – Impedance needle-probe sensor flow conditions.**

Conditions			High $\dot{V}_g$	Low $\dot{V}_g$
$\dot{V}_l$ ( $\frac{L}{s}$ )	$j_l$ ( $\frac{m}{s}$ )	$Re_l$	$\langle \alpha \rangle$	$\langle \alpha \rangle$
0.25	1.429	21,326	0.123	0.092
0.20	1.132	16,885	0.125	0.090
0.15	0.849	12,663	0.105	0.078
0.10	0.0.566	8,442	0.115	0.087
0.05	0.283	4,221	0.225	0.161
0.03	0.170	2,532	0.319	0.202
0.001	$5.659 \times 10^{-3}$	844.26	0.419	0.354

Regarding the Reynolds number of the superficial liquid velocity, Eq. (5.1) is utilized for its calculation.

$$Re_l = \frac{\rho_l j_l D}{\mu_l} \quad (5.1)$$

The following graphs (Fig. 40 and Fig. 41) show the PDF processed results obtained in the measurement of the two-phase flow parameters by employing the impedance needle-probe void fraction sensor.

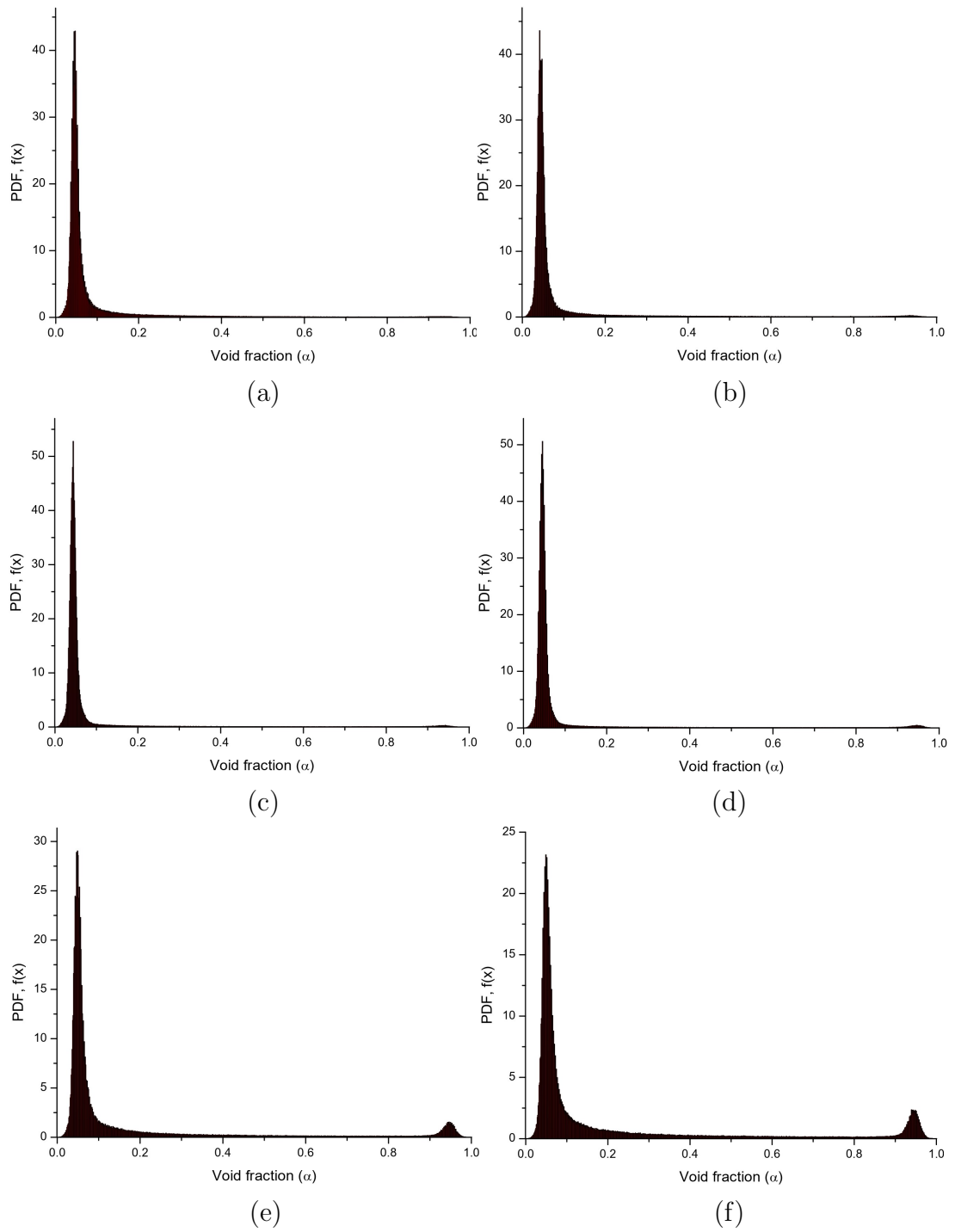
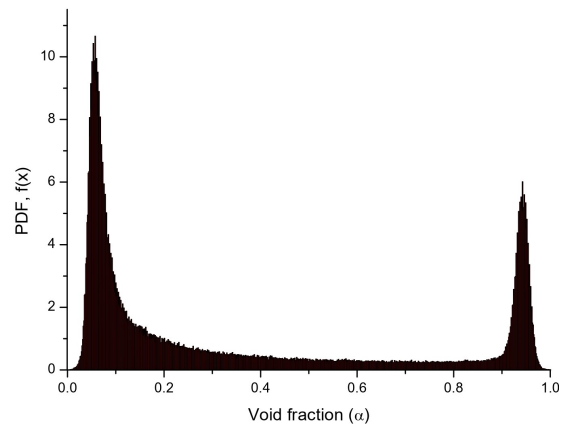
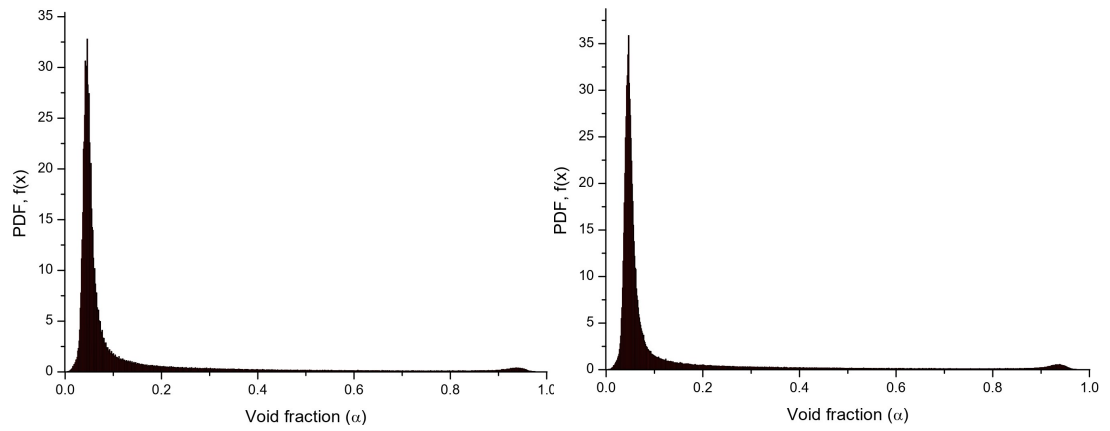


Figure 40 – PDF of void fractions for (a)  $\dot{V}_l = 0.25 \frac{L}{s}$  (b)  $\dot{V}_l = 0.20 \frac{L}{s}$  (c)  $\dot{V}_l = 0.15 \frac{L}{s}$  (d)  $\dot{V}_l = 0.10 \frac{L}{s}$  (e)  $\dot{V}_l = 0.05 \frac{L}{s}$  (f)  $\dot{V}_l = 0.03 \frac{L}{s}$  at low air flow rate.



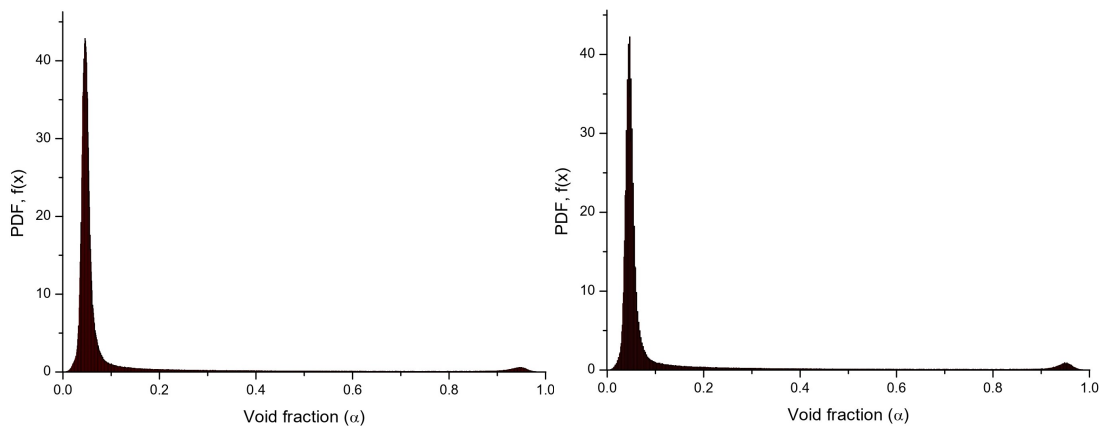
(g)

Figure 40 (Continue) – PDF of void fractions for (g)  $\dot{V}_l = 0.001 \frac{L}{s}$  at low air flow rate.



(a)

(b)



(c)

(d)

Figure 41 – PDF of void fractions for (a)  $\dot{V}_l = 0.25 \frac{L}{s}$  (b)  $\dot{V}_l = 0.20 \frac{L}{s}$  (c)  $\dot{V}_l = 0.15 \frac{L}{s}$  (d)  $\dot{V}_l = 0.10 \frac{L}{s}$  at high air flow rate.

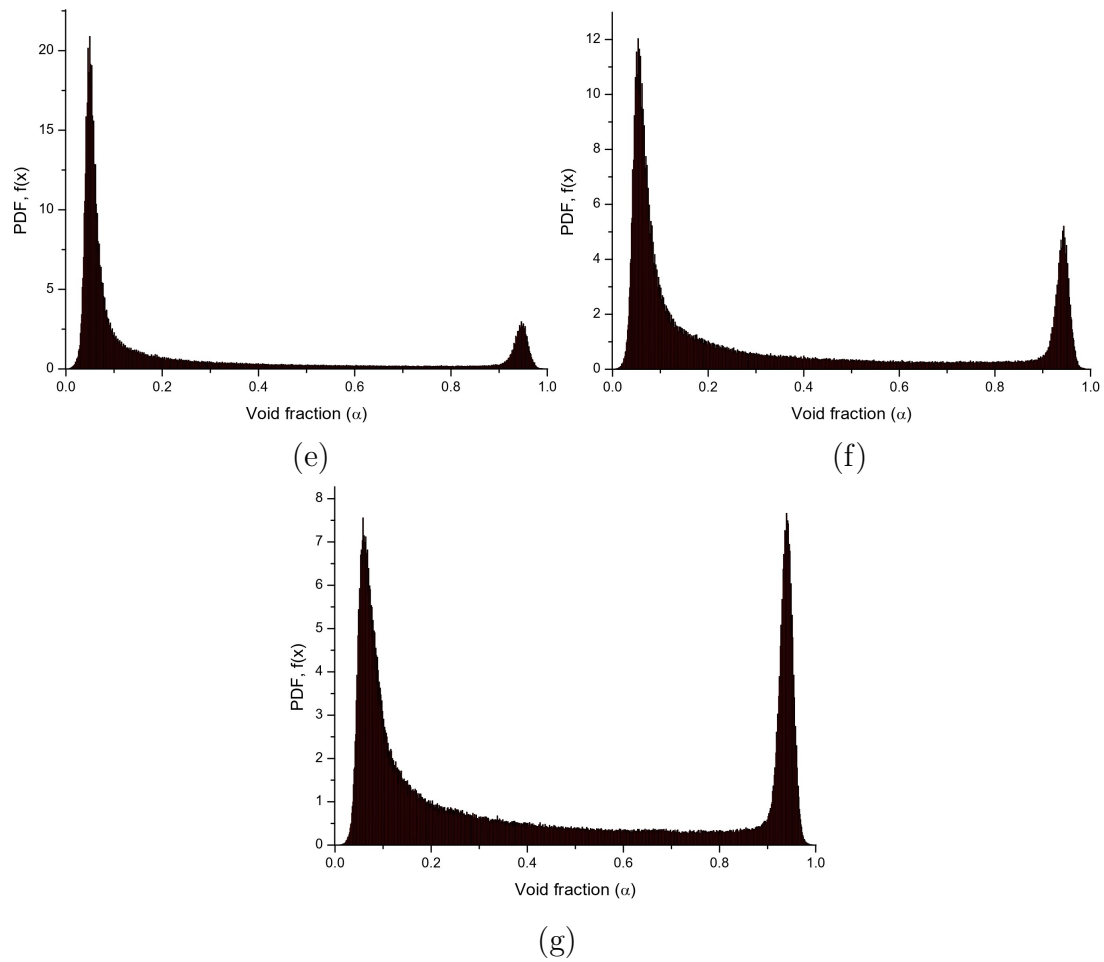


**Figure 41 (Continue) – PDF of void fractions for (e)  $\dot{V}_l = 0.05 \frac{L}{s}$  (f)  $\dot{V}_l = 0.03 \frac{L}{s}$  (g)  $\dot{V}_l = 0.001 \frac{L}{s}$  at high air flow rate.**

A second run (Fig. 42 and Fig. 43) was made at the same conditions displayed before for volumetric flows of 0.05 and 0.03  $\frac{L}{s}$ , but at a higher air flow. It is important to remember that the needles had a 1.2 mm distance from tip to tip and a 1 mm distance from needle to needle.



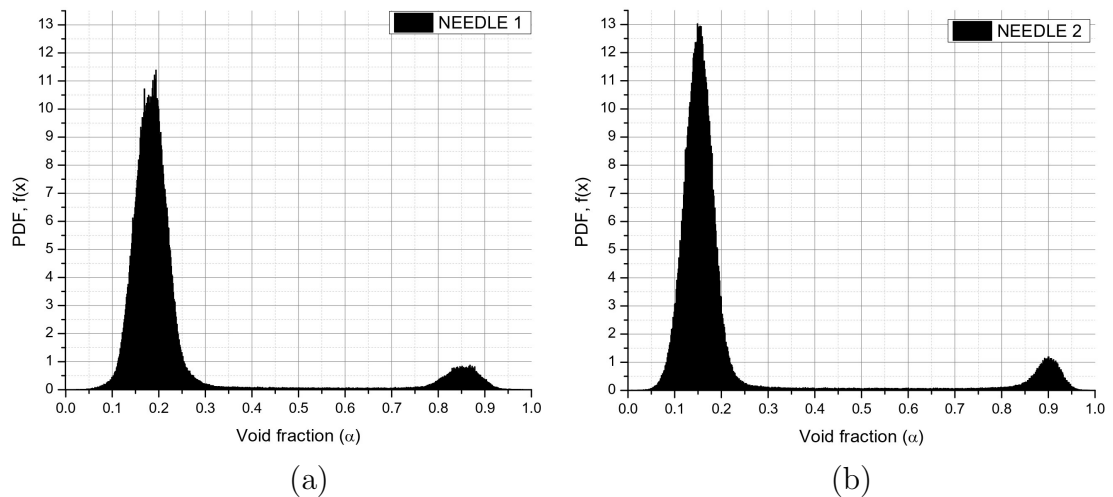


Figure 42 – PDF of void fractions for a water flow rate of  $\dot{V}_l = 0.05 \frac{L}{s}$  in (a) probe tip 1 and (b) probe tip 2.

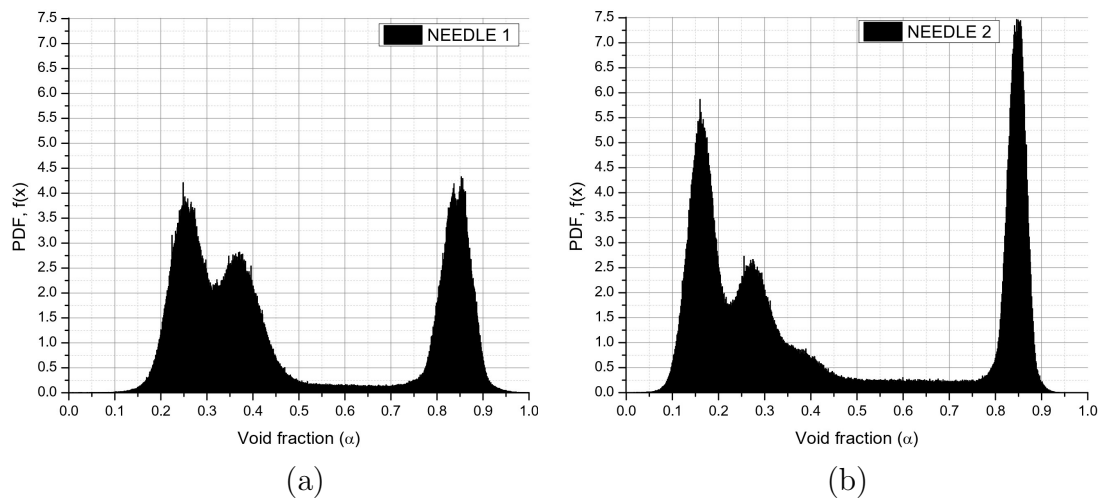


Figure 43 – PDF of void fractions for a water flow rate of  $\dot{V}_l = 0.03 \frac{L}{s}$  in (a) probe tip 1 and (b) probe tip 2.

Fig. 42 demonstrates a bubbly-slug transition flow regime whose time-averaged void fractions were 0.242 and 0.22, being not so different from each other. In Fig. 43 at first glance it was thought that the flow was in a slug flow regime, as some plugs were appearing when looking at the sight-glass, however, as the flow is too fast for the human eye, the sensor showed a different flow regime and time-averaged void fractions of 0.496 and 0.453.

In the following figures 44 and 45, the mean void fraction per second of the second run is shown. It can be seen that the difference between values is not so high, which means that the captured bubbles were mostly those with a high vertical speed regarding the other axial velocities. This can be supported with the fact of the similar behaviour of the curves in the graphs.

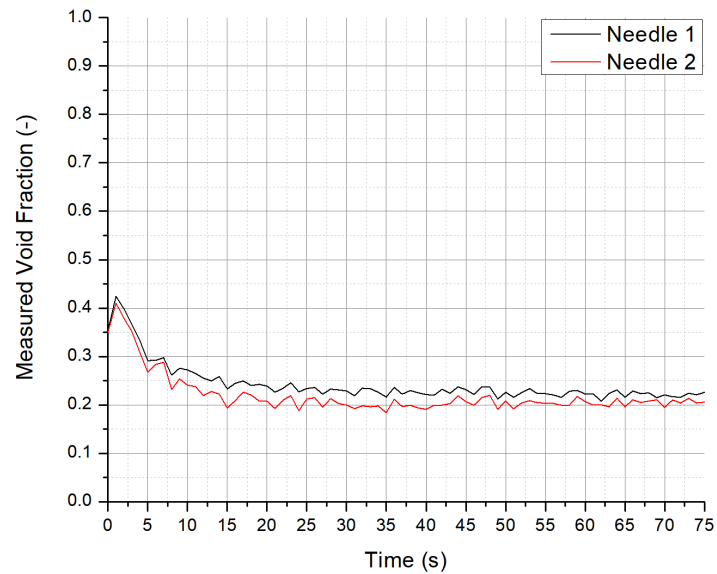


Figure 44 – Impedance needle-probe sensor’s mean void fraction curves measurement for  $\dot{V}_l = 0.05 \frac{L}{s}$  in the second run.

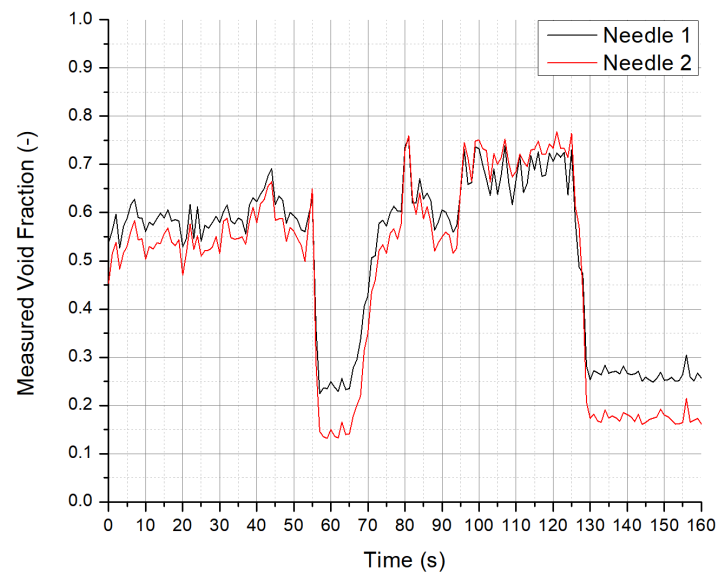


Figure 45 – Impedance needle-probe sensor’s mean void fraction curves measurement for  $\dot{V}_l = 0.03 \frac{L}{s}$  in the second run.

The results shown for different water and air flow rates give an increment on the PDF for higher void fractions as the water flow rate decreases for each fixed air flow rate. It can be seen that at the last test, where high air flow rate with a water flow rate of  $0.03 \frac{L}{s}$  results in a behaviour similar to that of a slug-churn flow regime.

## 5.2 CAPACITANCE ELECTRODE-BASED SENSOR

There were a few issues of the tube not getting well attached to the CPVC, so leakage and deformation of the electrodes were to happen. Indeed, the sensor was tested with the aid of an open water tank, submerging the tube section in the water.

The sensor was, however connected to the selected schering bridge circuit and data was taken from an oscilloscope and it was tested at full air, full water and half immersed volumes. For this, the electrodes were insulated at the outside and utilized frequencies were 2 MHz and 0.5 MHz.

Though the sensor could not make it to the calibration facility due to the attaching issues, it did workout as intended, at least at sensing a change in the measured voltage of the Schering bridge, as this raised to its maximum voltage when it was immersed in air and its minimum value when in water. It did also measure a value between the range of air and water when it was half-immersed in water, leading to a succesful usage of the bridge as the sensing circuit as seen on figures [46](#) and [47](#).

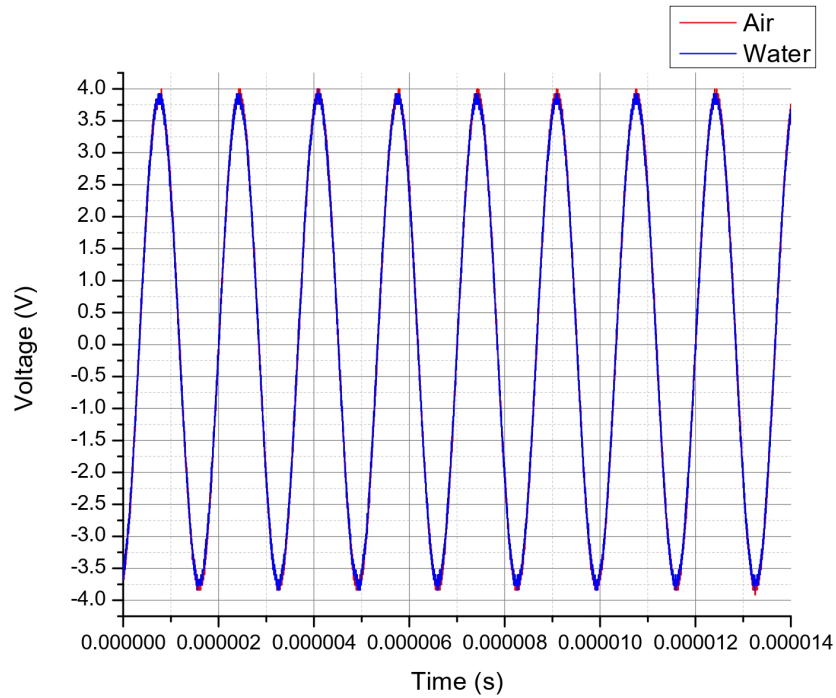


Figure 46 – Comparison of the 500 kHz voltage signals of full air and full water immersion, taken from the oscilloscope.

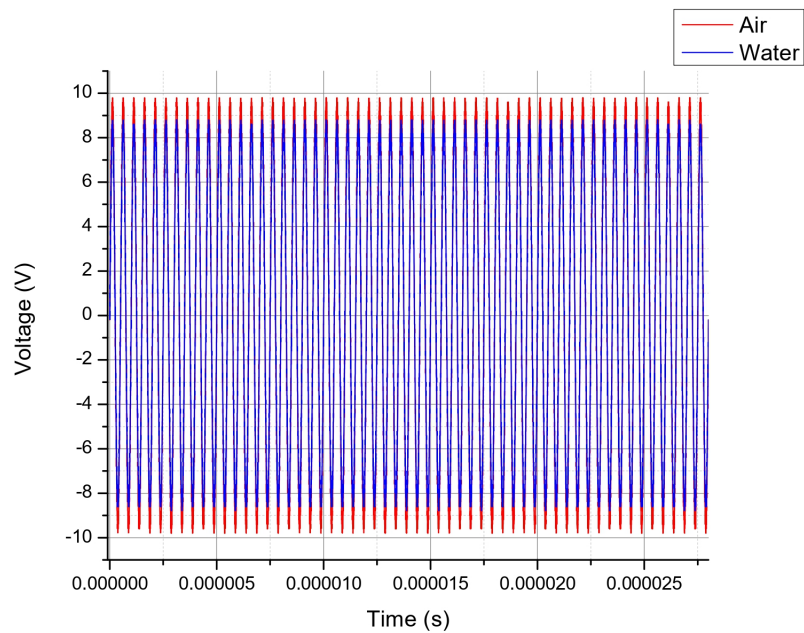


Figure 47 – Comparison of the 2 MHz voltage signals of full air and full water immersion, taken from the oscilloscope.

Even though in Fig. 48 the difference in the peaks may not be visible, when zooming in it can be seen that there is a difference higher than 0.3 V, as it is shown in Fig. 49. In Table 3, the average peak and RMS values of each signal are located. It seems that at 2 MHz the difference in voltage between phases is higher. Moreover, the higher the frequency, the more the probability for the bridge to get saturated, as capacitors may not be able to charge and discharge that fast, so there are limitations in frequency for the usage of the bridge depending of the materials chosen.

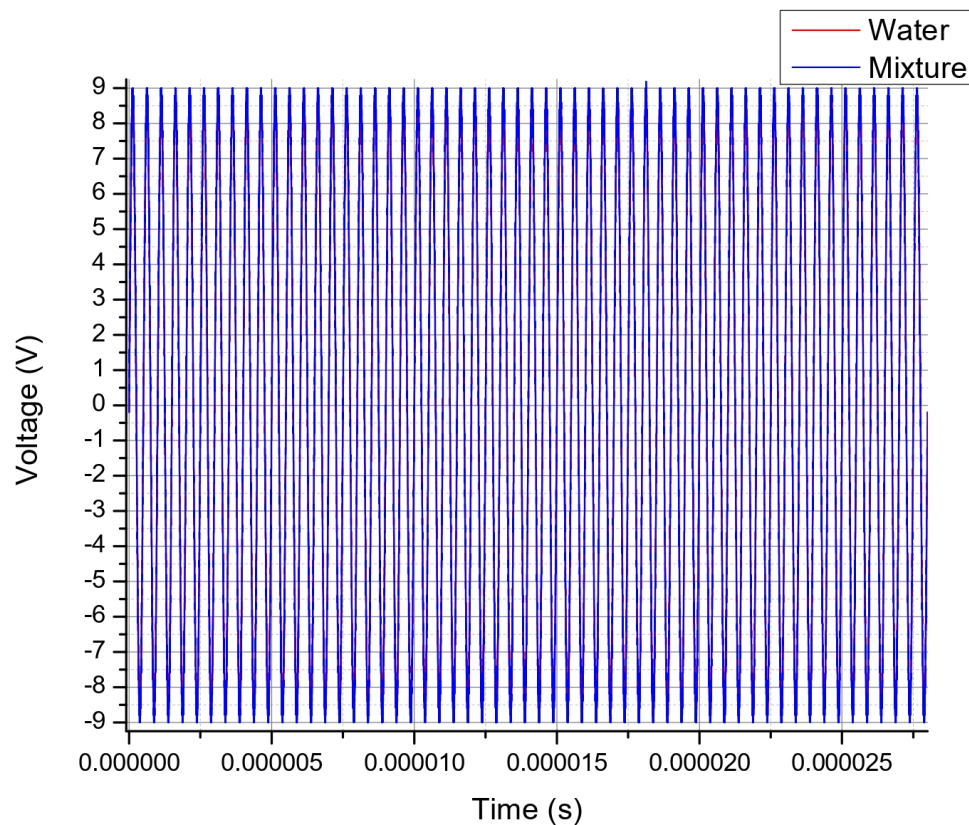


Figure 48 – Comparison of the 2 MHz voltage signals of full water and half stratified mixture immersion, taken from the oscilloscope.

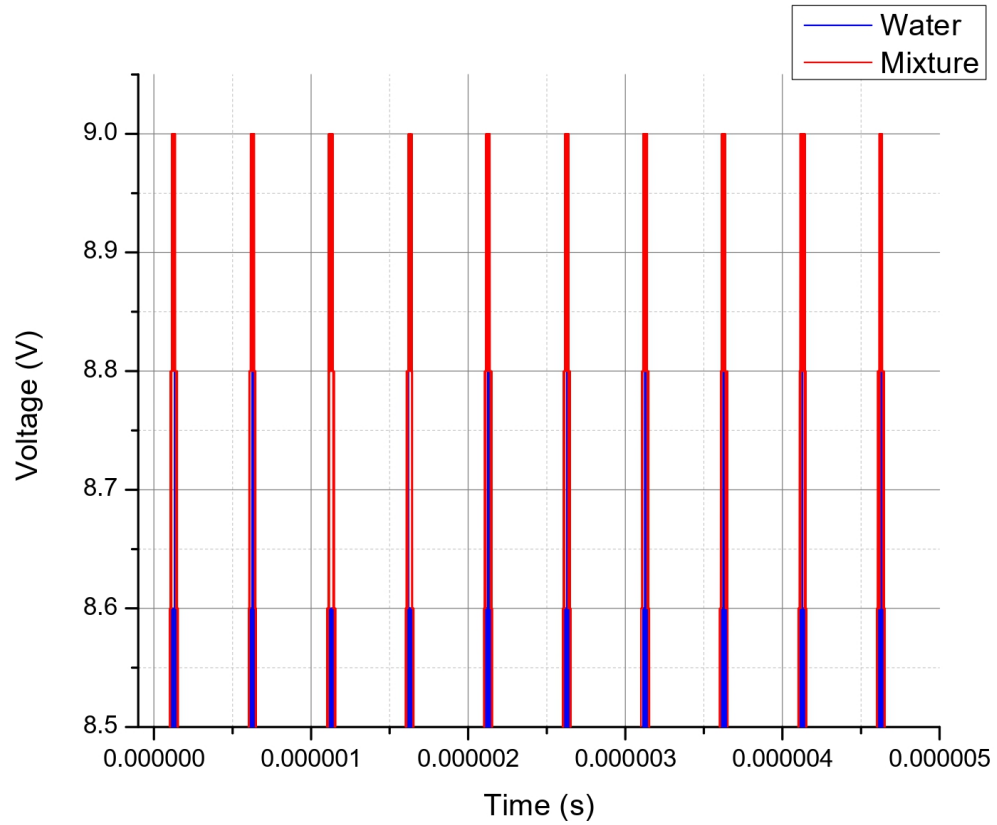


Figure 49 – Zoom in at the comparison of the 2 MHz voltage signals of full water and half stratified mixture immersion.

Table 3 – Average peak voltage and RMS values of the 500 kHz and 2 MHz signals.

Voltage (V)	500 kHz		2 MHz		
	Air	Water	Air	Water	Stratified mixture
Peak voltage ( $V_p$ )	3.88	3.86	9.8	8.8	9.2
RMS ( $V_{RMS}$ )	2.75	2.73	6.93	6.22	6.51

### 5.3 IMAGE ANALYSIS

For starters, the first flow image capture, in order to test the camera, was done with a refrigerant mass charge of 2.8 kg. A pressure and temperature measurement at

the evaporator inlet returned a value of 375.86 kPa and 311.09 K respectively. At the condenser unit outlet, a 1,689.66 kPa pressure, along with a 294.59 K temperature value was delivered for a  $31.92 \times 10^{-3}$  kg/s mass flow rate inside a 1/2" tube diameter. Refrigerant flow is captured at a rate of 19047 fps, a 208x200 pp resolution, an extreme dynamic light rate (EDR) of 28  $\mu$ s with a capture duration of 572 s. The flow is illuminated by a 120W COOPER PAR38 lamp with a luminous flow of 1335 lm at 30 cm from the sight-glass. From the image treatment, with the methodology described (See section 4.1.), the void fraction was determined at 0.812.

All the tests in the calibration facility, however, are aimed to be at different flow regimes and, consequently, void fractions. Since this is for the inlet of an evaporator, the focus is in the bubbly and slug flow regimes range. Unfortunately, tests were only captured for the impedance sensor, since there were some issues connecting the capacitance sensor as mentioned before.

Table 4 summarizes the results obtained from the tests at the calibration facility, where test 1 and 2 were determined visually to be at a bubbly flow regime and test 3 at a slug-churn flow regime.

**Table 4 – Image analysis calculated void fractions and superficial gas velocities.**

Test	$\alpha_{I\text{MAQ}}$	$\dot{j}_{g,I\text{MAQ}}$
No.	-	$\left(\frac{m}{s}\right)$
1	0.216646	0.2559
2	0.292294	0.1839
3	0.557770	0.4588

## 5.4 EXPERIMENTAL TO THEORETICAL COMPARISON

### 5.4.1 VOID FRACTION COMPARISON

For the first facility, in contemplation of the results comparison with correlations, flow properties were determined and depicted (Table 5) by the usage of the measured mass flow rate, pressure and temperature data. Likewise, it was determined with the ASHRAE handbook [42] the flow enthalpy, with a 109.32 kJ/kg value, a 0.427 mass quality and a  $9.281 \times 10^{-3}$  kg/s<sup>2</sup> surface tension.

**Table 5 – R-404A properties of the measured parameters.**

Properties	Liquid	Gas
Density (kg/m <sup>3</sup> )	1202.744	19.147
Enthalpy (kJ/kg)	33.164	211.543
Cinematic viscosity (kg/ms)	$2.132 \times 10^{-4}$	$1.032 \times 10^{-5}$

Analyzing the conditions under which the experiment was carried out, with some models described above, the following comparison was made (Table 6). A deviation of 7.5 % on average was obtained by means of the high-speed image analysis.



**Table 6 – Void fraction of the selected correlations. H = homogeneous, S = slip.** <sup>a</sup> Mentioned by [Gardenghi et al. \[1\]](#); <sup>b</sup> mentioned by [Xia et al. \[39\]](#); <sup>c</sup> mentioned by [Woldesemayat & Ghajar \[40\]](#).

Type	Author	Void fraction
H	Nishima & Yamazaki <sup>b</sup>	0.855359
H	Czop et al. <sup>b</sup>	0.789050
H	Armand <sup>c</sup>	0.815573
H	Guzhov et. al. <sup>b</sup>	0.793054
H	Chisholm <sup>b</sup>	0.871284
S	Lockhart & Martinelli <sup>a</sup>	0.913970
S	Spedding & Chen <sup>a</sup>	0.845836
S	Chen <sup>b</sup>	0.936583
S	Fauske <sup>b</sup>	0.855174
S	Thom <sup>b</sup>	0.945080
S	Zivi <sup>b</sup>	0.922699
S	Turner & Wallis <sup>b</sup>	0.768866
S	Baroczy <sup>b</sup>	0.888912
S	Smith <sup>b</sup>	0.984023
S	Chisholm <sup>b</sup>	0.982019
S	Hamersma & Hart <sup>b</sup>	0.925265
S	Xu & Fang <sup>a</sup>	0.034349

The calibration facility tests' measurements procedures utilized were already described in section 4.5. That said, the calculation of the void fraction for the 33 correlations were diverse for the 3 tests, being the first one mentioned in section 5.1 at a high inlet air flow and a  $\dot{V}_l$  of 0.05 L/s and the last two are from the second run also mentioned later in that section, where Image Analysis was performed at the same time as the Impedance Needle-probe sensor was employed. The calculated superficial gas velocity,  $j_g$ , was obtained both by image and sensor in different ways, as the gas-phase velocity,  $u_g$ , was obtained by the sensor and then multiplied by the

measured void fraction, while  $j_g$  was directly acquired by IMAQ analysis. The first test, however, was only done for the  $u_g$  obtained by image analysis. Therefore, the total number of comparisons is 5.

The sample rate at which the sensor worked was at 10,000 dps. The camera sample rate was 900 fps for the first test and 1,200 fps for the rest. The tests' measured parameters are reviewed in [Table 7](#).

**Table 7 – Experimental tests' measured parameters.**

Test	$\alpha_{Sensor}$	$\alpha_{IMAQ}$	$u_{g,Sensor}$	$j_{g,IMAQ}$	$V_l$	$t_{ndl}$
No.	-	-	$\left(\frac{m}{s}\right)$	$\left(\frac{m}{s}\right)$	$\left(\frac{L}{s}\right)$	s
1	0.225345	0.216646	N/A	0.2559	0.1	N/A
2	0.231073	0.292294	0.5217	0.1839	0.05	0.0023
3	0.474430	0.557770	0.9231	0.4588	0.03	0.0013

Hereafter, the comparisons whose error according to the measured or analysed void fraction was below 20% are shown in [Tables 8, 9](#) and [10](#) for those based on the  $j_g$  of IMAQ and [Tables 11](#) and [12](#) for those based on the  $j_g$  of the sensor. The mean error for all the correlations and those below 20%, as well as the standard deviation, can be seen on [Table 13](#) and [14](#) for the 3 tests and both velocities.

**Table 8** – Experimental to theoretical correlations comparison for test 1 based on  $j_{g, IMAQ} = 0.2559$  m/s. **H** = homogeneous, **S** = slip, **D** = drift flux. <sup>a</sup> Mentioned by **Gardenghi et al. [1]**; <sup>b</sup> mentioned by **Xia et al. [39]**; <sup>c</sup> mentioned by **Woldesemayat & Ghajar [40]**. "I" stands that the error was below 20% according to the IMAQ void fraction, "S" according to the sensor and "B" according to both.

Type	Base Error	Author	$\alpha_{IMAQ \text{ Based}}$
H	B	Nishima & Yamazaki <sup>b</sup>	0.187426
H	B	Guzhov et al. <sup>b</sup>	0.228216
S	B	Lockhart & Martinelli <sup>a</sup>	0.222524
S	B	Spedding & Chen <sup>a</sup>	0.226278
S	B	Hamersma & Hart <sup>b</sup>	0.217286
D	S	Dix <sup>c</sup>	0.269549
D	B	Toshiba <sup>c</sup>	0.202529
D	B	Nicklin et al. <sup>b</sup>	0.245450
D	B	Rouhani & Axelsson <sup>a</sup>	0.246473
D	B	Bonnecaze et al. <sup>b</sup>	0.245503
D	B	Greskovich & Cooper <sup>b</sup>	0.242090
D	B	Sun et al. <sup>b</sup>	0.237103
D	B	Mishima & Hibiki <sup>b</sup>	0.199322

**Table 9** – Experimental to theoretical correlations comparison for test 2 based on  $\dot{j}_{g, IMAQ} = 0.1839$  m/s.

Type	Base Error	Author	$\alpha_{IMAQ}$ Based
H	B	Nishima & Yamazaki <sup>b</sup>	0.241794
H	B	Guzhov et al. <sup>b</sup>	0.267429
S	B	Lockhart & Martinelli <sup>a</sup>	0.265250
S	B	Spedding & Chen <sup>a</sup>	0.270190
S	S	Baroczy <sup>b</sup>	0.204318
S	B	Hammersma & Hart <sup>b</sup>	0.261438
D	B	Dix <sup>c</sup>	0.251953
D	S	Toshiba <sup>c</sup>	0.200505
D	I	Nicklin et al. <sup>b</sup>	0.279586
D	I	Rouhani & Axelsson <sup>a</sup>	0.281428
D	I	Bonnecaze et al. <sup>b</sup>	0.279681
D	B	Greskovich & Cooper <sup>b</sup>	0.276137
D	B	Sun et al. <sup>b</sup>	0.267217
D	B	Mishima & Hibiki <sup>b</sup>	0.249429
D	I	Woldesemayat & Ghajar <a href="#">[40]</a>	0.339736

**Table 10 – Experimental to theoretical correlations comparison for test 3 based on  $j_{g, IMAQ} = 0.4588$  m/s.**

Type	Base Error	Author	$\alpha_{IMAQ}$ Based
H	B	Nishima & Yamazaki <sup>b</sup>	0.504617
H	B	Czop et al. <sup>b</sup>	0.542791
H	I	Armand <sup>c</sup>	0.628578
H	B	Guzhov et al. <sup>b</sup>	0.553941
H	I	Chisholm <sup>b</sup>	0.603687
S	B	Lockhart & Martinelli <sup>a</sup>	0.473319
S	B	Spedding & Chen <sup>a</sup>	0.483162
S	I	Chen <sup>b</sup>	0.587658
S	S	Thom <sup>b</sup>	0.411908
S	S	Baroczy <sup>b</sup>	0.424339
S	B	Hamersma & Hart <sup>b</sup>	0.479080
S	I	Xu & Fang <sup>a</sup>	0.594076
D	S	Dix <sup>c</sup>	0.439749
D	S	Toshiba <sup>c</sup>	0.414585
D	B	Nicklin et al. <sup>b</sup>	0.528405
D	B	Rouhani & Axelsson <sup>a</sup>	0.531347
D	B	Bonnecaze et al. <sup>b</sup>	0.528543
D	B	Greskovich & Cooper <sup>b</sup>	0.521417
D	B	Sun et al. <sup>b</sup>	0.508568
D	S	Mishima & Hibiki <sup>b</sup>	0.442736
D	B	Woldesemayat & Ghajar [40]	0.536780
D	I	Hughmark <sup>a</sup>	0.628830

**Table 11 – Experimental to theoretical correlations comparison for test 2 based on  $u_{g, Sensor} = 0.5217$  m/s.**

Type	Base Error	Author	$\alpha_{Sensor:Based}$
H	B	Armand <sup>c</sup>	0.271981
H	S	Guzhov et al. <sup>b</sup>	0.185891
H	I	Chisholm <sup>b</sup>	0.284620
S	S	Lockhart & Martinelli <sup>a</sup>	0.216006
S	S	Spedding & Chen <sup>a</sup>	0.219579
S	I	Chen <sup>b</sup>	0.319932
S	I	Smith <sup>b</sup>	0.326638
S	I	Chisholm <sup>b</sup>	0.326560
S	S	Hamersma & Hart <sup>b</sup>	0.210583
S	I	Xu & Fang <sup>a</sup>	0.316302
D	S	Dix <sup>c</sup>	0.192135
D	S	Nicklin et al. <sup>b</sup>	0.207236
D	S	Rouhani & Axelsson <sup>a</sup>	0.208765
D	S	Bonnecaze et al. <sup>b</sup>	0.207316
D	S	Greskovich & Cooper <sup>b</sup>	0.204779
D	S	Sun et al. <sup>b</sup>	0.197328
D	S	Mishima & Hibiki <sup>b</sup>	0.191569
D	B	Woldesemayat & Ghajar <a href="#">[40]</a>	0.274701
D	B	Hughmark <sup>a</sup>	0.272090

**Table 12 – Experimental to theoretical correlations comparison for test 3 based on  $u_{g, Sensor} = 0.9231$  m/s.**

Type	Base Error	Author	$\alpha_{Sensor Based}$
H	B	Nishima & Yamazaki <sup>b</sup>	0.495892
H	B	Czop et al. <sup>b</sup>	0.533225
H	I	Armand <sup>c</sup>	0.621314
H	B	Guzhov et al. <sup>b</sup>	0.544371
H	I	Chisholm <sup>b</sup>	0.596708
S	B	Lockhart & Martinelli <sup>a</sup>	0.465900
S	B	Spedding & Chen <sup>a</sup>	0.475612
S	I	Chen <sup>b</sup>	0.580875
S	S	Thom <sup>b</sup>	0.400682
S	S	Baroczy <sup>b</sup>	0.415948
S	B	Hamersma & Hart <sup>b</sup>	0.4713037
S	I	Xu & Fang <sup>a</sup>	0.587918
D	S	Dix <sup>c</sup>	0.430650
D	S	Toshiba <sup>c</sup>	0.403957
D	B	Nicklin et al. <sup>b</sup>	0.519351
D	B	Rouhani & Axelsson <sup>a</sup>	0.522300
D	B	Bonnecaze et al. <sup>b</sup>	0.519490
D	B	Greskovich & Cooper <sup>b</sup>	0.512526
D	B	Sun et al. <sup>b</sup>	0.499529
D	S	Mishima & Hibiki <sup>b</sup>	0.437619
D	B	Woldesemayat & Ghajar [40]	0.528703
D	I	Hughmark <sup>a</sup>	0.621563

**Table 13 – Experimental tests’ mean error and standard deviation based on measured void fractions by the sensor and IMAQ analysis based on  $j_{g, IMAQ}$ .**

Test	$\alpha_{Sensor}$	$\alpha_{IMAQ}$	$ERR_{Sensor}$	$ERR_{IMAQ}$	$\sigma_{st, Sensor}$	$\sigma_{st, IMAQ}$
No.	-	-	%	%	%	%
1	0.225345	0.216646	8.040	8.530	2.210	2.088
2	0.231073	0.292294	12.924	9.565	3.136	3.087
3	0.474430	0.557770	9.173	7.965	4.884	5.026

**Table 14 – Experimental tests’ mean error and standard deviation based on measured void fractions by the sensor and IMAQ analysis based on  $u_{g, Sensor}$ .**

Test	$\alpha_{Sensor}$	$\alpha_{IMAQ}$	$ERR_{Sensor}$	$ERR_{IMAQ}$	$\sigma_{st, Sensor}$	$\sigma_{st, IMAQ}$
No.	-	-	%	%	%	%
2	0.474430	0.557770	13.174	7.956	3.231	2.471
3	0.231073	0.292294	8.700	8.696	4.688	5.359

Finally, the following figures show the distribution of the correlations in a graph of the measured versus the calculated void fraction value based on either  $j_{g, IMAQ}$  or  $u_{g, Sensor}$ . The bold lines are the error lines for 0, 15 and -15 percent.

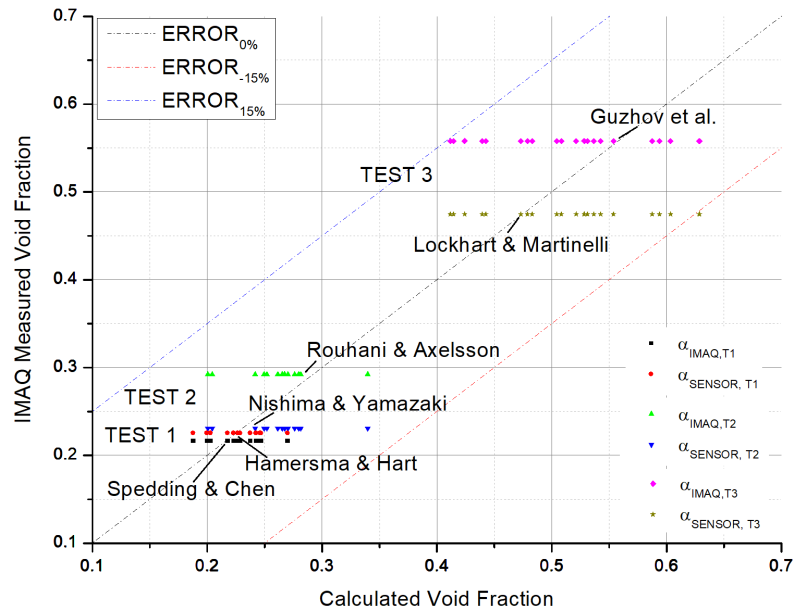


**Figure 45 – Measured vs. calculated void fraction based on  $j_{g, IMAQ}$ .**



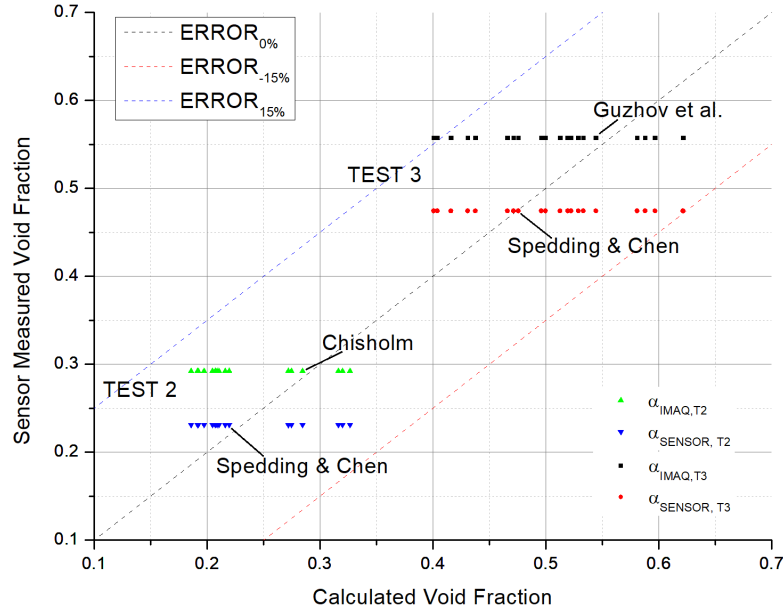


Figure 46 – Measured vs. calculated void fraction based on  $u_{g, \text{Sensor}}$ .

#### 5.4.2 FLOW REGIME COMPARISON

By utilizing the methods mentioned in section 4.4, according to Chung et al. [36], the tests had a critical diameter of 25 mm, which indicates that no bubbly flow can theoretically exist and, when introducing the data to the 3-D flow regime map, it results and an unstratified slug flow. Nevertheless, when utilizing the second method (overlapping the results and the air-water flow regime map), it seems that the smoothed map of Hibiki et al. [38] targets the point value of the velocities of the second test based on  $u_{g, \text{IMAQ}}$  as a bubbly flow regime, whereas for the first test and the other point value of the second test are near the boundary of the bubbly and slug flow regimes. This might mean that these points are in transition, while the last test, on both cases, the flow regime is nearly at the center of the slug flow regime.

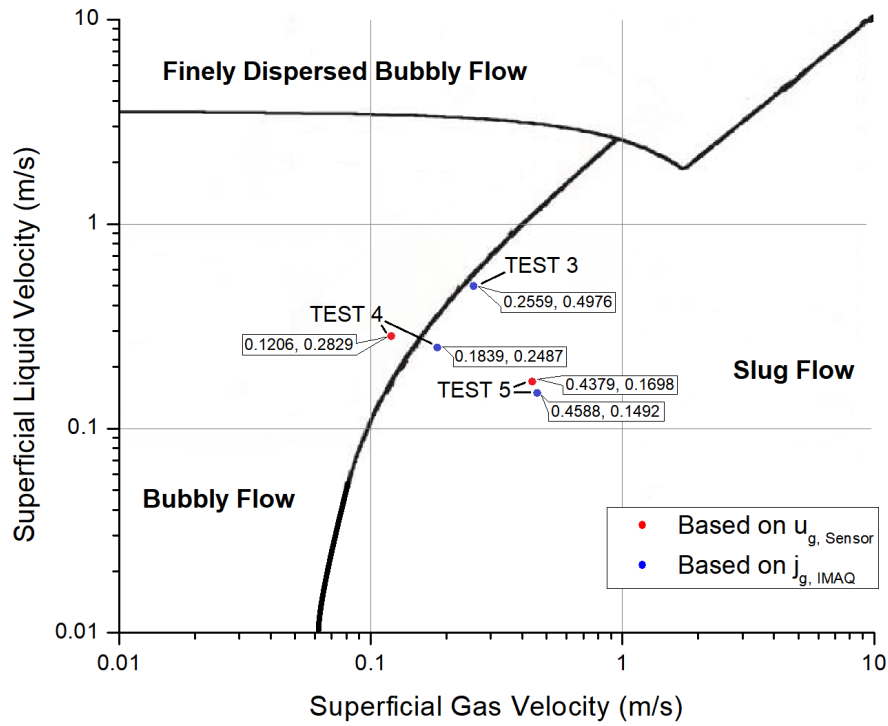


Figure 47 – Tests’ superficial gas velocity versus superficial liquid velocity flow regime map.

It is important to note that  $j_{g, \text{Sensor}}$  was obtained with Eq. (4.31).

## 5.5 NOMENCLATURE

$\langle FV_i \rangle$	Void fraction of a frame
C	Capacitance, [F]
$C_0$	Distribution parameter
$d_{ndl}$	Needles tips gap, [m]
D	Tube diameter, [m]
$D^*$	Non-dimensional tube diameter
$FV'$	Time-averaged void fraction
g	Gravity, [m/s <sup>2</sup> ]
$G_m$	Mixture mass flux, [kg/m <sup>2</sup> s]
$j$	Superficial velocity, [m/s]
$m$	Number of columns
$N$	Total captured frames
$n$	Number of rows
PDF	Probability density function
$\text{Pix}_i$	Pixel quantity distinct from 1
$t_{ndl}$	Time between voltage peaks of the needles, [s]
u	Velocity, [m/s]
V	Voltage, [V]
$\dot{V}$	Volumetric flow, [m <sup>3</sup> /s]
x	Mass quality

*Greek letters*

$\alpha$	Void fraction
$\theta$	Inclination angle, [°]
$\mu$	Dynamic viscosity, [kg/ms]
$\rho$	Density, [kg/m <sup>3</sup> ]
$\rho_m$	Mixture density, [kg/m <sup>3</sup> ]
$\sigma$	Surface tension, [kg/s <sup>2</sup> ]

*Subscript*

$g$	Gaseous phase
H	Homogeneous
$l$	Liquid phase

*Dimensionless parameters*

Fr	Froude number
Fr <sub>lo</sub>	Liquid-only Froude number
N <sub>μ</sub>	Viscous number
Re	Reynolds number

## 5.6 REFERENCES

- [1] Gardenghi, L. R., Filho, E. D. S., Chagas, D. G., Scagnolatto, G., Oliveira, R. M., & Tibiriçá, C. B. (2020). [Overview of Void Fraction Measurement Techniques, Databases and Correlations for Two-Phase Flow in Small Diameter Channels](#). *Fluids*, 5(4), 216. <sup>a</sup>
- [36] Chung, Bub Dong, Bae, Sung Won, Lee, Seung Wook, Yoon, Churl, Hwang, Moon Kyu, Kim, Kyung Doo, & Jeong, Jae Jun (2010). MARS CODE MANUAL VOLUME V: Models and Correlations (KAERI/TR-3872/2009). Korea, Republic of. [https://inis.iaea.org/search/search.aspx?orig\\_q=RN:42004666](https://inis.iaea.org/search/search.aspx?orig_q=RN:42004666) <sup>a</sup>
- [38] Hibiki, T., Ishii, M., & Xiao, Z. (2001). Axial interfacial area transport of vertical bubbly flows. *International Journal of Heat and Mass Transfer*, 44(10), 1869–1888. [https://doi.org/10.1016/s0017-9310\(00\)00232-5](https://doi.org/10.1016/s0017-9310(00)00232-5) <sup>a</sup>
- [39] Xia, G., Cai, B., Cheng, L., Wang, Z., & Jia, Y. (2018). Experimental study and modelling of average void fraction of gas-liquid two-phase flow in a helically coiled rectangular channel. *Experimental Thermal and Fluid Science*, 94, 9–22. <https://doi.org/10.1016/j.expthermflusci.2018.01.027> <sup>a</sup>
- [40] Woldesemayat, M. A., & Ghajar, A. J. (2007). Comparison of void fraction correlations for different flow patterns in horizontal and upward inclined pipes. *International Journal of Multiphase Flow*, 33(4), 347–370. <https://doi.org/10.1016/j.ijmultiphaseflow.2006.09.004> <sup>a</sup>
- [42] A. (2021). 2021 ASHRAE Handbook – Fundamentals (I-P). Ashrae. <sup>a</sup>

## CONCLUSIONS

---

Obtaining the void fraction in a two-phase flow for the calibration of void fraction sensors is somewhat easy to acquire and interpret. Bearing this in mind, the present work's achievements and results are summarized hereafter:

1. The void fractions (shown in [Table 13](#) and [Table 14](#)) and the mass qualities of the systems were successfully obtained, which is an important result, as a more precise determination of the cooling capacity on nowadays systems may be possible, since this is currently being calculated supposing an isenthalpic expansion process.
2. The first sight-glass was successful in emphasizing the acquisition of the void fraction as a means to acquire more precise information of the state of the working fluid (in this case, R-404A at 375 kPa) in the evaporator, in order to obtain an accurate and reliable response to the efficiency of the system. Nonetheless, the implementation of an accurate sight-glass for the measurement of the mean gas-phase velocity is still pending, as only void fraction could be determined.
3. An experimental facility was built as part of the calibration system and had been designed to obtain two-phase flow systems of water and air with different flow conditions, so the void fraction could be acquired in different flow regimes.

This in order to identify the flow regime from the analysis of the speed and void fraction data given by the signals, which are obtained from the sensors, in comparison with the image analysis and correlations as seen on [Figs. 45, 46](#) and [47](#).

4. A simple low-cost impedance void fraction sensor was designed and built, which was capable to measure low to medium void fractions with a low standard deviation regarding the correlations and the image analysis. It was also capable to measure the mean gas-phase velocity at a high sample rate and, consequently, determine the local flow regime of the system.
5. A prototype of the electrode-based capacitance sensor was built, which captured the differences of the voltage due the change in the system's capacitance. Unfortunately, it was not possible to attach it to the calibration facility due to some mechanical issues.
6. The experimental results were analyzed and compared to those of the theoretical results from the correlations. The mean error and standard deviation for the tests performed at both facilities were below the 20 %, which is a good result that might give reliability to the measurements.

Most correlations that had lower error were those on the drift flux model. The reason might be due to that most of the more accurate correlations were not highly influenced by the densities, and usually drift flux models have two parameters that affect the void fraction: the distribution parameter ( $C_0$ ) and the drift velocity ( $j_{gj}$ ). These two parameters are commonly based on different properties. When these parameters were calculated, it was found that in most of the drift flux model correlations whose distribution parameter was not based in densities had the most similar to the results among themselves and the experimental measurements. This might be due to the air-water flow void fraction being more related to the difference between velocities, geometry and mass flows than to the volumes.

## 6.1 FURTHER WORKS

As the results show a mean error and standard deviation below the 20 %, the implementation of the impedance void fraction sensor in refrigeration systems might be useful as its results are not much different from the image analysis. However, it is important to keep in mind that the results of this work had a wide gap between the densities of the fluids, which affected the correlations which had a huge bond to these paramaters.

The implementation of the capacitance sensor shall be done in further works as well, since the impedance needle-probe void fraction sensor is an intrusive tool that might affect the flow, while the proposed capacitance sensor is non-intrusive.

This work also opens the possibility to manage cost-effective sensors not only for research purposes, but for industrial and control purposes as well, since most sensors built for research are usually expensive and not so easy to install and uninstall.



# RESUMEN AUTOBIOGRÁFICO

---

Oziel Silva Alvarado

Candidato para obtener el grado de  
Maestría en Ciencias de la Ingeniería  
con Orientación en Energías Térmica y Renovable

Universidad Autónoma de Nuevo León  
Facultad de Ingeniería Mecánica y Eléctrica

Tesis:

DEVELOPMENT OF A VOID FRACTION SENSING METHOD FOR  
TWO-PHASE FLOW CHARACTERIZATION AND ITS APPLICATION IN  
REFRIGERATION SYSTEMS

Nacido en Monterrey en el Estado de Nuevo León, México en 1999 e hijo de José Juventino Silva Jurado y Elizabeth Alvarado Martínez, me recibí en la licenciatura de Ingeniería Mecánica Eléctrica en la Facultad de Ingeniería Mecánica y Eléctrica de la Universidad Autónoma de Nuevo León a diciembre del 2020. Aprendí inglés, alemán y japonés en el Centro de Idiomas de la Facultad de Filosofía y Letras de la misma institución, certificándome en el examen de japonés, JLPT, con el nivel N3 en marzo del 2020. Laboré en proyectos de instalación de paneles solares en la compañía SERSOLAR S.A. de C.V. de 2018 a 2020.

# AUTOBIOGRAPHICAL SUMMARY

---

Born in Monterrey in the State of Nuevo León, Mexico in 1999. Son of José Juventino Silva Jurado and Elizabeth Alvarado Martínez. I graduated from college in the program of 'Electrical Mechanical Engineering' at the school 'Facultad de Ingeniería Mecánica y Eléctrica' from the college 'Universidad Autónoma de Nuevo León' in December 2020. I learned English, German and Japanese at the Language Center of the school 'Facultad de Filosofía y Letras' from the same mentioned college, certifying in the Japanese exam, JLPT, with level N3 in March 2020. I worked on solar panel installation projects at the company SERSOLAR S.A. de C.V. from 2018 to 2020.